STATISTICAL IMAGING OF TRANSPORT IN COMPLEX FLUIDS: A JOURNEY FROM ENTANGLED POLYMERS TO LIVING CELLS

BY

BO WANG

DISSERTATION

Submitted in partial fulfillment of requirements
for the degree of Doctor of Philosophy in Materials Science and Engineering
in the Graduate College of the
University of Illinois at Urbana-Champaign, 2011

Urbana, Illinois

Doctoral Committee:

Professor Steve Granick, Chair
Professor Kenneth S. Schweizer
Assistant Professor Jianjun Cheng
Assistant Professor William M. Brieher

ABSTRACT

Combining advanced fluorescence imaging, single particle tracking, and quantitative analysis in the framework of statistical mechanics, we studied several transport phenomena in complex fluids with nanometer and millisecond resolution. On the list are diffusion of nanoparticles and vesicles in crowded environments, reptational motion of polymers in entangled semidilute solutions, and active endosome transport along microtubules in living cells. We started from individual trajectories, and then converged statistically to aggregate properties of interests, with special emphasis on the fluctuations buried under the classic mean-field descriptions. The unified scientific theme behind these diversified subjects is to examine, with experiments designed as direct as possible, the commonly believed fundamental assumptions in those fields, such as Gaussian displacements in Fickian diffusion, harmonic confining potential of virtual tubes in polymer entanglements, and bidirectional motion of active intra-cellular transport. This series of efforts led us to discoveries of new phenomena, mechanisms, and concepts. This route, we termed as "statistical imaging", is expected to be widely useful at studying dynamic processes, especially in those emerging fields at the overlap of physics and biology.

ACKNOWLEDGEMENTS

First and foremost, I would like to thank my advisor, Professor Steve Granick, for his patience, guidance and support. During the past few years, what he has transmitted to me is not only knowledge and intuition, but also a panoramic view of science and desire to be helpful. Also greatly appreciated is Dr. Sung Chul Bae, for his unique personality and unparalleled expertise in optics.

I would like to thank Prof. Kenneth S. Schweizer, who laid the theoretical foundation of my education in my early days in Urbana, and later intensified it for me during our continuous collaborations. I want to thank Prof. Jianjun Cheng, who has generously provided me his insights in nanomedicine and his cell culture facility for me to work with living cells. I also want to thank other committee members, Prof. William Brieher and Prof. Taekjip Ha for lending me their expertise in biology and physics. The overlap of these fields is, in my opinion, the most exciting area of science today.

I would like to thank all the members of the Granick group, past and present, whom I have enjoyed working alongside. In particular, Dr. Liangfang Zhang set me oriented when I first arrived in Urbana and has advised me since then as an older brother. Dr. Minsu Kim and Dr. Stephen M. Anthony introduced me to single particle tracking. Juan Guan has accompanied me in numerous experiments as a close collaborator and friend. James Kuo, a talented undergraduate student working with me, and Kejia Chen both have indispensable contributions to the work presented in this dissertation.

Additionally, I want to thank Dr. Xuan Zhen, who has graduated from the Cahill group, Jian Yang from the Schweizer group, Li Tang from the Cheng group, Dr. Dutt Meenakshi from the Luijten group, Nathan Schmidt from the Wong group, and Cheng Song and Prof. Dongwan

Yoo at Vet-Med. This is just a small portion of the people that I have had the pleasure to collaborate with, although those studies are not included here. This environment of extensive collaboration at the Department of Materials Science at Illinois made here the most scientifically exciting place for graduate work.

This work was supported by the U.S. Department of Energy, Division of Materials Science, under Award No. DEFG02-02ER46019. For instrumentation, we acknowledge support from NSF-DMR-0907018.

TABLE OF CONTENTS

CHAPTER 1

INTRODUCTION

Everything worthwhile and intelligent has already been thought. One can only try to think it over again. – Johann Wolfgang von Goethe

1.1 Objective and Significance

Traditionally, scientific experiments mainly rely on measurements on average: we measure the temperature of gases, which is an average of kinetic energy of individual gaseous particles; we measure the bulk spectroscopic response, which is the average of molecular configurations; in biology we measure the expression through electrophoresis and blot, which again is an average with no information about cell-to-cell variability. On the contrary, imaging is an intrinsically powerful approach to study heterogeneity on the level of single trajectories. As a voyeur, we can now watch single molecules or particles go about their business, and record/quantify their behaviors with unprecedented details [1,2].

However, only a plain report of what is seen does not surpass the old routine dating back hundreds of years when science was only phenomenological, no matter how many quantitative details are added in if no new insight is gained. In our vision, to set discussion to a higher standard, imaging has to be combined with statistical mechanics in ways that I am going to explain below. With technological advancements over the past decade, we are now ready to go beyond the tradition measuring the macroscopic observables to deduce the underlying collections of individual behaviors through theoretical developments. We commence from the bottom by

experimentally measuring the dynamics of individual trajectories and then converging to aggregate properties of interest statistically. This is what we mean by "statistical imaging".

Specifically, in the first place, we aim to measure and understand the fluctuations around the ensemble averages. With the knowledge of low order moments, one can only guess what is hidden. Instead, with statistical imaging, we now are equipped to explore what is buried under the so-called "noise" by direct measurements. By accumulating voluminous data, we can cover many decades in time, space and probability, and then inquire if and to what extent the classic distribution functions, for example Gaussian displacements in Brownian motion [3], are correct. By quantifying the deviations of individuals from the mean-field description, we can ask what the cause and consequences of these fluctuations are [4]. The stochastic fluctuations become even more critical when the system shrink to such a small size that randomness finally dominates the average.

Second, we would like to capture the rare events. These are the events which are statistically rare and therefore are easily concealed in averages, but are often physically and functionally important. Typical examples of this type are the intermittency in glassy dynamics [5], the avalanches of occurrence of earthquakes [6], and the bursts in gene expression [7,8]. For this purpose, we need to patiently follow many individuals— individual molecules, individual particles, individual cells, and even individual time steps— one-by-one, until enough instances are collected to draw a conclusion with statistical significance.

Third, we hope to sample all possible paths and states in the systems. Experiments can often be biased by subjectively selecting what to look at and what not to according to hypothesis or presumptions, or favored unevenly due to inconspicuous weighting underlying ensemble average measurements. These limitations also exist for imaging, especially in the situations when only a few samples can be examined. Statistical imaging, instead, emphasizes on large statistics by imaging thousands or even millions of points with no pre-selection, and relies on transparent and simple hypothesis put in subsequent data processing. Moreover, with explicit weighting, we

therefore are able to reconstruct the path in trajectory space [9], which is inaccessible otherwise if the analysis is done over time, space, or even both. This is often crucial to reveal and discriminate the nature of the systems, particularly when non-equilibrium dynamics is concerned.

Fourth, due to the intrinsic heterogeneity and large variability as nature always bears, statistics is the most reliable, if not only, way of characterizing the systems quantitatively. To fully disentangle the complexity, these descriptions often have to be multi-parametric and thus naturally of high dimension [10], which imaging does support. In this context, the correlations or the principal components (or other statistical dimensionally reductive depictions such as network notations) [10-13] become the most important characteristics instead of mere mean values.

The scope of this dissertation is to develop and implement this methodology in transport problems in complex fluids.

1.2 Organization

In the following chapters, I am going to illustrate and enrich the general ideas aforementioned. While the subjects in each chapter are interesting on their own due to their significance in diffusion, polymer physics, and active transport, these studies are organized together to systematically provide a multifaceted view on the concept of "statistical imaging".

Chapter 2 serves as a prelude. It highlights the necessity to clarify the basic interactions in the systems of interest, as we always do as the initial step, in order to set the stage for the imaging studies. In the same spirit, the preparation and characterization of liposomes are also included as appendix A.

Chapter 2: The nonspecific adsorption of charged nanoparticles onto single component phospholipid bilayers bearing phosphocholine headgroups is shown, from fluorescence and calorimetry experiments, to cause surface reconstruction at the points where

nanoparticles adsorb. Nanoparticles of negative charge induce local gelation in otherwise fluid bilayers; nanoparticles of positive charge induce otherwise gelled membranes to fluidize locally. Through this mechanism, the phase state deviates from the nominal phase transition temperature by tens of degrees. This work generalizes the notions of environmentally induced surface reconstruction, prominent in metals and semiconductors. Bearing in mind that chemical composition in these single-component lipid bilayers is the same everywhere, this offers a mechanism to generate patchy functional properties in phospholipid membranes.

The next chapter deals with Brownian motion of point objects, and focuses on the situations where non-classic effects start to emerge. The fundamental question to be answered there is how transport via thermal agitation is modulated in crowded environments with prominent slow long-range background fluctuations.

Chapter 3: We describe experiments using single-particle tracking in which mean-square displacement is simply proportional to time (Fickian) yet the distribution of displacement probability is not Gaussian as should be expected of a classical random walk, but instead is decidedly exponential for large displacements, the decay length of the exponential being proportional to the square root of time. The first example is when colloidal beads diffuse along linear phospholipid bilayer tubes whose radius is the same as that of the beads. The second is when beads diffuse through entangled F-actin networks, bead radius being less than one-fifth of the actin network mesh size. We explore the relevance to dynamic heterogeneity in trajectory space, which has been extensively discussed regarding glassy systems. Data for the second system might suggest activated diffusion between pores in the entangled F-actin networks, in the same spirit as activated diffusion and exponential tails observed in glassy systems. But the first

system shows exceptionally rapid diffusion, nearly as rapid as for identical colloids in free suspension, yet still displaying an exponential probability distribution as in the second system. Thus while the exponential tail is reminiscent of glassy systems, in fact these dynamics are exceptionally rapid. We also compare to particle trajectories that are at first subdiffusive but Fickian at the longest measurement times, finding that displacement probability distributions fall onto the same master curve in both regimes. The need is emphasized for experiments, theory, and computer simulation to allow definitive interpretation of this simple and clean exponential probability distribution.

Then we stretched to polymer physics, where the intramolecular fluctuations must be taken into account additionally. Despite considerable theoretical work on the fundamentally important concept of "entanglement" in polymer physics for more than half a century, the direct experiments have been still challenging. In chapters 4 and 5, we are able to track molecules in polymer networks, which provides us an unique opportunity to revisit those excellent questions.

Chapter 4: Using single-molecule fluorescence imaging, we track Brownian motion perpendicular to the contour of tightly-entangled F-actin filaments and extract the confining potential. The chain localization presents a small-displacement Hookean regime followed by a large amplitude regime where the effective restoring force is independent of displacement. The implied heterogeneity characterized by a distribution of tube width is modeled.

Chapter 5: Single molecule fluorescence imaging shows explicitly the quasi-1D Rouse motion of both the center of mass and the curvilinear center diffusion of λDNA in F-actin networks and agarose gel with matched mesh size. Looking beyond the ensemble

averages which confirm classic mean-field theory, we highlight prominent and systematic heterogeneity in the single-molecule response.

The final two chapters represent the beginnings of a new path to analyze the dynamics in living cells in the context of physical biology. They serve as the first trials to explore the potential of such an approach in fields where dynamics is as rich but statistical mechanics is less developed. While we started from endosomal active transport, the ultimate goal is to understand the mechanism dealing with the complex spatiotemporal heterogeneity in cells (or even in organisms) while maintaining their tightly regulatory programming.

Chapter 6: A fundamental problem of living cells is transport of matter and signal. In multiple mammalian cell lines and endosome populations, we used a new wavelet-based method to analyze active mobility as endosomes ("cargo") move along microtubules imaged by single-particle fluorescence tracking. We demonstrate that motion exceeding micrometers is random so as to enhance search efficiency for the target. Roughly half the elapsed time is spent in a newly-identified search phase of active motion, half in a transport phase, but the directional persistence of both is decidedly shorter than the microtubule stiffness. This conclusion is conserved quantitatively across cell lines, implying that cellular cargo hops in regulated fashion between microtubules. Biphasic mobility offers new conceptual understanding of how endosomes find the right spots for their biological missions.

Chapter 7: We scrutinize the spatially-resolved speed of active cargo transport in living cells over times and distances that slow environmental relaxation dominates, and show pervasive bursts of salutatory acceleration resembling nonlinear dynamics driven by

weak force in glass forming systems. These nonlinear fluctuations follow a scaling law over several decades of time and space, the statistical regularities displaying a time-averaged shape that we interpret to reflect stress buildup followed by rapid release. The power law of scaling is the same as seen in driven jammed colloids, granular, and magnetic systems. The implied regulation of active transport with environmental obstruction in the cytoplasm places the problem in the context of nonequilibrium mechanics, thus extending the classical notion of "molecular crowding". Augmenting previous work that explained active motion from step taken on the molecular level, this study of transport shows a different rate-limiting step.

1.3 Future Prospects

While the majority of the work presented here concerns fluorescence imaging and single particle tracking with nanometer and millisecond resolution, we are certainly not constrained by these means. In terms of technique, as we switched from epi-fluorescence to highly inclined illumination optical [14] microscopy in the latter half of this series of experiments, the imaging strategy should be guided by experimental demands. Two potentially useful techniques on our list are super-resolution microscopy [15] if the concentration of the species of interest is too high, and widefield 2-photon sectioning microscopy by multifocal temporal focusing [16] when we are interested in larger view and deeper penetration into the sample. One mustn't blindly insist on quantification with high resolution either, since the most useful information is on the relevant time and length scales of the system, and sometimes reality does not allow perfectionism.

While logical extensions of the systems covered in the subsequent chapters includes imaging single polymers in entangled networks under shear forces, and following artificial nanomaterials with well defined geometry and chemical compositions when they navigate through different endocytic pathways, we shouldn't constrain ourselves to this particular set of

problems. We believe that the methodology described here could contribute in prominent ways to other fields such as biology, especially developmental biology where dramatic transformations occur with incredible spatiotemporal accuracy.

1.4 References

1. Moerner WE, Orrit M (1999) Illuminating single molecules in condensed matter. *Science* 283: 1670-1676.
2. Granick S, *et al.* (2010) Single-molecule methods in polymer science. *J. Polym. Sci. Pt. B-Polym. Phys.* 48: 2542-2543.
3. Wang B, Anthony SM, Bae SC, Granick S (2009) Anomalous yet Brownian. *Proc. Nat. Acad. Sci. USA* 106: 15160-15164.
4. Szymanski J, Weiss M (2009) Elucidating the origin of anomalous diffusion in crowded fluids. *Phys. Rev. Lett.* 103: 038102.
5. Weeks ER, Crocker JC, Levitt AC, Schofield A, Weitz DA (2000) Three-dimensional direct imaging of structural relaxation near the colloidal glass transition. *Science* 287: 627-631.
6. Sethna JP, Dahmen KA, Myers CR (2001) Crackling noise. *Nature* 410: 242-250.
7. Pedraza JM, Paulsson J (2008) Effects of molecular memory and bursting on fluctuations in gene expression. *Science* 319: 339-343.
8. Suter DM, *et al.* (2011) Mammalian genes are transcribed with widely different bursting kinetics. *Science* 332: 472-474.
9. Wu D, *et al.* (2009) Trajectory approach to two-state kinetics of single particles on sculpted energy landscapes. *Phys. Rev. Lett.* 103: 050603.
10. Collinet C, *et al.* (2010) Systems survey of endocytosis by mutiparametric image analysis. *Nature* 464: 243-249.

11. Cohen AE, Moerner WE (2007) Principle-components analysis of shape fluctuations of single DNA molecules. *Proc. Nat. Acad. Sci. USA* 104: 12622-12677.
12. Slack MD, Martinez ED, Wu LF, Altschuler SJ (2008) Characterizing heterogeneous cellular responses to perturbations. *Proc. Nat. Acad. Sci. USA* 108: 19306-19311.
13. Parsa H, Upadhyay R, Sia SK (2011) Uncovering the behaviors of individual cells within a multicellular microvascular community. *Proc. Nat. Acad. Sci. USA* 108: 5133-5138.
14. Tokunaga M, Imamoto N, Sakata-Sogawa K (2008) Highly inclined thin illumination enables clear single-molecule imaging in cells. *Nat. Methods* 5: 159-161.
15. Jones SA, Shim S-H, He J, Zhuang XW (2011) Fast, three-dimensional super-resolution imaging of live cells. *Nat. Methods* 8: 499-505.
16. Vaziri A, Shank CV (2010) Ultrafast widefield optical sectioning microscopy by multifocal temporal focusing. *Opt. Express* 18: 19645-19655.

CHAPTER 2

NANOPARTICLE-INDUCED SURFACE RECONSTRUCTION OF PHOSPHOLIPID MEMBRANES

Adapted with permission from Bo Wang, Liangfang Zhang, Sung Chul Bae, and Steve Granick (2008) Nanoparticle-induced surface reconstruction of phospholipid membranes, Proceedings of the National Academy of Sciences of the United States of America, 105, 18171-18175.

2.1 Background

That phospholipid membranes possess patchy functional properties (different from spot to spot) is fundamental to their use as biomaterials and biosensors [1,2], as well as a multitude of cellular activity [3-6]. The extensive and sometimes contentious literature on the origins of spatial modulation supposes patchiness to arise from inhomogeneous distribution of the different lipids and other components within typical membranes and in some cases to specific binding [7-10]. Here phospholipid vesicles that do not satisfy the traditional requirements are stimulated to display spatial patchiness in response to non-specific binding by charged nanoparticles. By using fluorescence and calorimetry methods to study membranes formed from single-component lipids with phosphocholine headgroups, anionic nanoparticles are shown to induce local gelation in otherwise-fluid bilayers and cationic nanoparticles to induce local fluidization of otherwise-gelled bilayers. This work generalizes the notions of environmentally-induced surface reconstruction, prominent in metals and semiconductors [11-13]. Unlike adsorption-induced surface restructuring of solids, the present systems are more strongly influenced by the high mobility of the lipid molecules that comprise phospholipid membranes. It also suggests origins of potential biological

activity of nanoparticles that increasingly are exposed through the environment to living systems by accident and design [14,15].

2.2 Results and Discussions

The hypothesis that motivates this study is summarized in Fig. 2.1: a phospholipid bilayer's local phase state can be switched by binding of charged nanoparticles such that they alter the tilt angle of the phosphocholine (PC) headgroup, which is terminated by an electric dipole of phosphate and choline, $P^{-}N^{+}$. Negatively-charged (anionic) nanoparticles interact preferentially with the N^{+} terminus, raising the angle of the dipole above the average angle of 0~3° characteristic of the fluid phase [16] and recruiting lipid tails to densify; conversely, positively-charged (cationic) nanoparticles reduce the tilt angle below the angle of 30~65° characteristic of the gel phase [16], stimulating a reduced lipid density. To exclude the traditional explanations of spatial patchiness based on specific binding, redistribution of membrane components, and phase separation between different lipids [7-10], these possibilities were eliminated by constructing phospholipid membranes comprised of a sole lipid type. The possibility of specific binding was eliminated by selecting lipids bearing phosphocholine headgroups, which are uncharged under the buffer conditions of these experiments [17].

The phospholipids employed here, DOPC (dioleoyl PC), DLPC (dilauryl PC), and DPPC (dipalmitoyl PC), have gel-to-fluid phase transition temperatures (T_m) of ~ -20, ~ -1, and ~ +40 °C, respectively. Large unilamellar lipid vesicles (liposomes) were prepared at 1 vol% concentration in PBS buffer (10 mM, pH=6.0) by the well-known extrusion method. The main nanoparticles used were carboxyl-modified (negatively charged; ~0.91 e^{-}/nm^2) and amidine-modified (positively charged; ~0.25 e^{+}/nm^2) white polystyrene (PS) latex with a diameter of 20 nm; in control experiments, silicon dioxide nanoparticles (~0.11 e^{-}/nm^2) and supercoiled plasmids were also used. Charged nanoparticles were mixed by vortex into the liposome suspension at the

desired molar ratio [18]. Measurements were performed at room temperature. It is known that charged nanoparticles, both anionic and cationic, adsorb to the PC group of phospholipids and that liposomes carrying adsorbed nanoparticles maintain their integrity as discrete liposomes [18,19].

A simple initial test of our hypothesis was that adsorption by anionic nanoparticles should cause liposomes to shrink beacause the area per lipid headgroup is less in the gel than in the fluid phase. The anticipated shrinkage of initially-fluid liposomes when anionic nanoparticles adsorb was confirmed by fluorescence correlation spectroscopy (FCS), showing shrinkage of hydrodynamic radii by ≈20%. A delicate point then became to decide whether phase-separated regions would clump together; the tendency to minimize line tension favors this but electrostatic repulsion between charged nanoparticles resists it. Electron microscopy was not successful in imaging the spatial distribution of nanoparticles, their binding to liposomes being too weak to survive quench to the needed cryogenic temperatures. However, fluorescence imaging at room temperature revealed a highly dynamic spatial distribution and no aggregation of the nanoparticles on optical length scales when they adsorbed to giant unilamellar vesicles (GUVs). Förster resonance energy transfer (FRET) experiments described below set an even smaller upper bound on the size of phase-separated regions, 10-100 nm.

Moving to information on a molecular level, Fig. 2.2a illustrates the raw fluorescence data when anionic nanoparticles were allowed to bind to DLPC liposomes containing embedded Laurdan, which is an uncharged fluorescent dye whose emission is known to be diagnostic of a phospholipid membrane's phase state [20]. Normally, Laurdan assay is used to diagnose a membrane's phase when temperature is varied; this work is considered its first application to diagnose surface reconstruction. Fluorescence emission is plotted against wavelength and one observes the progressive rise of blue emission and loss of red emission as nanoparticle concentration increased – suggestive of fluid-gel phase coexistence such that the proportion of fluid to gel phase varies. For quantification, emission intensity was compared at the wavelengths

of peak emission intensity for bilayers in pure fluid and gel phases. Fig. 2.2b plots against normalized nanoparticle concentration the intensity fraction of these two peaks, and one sees that the changes are linear over a considerable span of nanoparticle concentration. Their normalized difference is the traditional definition of the net polarization, $P \equiv (I_B - I_R)/(I_B + I_R)$, where I_B and I_R are the emitted intensity at these wavelengths in the blue and red respectively [20]. From the data in Fig. 2.2b, P was calculated and found to vary smoothly between values characteristic of the membrane fluid phase (no added nanoparticles) and the gel phase (maximum concentration of added nanoparticles). The proportionality to nanoparticle concentration signifies that nanoparticles bound in proportion to their concentration in the environment and that lipid gelled in local spots where nanoparticles bound. Fig. 2.2c plots the implied lipid gel fraction against surface coverage.

The findings did not depend on choice of the lipid: the data are the same when the same anionic nanoparticles were allowed to bind to DOPC liposomes, whose T_m is ~ -20ºC. The findings did not depend on liposome size either, being indistinguishable for liposomes 200 and 80 nm in mean diameter. Silica particles had a similar but weaker effect (not shown) but presented the advantage of offering a range of particles of different size but similar chemical makeup. These experiments demonstrated that the nanoparticle size plays a minor role. The density of surface charge on the nanoparticles, nearly an order of magnitude larger for carboxyl-modified polystyrene latex than for silica, correlates with the stronger enhancement of the phase transition that was observed for carboxyl-modified latex. All these nanoparticle systems share the feature that charge on these objects was held rigidly in place. Adsorbed DNA, which also is anionic, did not produce this effect. We believe the reason to be that whereas DNA is flexible, the rigidity of charge placement on nanoparticles enables them to template the phase state of the phospholipids to which they bind. This null result for the case of flexible charged objects incidentally demonstrates that the photophysical response of the fluorescent dye was unmodified by charge, thus validating the data in Fig. 2.2.

The hypothesis predicts the opposite effect for cationic nanoparticles. This was validated by allowing cationic nanoparticles to bind to a DPPC membrane ($T_m \approx 40$ºC), which at the experimental temperature (~ 20ºC) displayed $P \approx 0.6$ before nanoparticles were added. As shown in Fig. 2.2d, the net polarization then decreased and detailed inspection of the emission raw data shows that the shift of emission wavelength was less pronounced than after adding carboxyl-modified nanoparticles to DLPC membrane as shown in Fig. 2.2b, consistent with the expected weaker binding of cationic particles [19]. The decrease of P again suggests that the phase transition was localized to regions where nanoparticles had bound. In Fig. 2.2d, the final fraction of liquid phase can be estimated as 20% – though the experimental temperature was less than the literature value of this lipid's T_m. The addition of cationic nanoparticles to DLPC ($T_m \approx -1$ºC) liposomes induced negligible change of net polarization, consistent with the anticipation that positively particles do not fluidize initially-fluid lipids.

FRET experiments afforded an independent test of the hypothesis of nanoparticle-induced gelation, as the efficiency of energy transfer between two fluorescent dyes must decrease when they become spatially separated by partitioning into different phases. For this purpose, NBD and Rhodamine B (RhB) were selected because phospholipids bearing an NBD probe are known to partition into the gel phase of lipid membranes but phospholipids bearing a RhB probe do not [21]. Fig. 2.3 plots the logarithmic normalized emission against time on the nanosecond time scale under the conditions specified in the figure caption. The lifetime of NBD increased as anticipated after adding nanoparticles, consistent with its partitioning into the gel phase. In addition, the FRET efficiency in lifetime experiments decreased, indicating increased distances between the two dyes, as should be expected since the donor and acceptor dyes partitioned into different lipid phases. The magnitude of decrease is in the range expected from prior studies on microscopic phase separation involving two chemically-different lipid components [21], corroborating the idea of local phase transition. The absolute value of the observed FRET

efficiency shows that the domain size is in the range of 10-100 nm, according to theoretical estimates [22].

A final independent test of the hypothesis of nanoparticle-induced surface reconstruction consisted in using isothermal titration calorimetry (ITC) to measure the enthalpy (ΔH) of binding [23]. Fig. 2.4a shows raw data when anionic nanoparticles were added to DLPC liposomes and Fig. 2.4c shows the integrated heat change plotted against normalized nanoparticle concentration. Consistent with the hypothesis of nanoparticle-induced gelation, the initially-exothermic binding was followed, at the highest NP concentrations, by an endothermic process, which is expected since binding-induced shrinkage of the liposome should be endothermic. Fitting gives the binding constant of $\sim 10^8$ M^{-1}, corresponding to a modest free energy of binding, ~20 k_BT per particle. The dramatic difference between enthalpy and free energy reveals a significant contribution from entropy, presumably partly from loss of entropy by gelation, partly from release of hydrated water from the PC headgroups when nanoparticles bind. The deviation of the fitting in the range of high molar ratio may reflect cooperative gelation, which also reconciles the absence of plateau in heat change with linearity of the phase transition measured by fluorescence polarization. But in contrast to this, allowing positively-charged nanoparticles to bind to gel-phase DPPC liposomes showed that this process was uniformly endothermic, as anticipated if nanoparticles caused the lipids to fluidify. The raw data (Fig. 2.4b) was integrated to give the integrated heat change plotted against normalized nanoparticle concentration in Fig. 2.4d. Thus, the sign of calorimetric heat changes is consistent with the conclusions that emerged from the independent fluorescence measurements. We speculate that cooperativity of this fluidization may be less than of the gelation transition, which may be facilitated by long-range correlations of lipid chain alignment, but no quantitative explanation is presented at this time.

2.3 Conclusions

The traditional notion of how to produce spatially patchy stiffness of a phospholipid membrane is by phase separation of lipids with different intrinsic stiffness [10]; but when phospholipid membranes reconstruct locally in response to binding as described here, it is reasonable to infer that they will be locally stiffer in the gelled patches and less stiff in the fluidized patches, so nanoparticle-induced reconstruction of the phase state offers a new mechanism to modulate stiffness. Similarly, the traditional notion of how to produce a thermodynamic line tension in a phospholipid membrane is from the phase coexistence of different components [24]; this study, showing that even the same lipid can coexist in two different phases according to what binds to it, presents an additional mechanism. Binding-induced structural reorganization also provides a potential mechanism to couple membrane fluctuation and transportation/clustering of absorbates [25]. Surfactants are known to reorganize upon transfer to planar solids and removal from water [26] and it is intriguing to notice some analogy to the present very different case of *in situ* adsorption of nano-sized particles. Also pleasing is to generalize the notion of environmentally-induced surface reconstruction, which is prominent for metals and semiconductors [11-13] but not identified previously for phospholipid systems. However, it is worth emphasizing that as model phospholipid systems were studied here in order to simplify the problem, the question of generalizing the conclusions of this study to living organisms remains unresolved.

2.4 Materials and Methods

Materials

The phospholipids DLPC, DOPC, and DPPC were obtained from Avanti Polar Lipids, Inc.. Large unilamellar lipid vesicles were prepared at 1 vol% concentration in PBS buffer (10 mM, pH=6.0) by the well-known extrusion method, employing procedures described in detail

elsewhere [18]. Carboxyl-modified (negatively charged) and amidine-modified (positively charged) white polystyrene (PS) latex with a diameter of 20 nm were purchased from Interfacial Dynamics Corp. (Eugene, OR). In control experiments, silicon dioxide nanoparticles with diameters of 4, 10 or 20 nm were obtained from Alfa Aesar. Plasmids (4 kbp) with a radius gyration of ~10 nm were extracted from Escherichia coli using standard protocols. Charged nanoparticles were mixed by vortex into the liposome suspension at the desired molar ratio [18]. From data given by the manufacturers, the surface charge density was calculated to be 1 charge per ~1.1 nm^2 for carboxyl-modified polystyrene nanoparticles, ~9 nm^2 for silica particles, and ~ 4.0 nm^2 for amidine-modified nanoparticles.

The fluorescent dye Laurdan, 6-dodecanoyl-2-dimethylaminonaphthalene, was purchased from Molecular Probes (Eugene, OR). The FRET (Förster resonance energy transfer) pair, N-(7-nitrobenz-2-oxa-1,3-diazol-4-yl)-dipalmitoylphosphatidylethanolamine) (NBD-DPPE) and N-(lissamine-rhodamine B)-dioleoylphosphatidylethanolamine (RhB-DOPE), were purchased from the same company.

Fluorescence correlation spectroscopy (FCS)

FCS measurements were carried out in the two photon excitation mode using a home-built apparatus. Briefly, a near-infrared femtosecond pulse laser was focused onto the sample through an objective lens. The excitation spot had a diffraction-limited diameter about 0.35 μm. Fluorescence was collected and detected by a single photon counting module. The translational diffusion coefficients (D) were obtained by fitting the fluorescence intensity-intensity autocorrelation function. The mean diameters of the liposomes, present at dilute concentration, were related to D using the Stokes-Einstein equation.

Dye orientation within liposomes

The final concentrations of Laurdan and phospholipid were 0.8 μM and 0.4 mM, respectively (probe : phospholipid = 1 : 500). Steady-state emission spectra of Laurdan were measured by using a fluorometer (Photon Tech., Brunswick, NJ) at magic angle condition with excitation at 340 nm. Emission spectra were corrected for instrument response. The characteristic wavelengths for gel and fluid phases respectively for various lipids were determined from the samples below or above the phase transition temperatures and agree with the values reported in the literature [27,28].

Time resolved FRET experiments

The approach of measuring fluorescence lifetime was used to make time-resolved FRET measurements. The donor was NBD-DPPE (probe : phospholipid = 1 : 1000), the acceptor was RhB-DOPE (probe : phospholipid = 1 : 200), in liposomes with 200 nm mean diameter. Excitation, achieved by a frequency-doubled Ti:sapphire laser, was performed at 460 nm to minimize RhB excitation and emission was measured in the region 500 – 530 nm, which selectively characterize NBD emission. The time-resolved lifetimes were measured using a data acquisition board purchased from Becker & Hickl GmbH. As the fluorescence lifetimes did not follow single exponential kinetics, the mean lifetime was defined, in the conventional way [21], as $\overline{\tau} = \sum_i \alpha_i \tau_i$. In most cases, the data were fitted with second order exponential decays summarized in Table 2.1.

ITC experiments

Isothermal titration calorimetry was performed using the VP-ITC high-sensitivity titration calorimeter (MicroCal, Northampton, MA) housed in the Post Genomics Institute at the University of Illinois. Typically, 58 consecutive aliquots of 5 μL each (for anionic PS particles),

or 29 consecutive aliquots of 10μL each (for cationic PS particles), containing nanoparticles at a concentration of 3 μM, were injected into the cell (1.43 mL) filled with 0.4 mM lipid solution (1 nM liposome). Both liposome and nanoparticle solutions were degassed under vacuum for 30 min immediately before use. Injections were made at 5 min intervals and at 0.5 μL-s^{-1} rate. A constant stirring speed of 300 rpm was maintained during the experiments to ensure sufficient mixing after each injection. For calculation of the binding isotherm, the heat of dilution was measured in separate nanoparticle-buffer titrations and was subtracted. Surface coverage was estimated from the raw data as follows. First, the projected nanoparticle area showed complete surface coverage in hexagonal close packing to occur at $C_{NP}/C_L = 400$; this estimate presents an upper bound of surface coverage. Second, $C_{NP}/C_L = 300$ is the point up to which changes of net polarization (P) were linear; therefore, the linear region in Fig. 2.2c ends at a fractional surface coverage of at least 0.75. Third, the calorimetry experiments showed that heat changes were completed approximately $C_{NP}/C_L = 500$. Assuming the binding affinity is still constant in the range of molar ratio between 300 – 500, but weaker because of electrostatic repulsion, we were able to extrapolate the surface coverage, and found out the relation of P to surface coverage remained linear in the whole range. We should mention that the surface coverage is estimated on the strong assumption that no cooperativity of phase transition exists, which cannot strictly be true but provides meaningful physical insight into the situation and quickly affords comparison between different systems, which would be difficult to achieve otherwise.

2.5 References

1. Groves JT, Boxer SG (2002) Micropattern formation in supported lipid membranes. *Acc. Chem. Res.* 35: 149-157.
2. Daniel S, Albertorio F, Cremer PS (2006) Making lipid membranes rough, tough and ready to hit the road. *MRS Bulletin* 31: 536-540.

3. Römer W, *et al.* (2007) Shiga toxin induces tubular membrane invaginations for its uptake into cells. *Nature* 450: 670-675.
4. Fielding CJ ed. (2006) *Lipid rafts and caveolae* (Wiley-VCH, Weinheim).
5. Anderson RG, Jacobson KA (2002) A role for lipid shells in targeting proteins to caveolae, rafts, and other lipid domains. *Science* 296: 1821–1825.
6. Simons K, Ikonen E (1997) Functional rafts in cell membranes. *Nature* 387: 569-572.
7. Collins MD, Keller SL (2008) Tuning lipid mixtures to induce or suppress domain formation across leaflets of unsupported asymmetric bilayers. *Proc. Natl. Acad. Sci. U.S.A.* 105: 124-128.
8. Forstner MB, Yee CK, Parikh AN, Groves JT (2006) Lipid lateral mobility and membrane phase structure modulation by protein binding. *J. Am. Chem. Soc.* 128: 15221-15227.
9. Binder WH, Barragan V, Menger FM (2003) Domains and rafts in lipid membranes. *Angew. Chem. Int. Ed.* 42: 5802-5827.
10. Baumgart T, Hess ST, Webb WW (2003) Imaging coexisting fluid domains in biomembrane models coupling curvature and line tension. *Nature* 425: 821-824.
11. Billinge SJL (2007) The problem of determining atomic structure at the nanoscale. *Science* 316: 561-565.
12. Somorjai GA, Contreras AM, Montano M, Rioux RM (2006) Clusters, surfaces, and catalysis. *Proc. Nat. Acad. Sci. USA* 103: 10577-10583.
13. Zhang H, Gilbert B, Huang F, Banfield JF (2003) Water-driven transformation in nanoparticles at room temperature. *Nature* 424, 1025-1029.
14. Dobrovolskaia MA, Mcneil SE (2007) Immunological properties of engineered nanomaterials. *Nat. Nanotechnol.* 2: 469-478.
15. Nel A, Xia T, Mädler L, Li N (2006) Toxic potential of materials at the nanolevel. *Science* 311: 622-627.

16. Somerharju P, Virtanen JA, Cheng KH (1999) Lateral organisation of membrane lipids-The superlattice view. *Biochim. Biophys. Acta Mol. Cell Biol. Lipids* 1440: 32-48.
17. Cevc G, Marsh D (1987) *Phospholipid bilayers: Physical Principles and Models* (John Wiley & Sons, New York).
18. Zhang LF, Granick S (2006) How to stabilize phospholipid liposomes (using nanoparticles). *Nano Lett.* 6: 694-698.
19. Yu Y, Anthony SM, Zhang LF, Bae SC, Granick S (2007) Cationic nanoparticles stabilize zwitterionic liposomes better than anionic ones. *J. Phys. Chem. C* 111: 8233-8236.
20. Gaus K, *et al.* (2003) Visualizing lipid structure and raft domains in living cells with two-photon microscopy. *Proc. Natl. Acad. Sci. U.S.A.* 100: 15554-15559.
21. de Almeida RDF, Loura LMS, Fedorov A, Prieto M (2005) Lipid rafts have different sizes depending on membrane composition: a time-resolved fluorescence resonance energy transfer study. *J. Mol. Bol.* 346: 1109-1120.
22. Towles KB, Dan N (2007) Determination of membrane domain size by fluorescence resonance energy transfer: Effects of domain polydispersity and packing. *Langmuir* 23: 4737-4739.
23. Cedervall T, *et al.* (2007) Understanding the nanoparticle-protein corona using methods to quantify exchange rates and affinities of proteins for nanoparticles. *Proc. Natl. Acad. Sci. USA* 104: 2050-2055.
24. Kuzmin PI, Akimov SA, Chizmadzhev YA, Zimmerberg J, Cohen FS (2005) Line tension and interaction energies of membrane rafts calculated from lipid splay and tilt. *Biophys. J.* 82: 1120-1133.
25. Reynwar BJ *et al.* (2007) Aggregation and vesiculation of membrane proteins by curvature-mediated interactions. *Nature* 447: 461-464.

26. Yaminsky V, Nylander T, Ninham B (1997) Thermodynamics of Transfer of Amphiphiles between the Liquid-Air Interface and a Solid Surface-Wetting Tension Study of Langmuir-Blodgett Films. *Langmuir* 13: 1746-1757.

27. Parasassi T, De Stasio G, Ravagnan G, Rusch RM, Gratton E (1991) Quantitation of Lipid Phases in Phospholipid-Vesicles by the Generalized Polarization of Laurdan Fluorescence. Bi*ophys. J.* 60: 179-189.

28. De Vequi-Suplicy CC, Benatti CR, Lamy MT (2006) Laurdan in fluid bilayers: Position and structural sensitivity. *J. Fluoresc.* 16: 431-439.

2.6 Figures

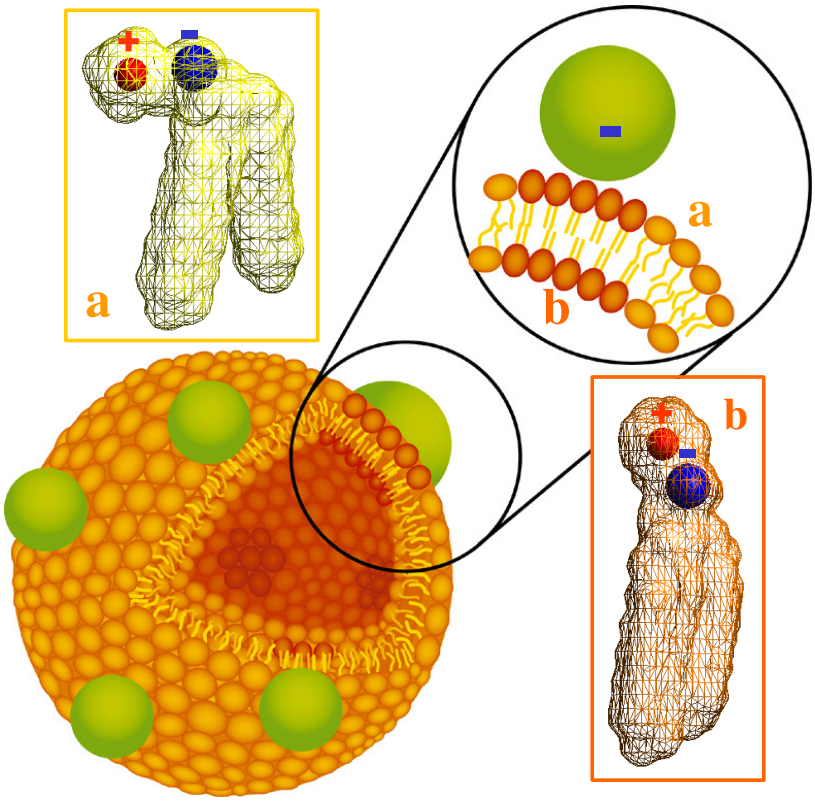

Figure 2.1

Schematic diagram of a phospholipid bilayer vesicle with bound nanoparticles. Binding of anionic nanoparticles to a lipid bilayer in the fluid phase causes the nanoparticle to template a gel phase in the place where the nanoparticle binds. Binding-induced reorientation of the phosphocholine (PC) headgroup causes lipids in the fluid phase to have lower density (a) than in the gel phase (b). In the PC headgroup, P^- and N^+ are denoted by blue and red, respectively.

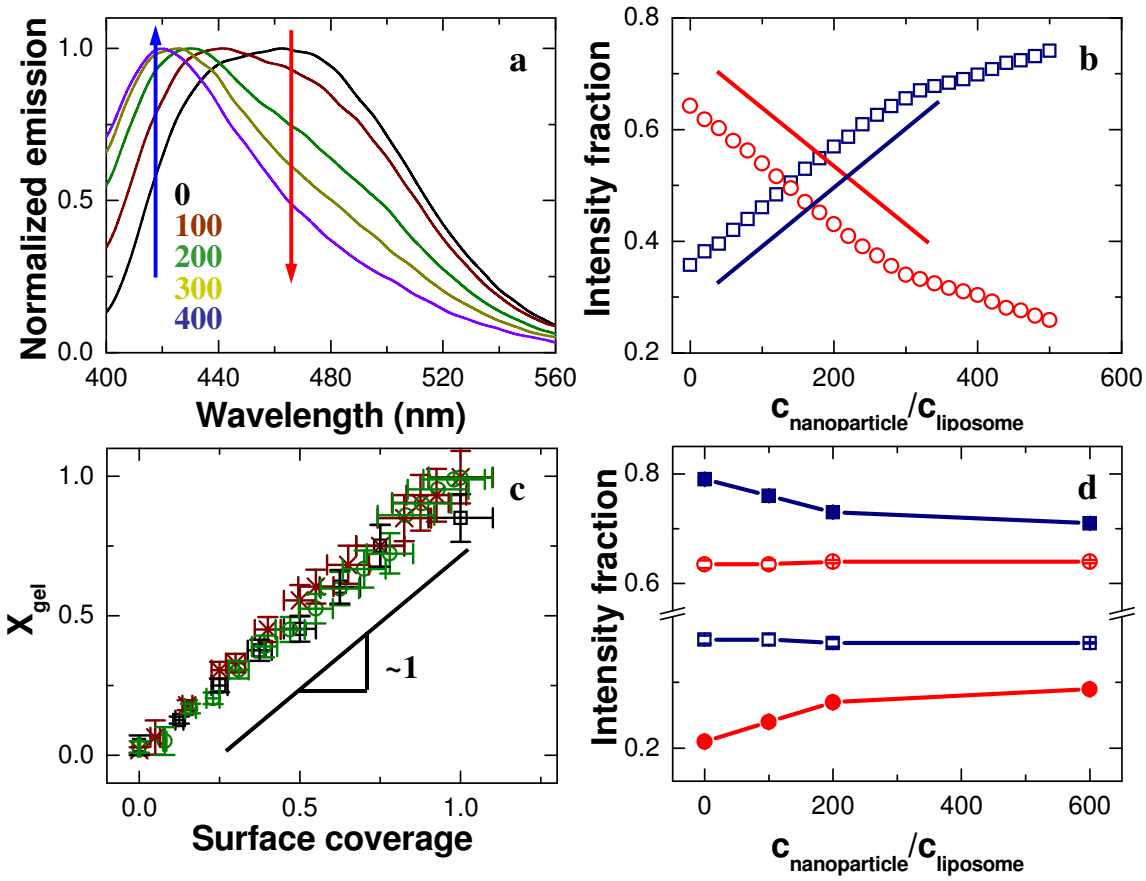

Figure 2.2

Experiments in which the fluorescence spectrum of Laurdan, an uncharged fluorescent dye that segregates into the hydrophobic region of lipid bilayers, is used to indicate the membrane phase state. (a) Normalized emission plotted against wavelength after anionic (carboxyl-modified) nanoparticles bind to 200 nm DLPC liposomes. The plot compares the cases of number ratio of particles to liposomes C_{NP}/C_L = 0, 100, 200, 300, and 400. (b) From data of the kind illustrated in Fig. 2A, the intensity fraction of blue and red emission at 416 (blue) and 473 nm (red) is plotted against C_{NP}/C_L. (c) Mole fraction of gel phase plotted against surface coverage for binding of anionic nanoparticles onto 200 nm fluid DLPC liposomes (red), 200 nm fluid DOPC liposomes (black), and 80 nm fluid DLPC liposomes (green); the data coincide within experimental uncertainty. Line with slope of unity is drawn for comparison. (d) The intensity fraction of blue emission (416 and 440 nm for DLPC and DPPC respectively) and red emission (473 and 490 nm for DLPC and DPPC respectively), plotted against C_{NP}/C_L for binding of cationic (amidine-modified) nanoparticles onto liposomes of DLPC (open symbols) and DPPC (filled symbols).

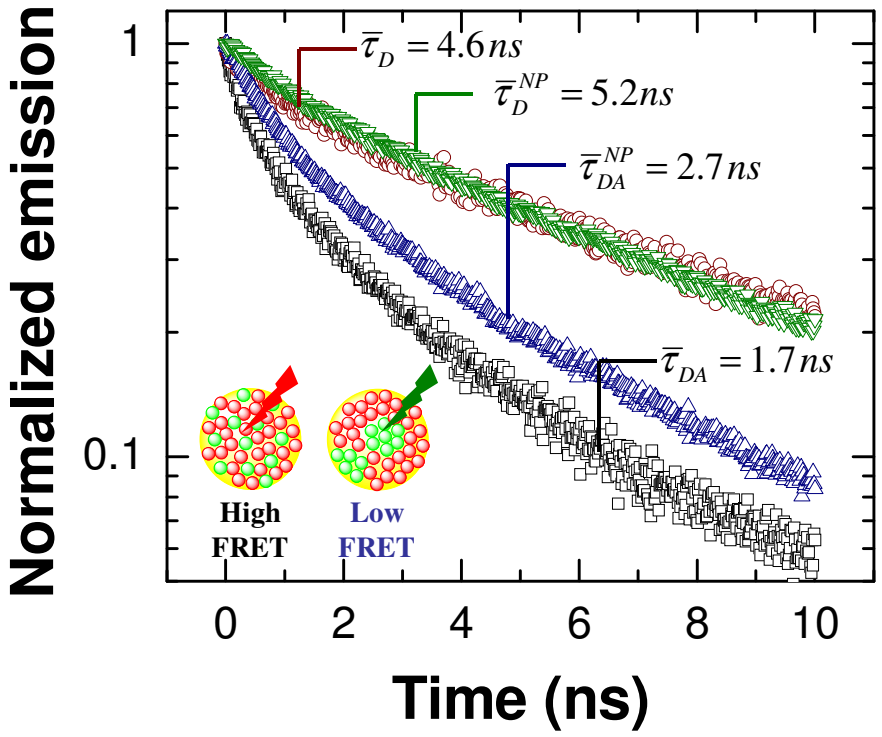

Figure 2.3

Fluorescence emission plotted against time on the nanosecond time scale for FRET (Förster resonance energy transfer) experiments involving 200 nm DOPC liposomes after adding anionic (carboxyl-modified) nanoparticles at number ratio of particles to liposomes C_{NP}/C_L = 200. The fluorescence donor was NBD-DPPE (0.1% concentration) and the acceptor was RhB-DOPE (0.5% concentration). The mean lifetime of the donor increases, after nanoparticle binding, from 4.6 to 5.2 ns and the FRET efficiency, evaluated from lifetime, decreases from 0.65±0.06 to 0.45±0.05. Alternatively, the SI shows fits of the fluorescence lifetimes to a sum of several decay processes. Wherever present in this figure, the superscript (NP) denotes the presence of bound nanoparticles, and the subscripts (D and A) refer to the presence of donor and acceptor fluorescent dyes, respectively. In the Inset, a schematic diagram compares randomly mixed FRET pairs, which is the situation of higher FRET efficiency, with the situation where the donor dye partitions into gel-phase regions as occurs in these experiments.

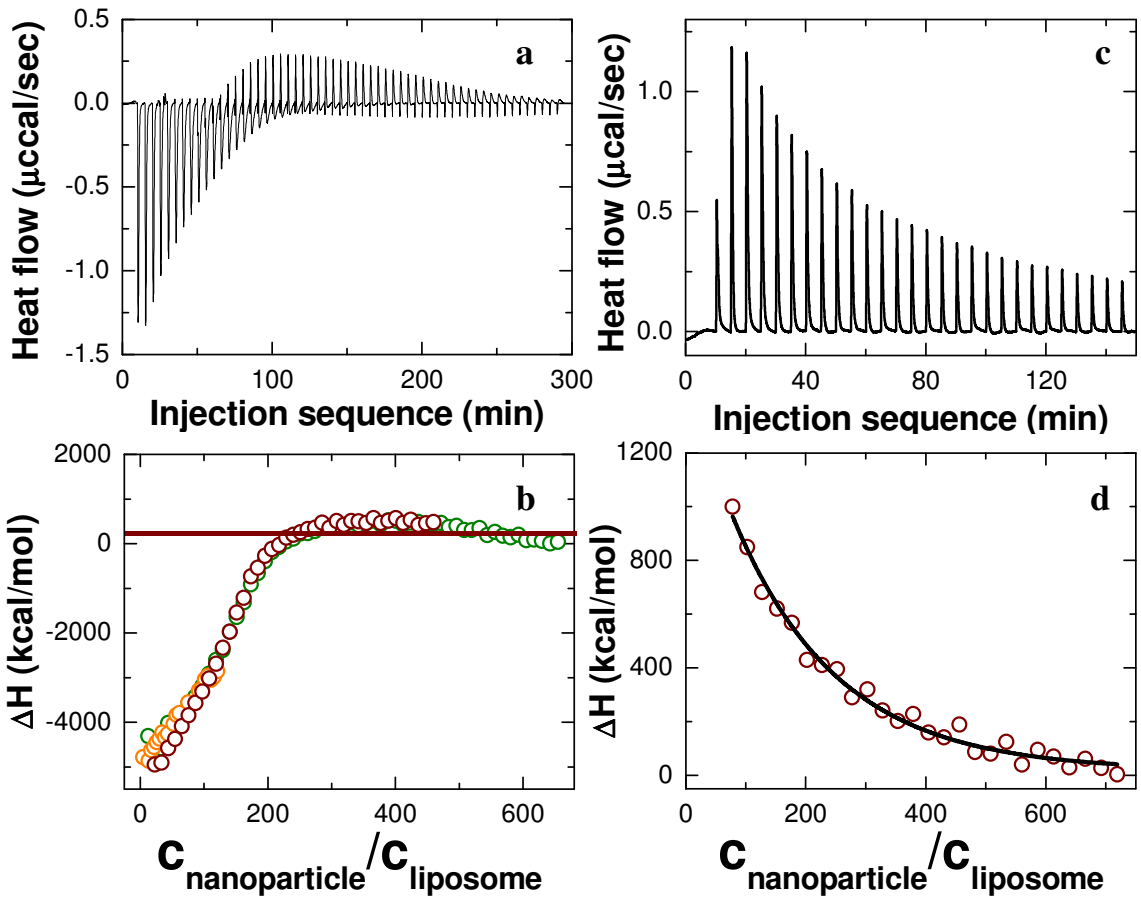

Figure 2.4

Isothermal titration calorimetry of liposomes with nanoparticles added. (a) Raw data, heat flow plotted against injection sequence, when a fluid-phase 200 nm DLPC liposome suspension is exposed to increasing amounts of anionic nanoparticles as described in the text. (b) Raw data when a gel-phase 200 nm DPPC liposome suspension is exposed to increasing amounts of cationic nanoparticles as described in the text. (c) Integrated enthalpy change after subtraction of heat of dilution plotted against number ratio of particles to liposomes, C_{NP}/C_L, for the case illustrated in (a). Data obtained from different concentrations of injected particle suspension are shown in a color-coded manner: blue: 3 μM; red: 2 μM; green: 1 μM. The liposome concentration was fixed at 1 nM. (d) Integrated enthalpy change after subtraction of heat of dilution plotted against number ratio of particles to liposomes, C_{NP}/C_L, for the case illustrated in Panel B. The heat of dilution was measured in separate control experiments and was subtracted for calculation of these binding isotherms.

2.7 Table

Table 2.1

Rather than the mean lifetime quoted in the caption of Fig. 2.3, this table tabulates a decomposition of the lifetime decay into the sum of two separate exponential decays with amplitudes α_1 and α_2 and exponential time constants τ_1 and τ_2, respectively. Wherever present, the superscript (NP) denotes the presence of adsorbed nanoparticles and the subscripts (D and A) refer to the presence of donor and acceptor fluorescent dyes, respectively.

	α_1	τ_1 *(ns)*	α_2	τ_2 *(ns)*
τ_D	0.17 ± 0.02	0.70 ± 0.08	0.74 ± 0.01	5.94 ± 0.31
τ_D^{NP}	0.19 ± 0.01	1.03 ± 0.07	0.80 ± 0.01	6.35 ± 0.25
τ_{DA}	0.37 ± 0.01	0.44 ± 0.01	0.54 ± 0.01	2.79 ± 0.05
τ_{DA}^{NP}	0.41 ± 0.01	0.80 ± 0.02	0.59 ± 0.01	4.05 ± 0.09

CHAPTER 3

ANOMALOUS YET BROWNIAN

Adapted with permission from Bo Wang, Stephen M. Anthony, Sung Chul Bae, and Steve Granick (2009) Anomalous yet Brownian, Proceedings of the National Academy of Sciences of the United States of America, 106, 15160-15164. Copyright 2009 National Academy of Sciences.

3.1 Background

The supposition that Brownian motion follows Gaussian statistics is seldom tested experimentally. In fact, there are few physical situations in which the statistics of displacement distribution can be measured directly. More often, one simply verifies that mean square displacement is proportional to time, which defines a diffusion coefficient, D. However, a finite diffusion coefficient does not necessarily stem from a Gaussian distribution, since D only holds information regarding second-order cumulants but not the full probability distribution of displacements [1]. Relaxation functions in Fourier space are also heavily relied upon in experimental tests of theories that assume Gaussian statistics, but the limited signal-to-noise ratio in measuring these quantities does not typically allow one to deduce distribution functions in real space with the large dynamic range presented by the experiments described below. It is easy to show formally that other zero-centered distributions than Gaussian, in particular exponentially decaying probability distributions of displacement amplitude, would also lead formally to mean-squared displacement proportional to time.

Here, using single-particle tracking [2], we report the full displacement probability during Brownian motion in two complex liquid systems, and conclude that the distribution of

displacement probability is exponential for large displacements, the variance of the exponential being proportional to time. This is reminiscent of the exponential rather than Gaussian displacement distributions that have been observed in glassy systems and in those systems is believed to originate in activated hopping [3-6]. The new point is two-fold: first the finding that this is combined with Fickian diffusion, $\left\langle \Delta r^2 \right\rangle \propto t$, and secondly that the decay length of the exponential, $\lambda(t)$, grows with the square root of time, t. We also compare to particle trajectories that are subdiffusive at the earliest measurement times but Fickian at the longest measurement times, finding that the displacement probability distributions fall onto the same master curve for both regimes. The fact that $\lambda(t) \propto \sqrt{t}$ is more generic than $\left\langle \Delta r^2 \right\rangle \propto t$ is striking.

Beyond the two independent systems described in this study, in which this pattern was observed by direct measurement, discussion at the end of this chapter leads us to anticipate that this non-Gaussian diffusion may be common in other complex liquids with slow environmental fluctuations whose wavelength exceeds the size of the diffusing element.

3.2 Results

Colloidal beads on phospholipid bilayer tubes

Fig. 3.1 shows a schematic diagram as colloidal particles were imaged as they diffused on tracks composed of lipid bilayer tubes at concentrations so low that they did not interact with one another. A representative image is shown in Fig. 3.2. The anionic particles adsorbed strongly to the zwitterionic lipid headgroups [7], presumably owing to charge-dipole attraction, and were observed to never leave the tubes although they diffuse along them. Although tubes of various diameters formed using the preparation protocol, we analyzed only those straight tubes with diameter of ~100 nm (estimated from the colloid transverse vibration range) that lacked long-range vibrations when they lay on the surface of the glass sample cell. To exploit the simplicity of

one dimension, the particle diameter was kept the same as the tube diameter, ≈100 nm, with the added advantage that for this size, thermal fluctuation significantly outweighed gravity and the length scale of 100 nm exceeded that of the lipid molecules and the particle roughness, allowing the desired long-range motions to be abstracted. At the experimental temperature, 22-23 ˚C, these lipids were in the fluid phase. An illustrative 1-dimensional trajectory is shown in Fig. 3.2. From data of this kind we calculated the ensemble-average mean square displacement (MSD), $\left\langle \Delta x^2(t) \right\rangle = \left\langle \left| x(t) - x(0) \right|^2 \right\rangle$ where x is position and t time, and brackets denote averaging over hundreds of trajectories. Fig. 3.1b (upper line) shows that MSD is proportional to time over our observation time window – classical Brownian motion.

The relation $\left\langle \Delta x^2(t) \right\rangle = 2Dt$, where D is the translational diffusion coefficient, implies $D = 0.4\ \mu m^2 \cdot s^{-1}$ for particles. This value is strikingly fast, ≈20% of the value in free dilute suspension, even though the viscosity of lipid bilayers is about a hundred times higher than the viscosity of bulk water and the particles never left the surface track. Exploring further, we compared our experimental values to diffusion upon solid-supported lipid bilayers formed from the fusion of single unilamellar vesicles of these same lipids [8] and found slower diffusion for bilayers, a two-dimensional diffusion $D = 0.01\ \mu m^2 \cdot s^{-1}$, which agrees with literature [9]. While it is true that diffusion on the supported bilayer is expected to be slower than diffusion along the tubes owing to friction from the solid substrate underneath, such reduction is expected to be on the order of a factor of two, the amount that friction from the supporting substrate reduces diffusion in supported bilayers compared to free-standing giant unilamellar vesicles [10]. The much larger difference in diffusion observed is believed to result from coupling to thermal fluctuation of the membrane. Such fluctuations *without* adsorbed particles have been studied both theoretically and experimentally [11,12]. Although fluctuation in the presence of an adsorbed particle might be perturbed, it is reasonable that fluctuations continue to be significant, albeit

perturbed, given that particle adsorption can drastically deform membranes [13] and disturb the Goldstone modes of lipid tubules [14].

In another control experiment we mixed 40% cholesterol into the tubes to stiffen and tighten them [15]. The mean-squared displacement remained Brownian but with smaller *D*, 0.012 μm^2-s^{-1} (Fig. 3.1b, bottom line). This cannot be attributed to viscosity change, as cholesterol increases viscosity by only ≈20% [16]. Noting that cholesterol largely suppresses membrane fluctuations, reducing their amplitude by an order of magnitude, this further supports the hypothesis that membrane fluctuations speed up diffusion. In other control experiments we also observed that adsorbed DNA displays enhanced diffusion, enhanced by roughly the same factor as these rigid colloid particles. The result seems generic.

From the analysis of hundreds of trajectories, the probability distribution of particle displacement, $G_s(x,t) = \left\langle \delta\left(x - \left|x_i(t) - x_i(0)\right|\right)\right\rangle$ where $x_i(t)$ denotes the projected position along the tube of particle *i* at time t, are reported in Fig. 3.1. Logarithmic $G_s(x,t)$ is plotted against displacement normalized by particle diameter, σ, for particles diffusing on tubes of dilauroylphosphatidylcholine (DLPC), and the distribution was observed to decay linearly on a semilog plot for observation times up to several seconds. Phenomenologically, $G_s(x,t) = \frac{1}{\lambda(t)}\exp\left(-\frac{|x|}{\lambda(t)}\right)$. However, beyond t ≈ 4 sec, the exponential decay smoothly reverted to Gaussian decay, becoming indistinguishable from Gaussian decay within a couple of seconds. Though the statistics change in this major qualitative way, the mean-square displacement remains Fickian with the same diffusion coefficient throughout.

The decay length $\lambda(t)$ grows as the square root of the time over which displacements are measured, $\lambda(t) \propto \sqrt{t}$ (Fig. 3.3a), which is consistent with linear MSD. Consequently, the probability distributions collapse to form a master curve if normalized by λ(t) (Fig. 3.3b). For

comparison, Fig. 3.3b also shows the hypothetical Gaussian distribution that would give this same proportionality between mean-square displacement and elapsed time; one observes fewer small steps than in the Gaussian distribution and more long steps, even though the implied diffusion coefficient is the same. Finally, for the control experiment of diffusion on stiffer tubes (tubes containing cholesterol), the probability distribution was simply Gaussian regardless of the time scale of the step.

Colloidal beads in entangled actin suspensions

The schematic diagram in Fig. 3.4a illustrates this system: transport of solute particles (blue sphere) through the porous structure created by surrounding entangled macromolecular filaments (grey) whose translational diffusion is known from many studies of F-actin networks to be slow relative to this transport. These are semiflexible filaments [17].

The trajectories of dilute nanoparticles were followed as they diffused through entangled F-actin networks (Fig. 3.5). The filament lengths of 2 – 20 μm were comparable to the persistence length of ~15 μm [17]. Potential non-specific adsorption to actinwas excluded by coating the particles (fluorescent carboxylate-modified polystyrene spheres) with BSA, a widely used blocking protein. The F-actin concentration was kept sufficiently low that the networks remain isotropic.

A pioneering study by Weitz and coworkers on a similar system analyzed patterns of subdiffusive behavior when the ratio of particle size to mesh size was increased [18]. Here, we focused on selected values of particle radius (a) and mesh size (ξ) such that displacement was Fickian over times as short as we could measure, as short as 50 msec, and analyzed the full distribution of displacement probability instead. As an extension, we also examined the situation where diffusion was subdiffusive for some window of observation time but was Fickian in the long-time limit.

Strictly Fickian behavior was observed in the least-obstructed systems, which are within $a/\xi < 0.15$ (Fig. 3.4), to show the generality of Fickian behavior when both particle size and mesh size were varied. For Fickian diffusion, classically one expects Gaussian decay, $G_s(r,t) \propto \exp\left(-\frac{r^2}{4Dt}\right)$, where D is the diffusion coefficient, and $r(t)$ denotes the two-dimensional projection of displacement in time t. This is consistent with the data when the displacement is small, but for larger displacements the data are definitively exponential instead, $G_s(r,t) \propto \exp\left(-\frac{r}{\lambda}\right)$ (Fig. 3.4c).

One expects in principle the displacement distribution to revert to Gaussian at sufficiently long times, but this was not observed, perhaps because the system relaxation time estimated from rheology measurements on similar F-actin networks (>1000 sec) so much exceeds the time on which these experiments were conducted [19]. In fact, it was the opposite: the contribution of the central portion that could be fitted as Gaussian decreased with time elapsed. Inspection shows that the crossover point from Gaussian to exponential occurs approximately at the distance $(\xi - 2a)/2$, which is the average distance between particle and filaments. When the distributions spread with increasing observation time, this crossover point did not. The result is that the exponential parts took larger and larger portions of the overall distribution. This then suggests that the exponential arises from interaction between particle and filaments, although a molecular explanation is not the main subject of this study. Furthermore, the dashed line in Fig. 3.4c shows the hypothetical Gaussian distribution that would lead to the diffusion coefficients implied by the raw data in Fig. 3.4b. Just as for the first system described in this chapter, in the observed probability distribution one observes fewer small steps than in the Gaussian distribution and more long steps, even though the implied diffusion coefficient (D) is the same.

Also in common with the first system described in this study, the temporal evolution of $G_s(r,t)$ reveals that the exponential tail spreads with time. In Fig. 3.6, the plot on log-log scales shows $\lambda(t) \propto \sqrt{t}$ over two orders of magnitude of *t*.

We now compare trajectories that span subdiffusive, crossover, and Fickian diffusion regimes (Fig. 3.6a, the system with a/ξ ~ 0.3). It is evident that the displacement distribution is exponential in all three regimes and that the decay lengths of the exponential collapse onto the same curve in Fig. 3.6b (circles). Again, probability distributions collapse to form a master curve when normalized by λ(t) (Fig. 3.6a inset), showing universal exponential tails and Gaussians disappearing with time. The fact that $\lambda(t) \propto \sqrt{t}$ is more generic than $\langle \Delta r^2 \rangle \propto t$ is striking.

3.3 Discussions

We focus below on generic aspects of these observations but first make some system-specific comments. For the first system described here, colloids on lipid tubules, physically one expects slow entropic forces to promote diffusion because adsorption perturbs spontaneous membrane fluctuations. For the second system described here, colloids in actin networks, entropic forces arise from coupling between these diffusing particles and transverse fluctuations of actin filaments. Considering that the presence of particles might modify the thermal fluctuation of the environment as well, it is reasonable to speculate that these phenomena have an intermittent nature consisting of a long sequence of stochastic bursts resulting in a broad distribution of time scales; analysis along these lines is presented in Supporting Information. The main point is experimental, the ubiquitous observation of exponential tails.

Regarded just on its own, data for the second system might suggest activated diffusion between pores in the entangled F-actin networks, in the same spirit as activated diffusion and exponential tails observed in glassy systems [3,4]. But data for the first system show diffusion

nearly as rapid as for the same colloids in free suspension. While the exponential tail is reminiscent of slow dynamics in glassy system, in fact these dynamics are exceptionally rapid.

Continuous-time random walk (CTRW) models

We compare the experimental van Hove functions in the frequency domain by performing the discrete Fourier-Laplace transform of $G_s(x,t) \to F_s(k,u)$ on these data, with those calculated functions from the continuous time random walk (CTRW) model. Inputting the conjectural jumping length $\psi(k)$ and pausing time $\varphi(u)$ distributions into the Montroll-Weiss equation, $F_s(k,u) = \frac{1-\varphi(u)}{u} \frac{1}{1-\psi(k)\varphi(u)}$, best "fittings" are achieved with power-law distributions both for displacements, $\psi(x) \sim x^{-1-\beta}$, and time intermittency, $\varphi(\tau) \sim \tau^{-1-\alpha}$, within the range of $0.3 \le \beta < 0.5, 2\alpha \approx \beta$ for colloid diffusion on lipid tubule (Fig. 3.7). It is consistent to observe the relation between exponents, $2\alpha \approx \beta$. This satisfies the linear MSD we observed, since according to CTRW model, this relation corresponds to a complicated spatiotemporal correlation, $\langle \Delta x^2(t) \rangle \sim t^{2\alpha/\beta}$ [20].

Another similar model considers a dynamic disordered landscape with stochastic potential barriers chosen to have a finite lifetime. Simulation shows crossover from Fickian (and Gaussian) behavior, to Fickian and exponential behavior when the barrier lifetime exceeds the mean collision time between particle and barrier.

Taken together, the common difficulties in evaluating this sort of model are two-fold. First: how to legitimize on physical grounds the fitting parameters? Second: how to rationalize that the probability distribution function described not only slow dynamics (the second system) but also enhanced diffusion (the first system)?

"Diffusing diffusivities" scenario

Another line of explanation, attractive in its simplicity, is to assume that the exponential tail of the probability distribution is a series of Gaussian distributions with different variance. Then the total can be written as $G(x) = \sum p(x)\varpi(\sigma)$ where $\varpi(\sigma)$ is the weight of the Gaussian distribution with given variance. Approximately, the sum can be performed by integration which gives $G(x) \sim \exp\left(-\frac{|x|}{\lambda}\right)$, assuming that $\varpi(\sigma) \sim \exp\left(-\frac{\sigma^2}{t}\right)$. It follows that $\lambda \sim \sqrt{t}$. Since each elemental process is diffusive, the variance of the total should be $\lambda^2 \sim t$ – also diffusive. In this interpretation, the enhanced diffusion observed in our first system reflects contributions from those Gaussians with large variances. Physically, each Gaussian connects to a certain level of force on the particle as a consequence of the central limit theorem and the weightings reflect Boltzmann distributions of those states [1]. Observed in the laboratory frame as we have done in this experimental study, diffusion is then the superposition of a packet of diffusive processes (Fig. 3.8). In other words, the systems have diffusivity memory, that particles diffusing faster are likely to keep diffusing faster for some time, but there is no directional persistence for diffusive cases and weak anti-persistence for sub-diffusive cases.

These arguments are similar in spirit to notions about distributions of dynamic activity in supercooled liquids [21,22]. For this picture to be consistent, dynamic heterogeneity must flip very fast in our systems. On the one hand, this is supported by the observations of Fickian diffusion, no significant velocity autocorrelation on the experimental time scales, and exchange and persistence time distributions that are nearly the same. This contrasts to glasses, where correlations of heterogeneity are long-lived, finally leading to bistability of trajectories [23] and spatial distribution of fast and slow populations [24]. On the other hand, there are difficulties. It is not clear how to justify the assumption of independent Gaussian processes when they are highly entangled, nor that variances are related to one another in this assumed way. Also, one must

establish explicitly the connection between environmental fluctuations and dynamic heterogeneity in trajectory space.

3.4 Conclusions

The data presented in this chapter raise fundamental questions concerning what is the statistical nature of the diffusive process, when the physical situation is such that the assumption of Einstein's classic derivation of Brownian motion are not satisfied. It is our hope that this experimental study will call renewed theoretical and experimental attention to the problem of random walks under conditions where the environment fluctuates on similar time scales as the random walk itself.

3.5 Materials and Methods

Colloidal beads on phospholipid bilayer tubes

Tubular lipid vesicles were produced by drying a suspension of liposomes composed of dilauroylphosphatidylcholine (DLPC, Avanti Polar Liquids, Inc.) on a clean glass slide, followed by prehydration in water vapor and then hydration in water or buffer. Tubes form with diameters ranging from 100 nm to 1 μm and lengths of several hundred microns. Carboxylate-modified fluorescent colloidal polystyrene spheres with diameter σ = 100 nm (Interfacial Dynamics Corp.) were added after the phospholipid tubes relaxed.

Colloidal beads in entangled actin suspensions

Lyophilized G-actin (rabbit skeletal muscle, Cytoskeleton Inc.) was reconstituted in fresh G-buffer (5 mM TRIS (tris(hydroxymethyl)aminomethane) at pH 8.0, supplemented with 0.2 mM $CaCl_2$, 1 mM ATP, and 0.2 mM dithiothreitol (DTT) and 0.01% NaN_3) at 4 ºC and used within 7 days of reconstitution. G-actin was polymerized into F-actin by the addition of salt (100mM KCl,

2mM $MgCl_2$), in the presence of gelsolin (human plasma, Cytoskeleton Inc.) to control the length of the filaments [17]. In other control experiments, the ATP concentration was varied to show no dependence of observations on ATP level (0.1 – 1 mM), thus confirming that treadmilling, whose time scale is hours [17], is negligible for the duration of these experiments.

Fluorescent tracer particles, carboxylate modified colloidal polystyrene nanospheres (Molecular Probes), were coated with bovine serum albumin (BSA, Sigma-Aldrich), a widely used blocking protein, to preclude non-specific adsorption. The extra BSA was removed from the solution by repeated centrifugation (25,000×g for 30 min) and washing. The possible aggregates were filtered out by passing the modified particles though PVDF membranes (Millipore) with pore size cutting off single nanospheres. Modifying the surface has only small effect on the particle motion.

The probes were added into G-actin solutions at concentration ~10^{-15} M immediately before polymerization. After mixing and polymerization, the samples were stabilized on the microscope stage for at least 4 h. We focused ~100 μm into the sample to avoid wall effects. To reduce the noise in displacement probability distribution, approximately 100 particles were imaged in the field of view, and ~50 movies were taken from 3-5 samples for each condition.

Single-particle tracking

The samples were imaged using a homebuilt setup for epifluorescence microscopy with a diode-pumped Nd:YAG laser (CrystaLaser) excitation source [2]. The laser was focused to the back focal point of an air objective (LD Neofluor 63×, NA = 0.75), causing the beam out of the objective to be parallel and homogeneous. Fluorescence excited was collected through the objective and detected by a back-illuminated electron multiplying charge-coupled device (CCD) camera (Andor iXon DV-897 BV). The total system magnification of the CCD was 100 nm-pixel. Fluorescence images were collected typically at the speed of 20 frames/s for 500 s. The video images were converted into digital format and analyzed using single-particle tracking programs,

locating the center of each particle in each frame, and then stringing these positions together to form trajectories, using software written in-house [2]. The accuracy was ~10 nm.

For the case of particles diffusing on lipid tubules, before the movies can be analyzed using standard particle tracking algorithms, the fluorescent contribution of the tubes must be subtracted. We exploited their effectively constant contribution. For the majority of the time, the intensity of a pixel reflected the background value with a small noise component. Thus, if we average the value of a pixel over all times after discarding the brightest quarter, we obtain an almost perfect background image. Some distortion persists as the average value at those locations where a particle was never present will be slightly too low, but this deviation is minimal and acceptable, as this random noise is trivial compared to tube fluorescence. This has the beneficial side effect of excluding fixed particles from consideration. Finally, the trajectories are projected to the axis parallel to the extending direction of the tubes, for further statistical analysis.

3.6 References

1. McLennan JA (1989) *Introduction to Non-equilibrium Statistical Mechanics*, (Prentice Hall, Englewood Cliffs).
2. Anthony S, Zhang L, Granick S (2006) Methods to track single-molecule trajectories. *Langmuir* 22: 5266-5272.
3. Chaudhuri P, Berthier L, Kob W (2007) Universal nature of particle displacements close to glass and jamming transitions. *Phys. Rev. Lett.* 99: 060604.
4. Saltzman EJ, Schweizer KS (2008) Large-amplitude jumps and non-Gaussian dynamics in highly concentrated hard sphere fluids. *Phys. Rev. E* 77: 051504.
5. Bailey NP, Schrøder TB, Dyre JC (2009) Exponential distributions of collective flow-event properties in viscous liquid dynamics. *Phys. Rev. Lett.* 102: 055701.

6. Stariolo DA, Fabricius G (2006) Fickian crossover and length scales from two point functions in supercooled liquids. *J. Chem. Phys.* 125: 064505.
7. Wang B, Zhang L, Bae SC, Granick S (2008) Nanoparticle-induced surface reconstruction of phospholipid membranes. *Proc. Nat. Acad. Sci. USA* 105: 18171-18175.
8. Zhang L. Granick S (2005) Slaved diffusion in phospholipid bilayers. *Proc. Nat. Acad. Sci. USA* 102: 9118-9121.
9. Ewers H, *et al.* (2005) Single-particle tracking of murine polyoma virus-like particles on live cells and artificial membranes. *Proc. Natl. Acad. Sci. USA* 102: 15110-15115.
10. Przybylo M, *et al.* (2006) Lipid diffusion in giant unilamellar vesicles is more than 2 times faster than in supported phospholipid bilayers under identical conditions. *Langmuir* 22: 9096-9099.
11. Leitenberger SM, Reister-Gottfried E, Seifert U (2008) Curvature coupling dependence of membrane protein diffusion coefficients. *Langmuir* 24: 1254-1261.
12. Kaizuka Y, Groves JT (2006) Hydrodynamic damping of membrane thermal fluctuations near surfaces imaged by fluorescence interference microscopy. *Phys. Rev. Lett.* 96: 118201.
13. Deserno M (2004) Elastic deformation of a fluid membrane upon colloid binding. *Phys. Rev. E* 69: 031903.
14. Fournier J–B, Galatola P (2007) Critical fluctuations of tense fluid membrane tubules. *Phys. Rev. Lett.* 98: 018103.
15. Koster G, VanDuijin M, Hofs B, Dogterom M (2003) Membrane tube formation from giant vesicles by dynamic association of motor proteins. *Proc. Natl. Acad. Sci. USA* 100:15583-15588.
16. El-Sayed MY, Guion TA, Fayer MD (1986) Effect of cholesterol on viscoelastic properties of dipalmitoylphosphatidylcholine multibilayers as measured by a laser-induced ultrasonic probe. *Biochemistry* 25: 4825-4832.

17. Sheterline P, Clayton J, Sparrow JC (1998) *Actin*, (Oxford University, New York, ed. 4).
18. Wong IY, *et al.* (2004) Anomalous diffusion probes microstructure dynamics of entangled F-actin networks. *Phys. Rev. Lett.* 92: 178101.
19. Janmey PA, *et al.* (1994) The mechanical properties of actin gels: elastic modulus and filament motions. *J. Biol. Chem.* 269: 32503-32513.
20. Baskin E, Iomin A (2004) Superdiffusion on a comb structure. *Phys. Rev. Lett.* 93: 120603 (2004).
21. Merolle M, Garrahan JP, Chandler D (2005) Space-time thermodynamics of the glass transition. *Proc. Natl. Acad. Sci. USA* 102: 10837-10840.
22. Xia X, Wolynes PG (2001) Microscopic theory of heterogeneity and nonexponential relaxations in supercooled liquids. *Phys. Rev. Lett.* 86: 5526-5529.
23. Hedges LO, Jack RL, Garrahan JP, Chandler D (2009) Dynamic order-disorder in atomistic models of structural glass formers. *Science* 323: 1309-1313.
24. Swallen SF, Bonvallet PA, McMahon RJ, Ediger MD (2003) Self-diffusion of tris-naphthylbenzene near the glass transition temperature. *Phys. Rev. Lett.* 90: 015901.

3.7 Figures

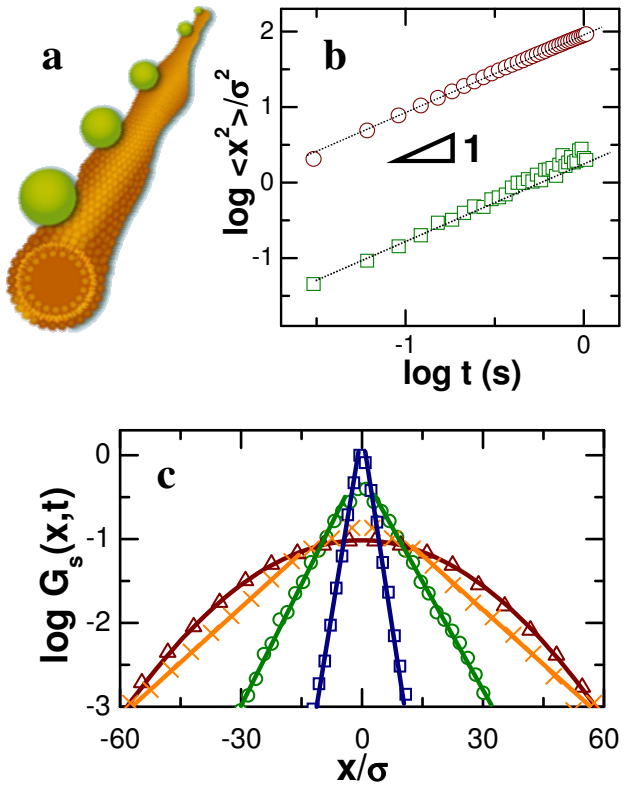

Figure 3.1

The first system: colloidal beads diffusing on lipid tubules. (a) Schematic representation of particles with diameter σ = 100 nm, separated by distances >100 σ, diffusing on linear tubes of phospholipid bilayers. (b) Mean-squared displacement, normalized by particle diameter squared, plotted against time on log-log scales for particles on lipid tubes composed of pure DLPC bilayers (upper line) and tubes composed of DLPC bilayers containing 40% cholesterol (bottom line). The lines have slope of unity. (c) From the analysis of hundreds of trajectories without statistical difference, the displacement probability distribution of particles on lipid tubes composed of pure DLPC bilayers is plotted logarithmically against linear displacement normalized by particle diameter for several representative values of time step: 60 ms (squares), 0.6 s (circles), 3 s (crosses) and 5.8 s (triangles).

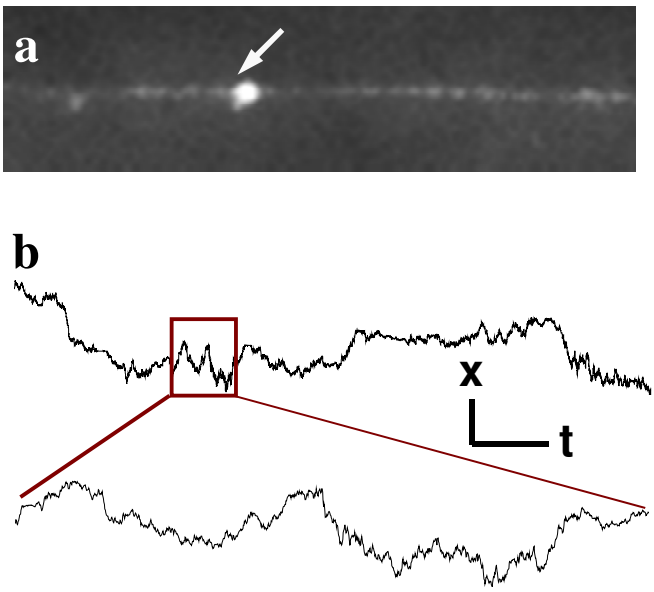

Figure 3.2

(a) Representative image of a particle diffusing on a lipid tubule. The arrow shows the particle. The image size is 5 μm × 20 μm. Image analysis allows us to measure relative displacements of 20 nm. (b) Representative trajectory parallel to the tube extension. The coordinate scales in the top trace are 10 σ and 50 sec. In the bottom trace, the scales are 4.5 σ and 5 sec. Each time step is 30 ms.

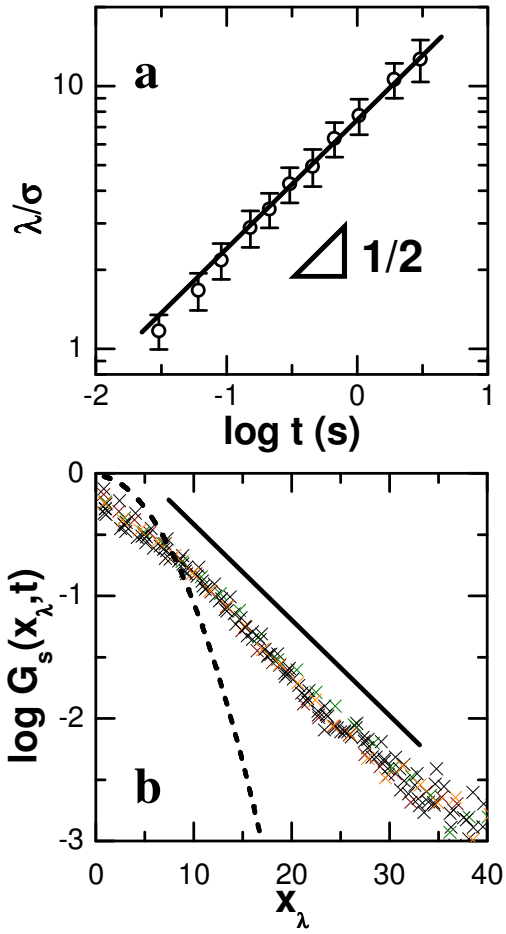

Figure 3.3

Time evolution of exponential tails in displacement distribution. (a) The decay length $\lambda(t)$, plotted versus delay time on log-log scales, shows a square root power law for nanoparticles diffusing on lipid tubules. (b) Master curve obtained by normalizing the probability distribution by the square root of the time step, $x_\lambda = x(t)/\sqrt{t}$, with delay times ranging from 30 ms to 1 s. The solid line, a guide to the eye, shows semilogarithmic behavior. The dotted line shows Gaussian behavior with the same diffusion coefficient.

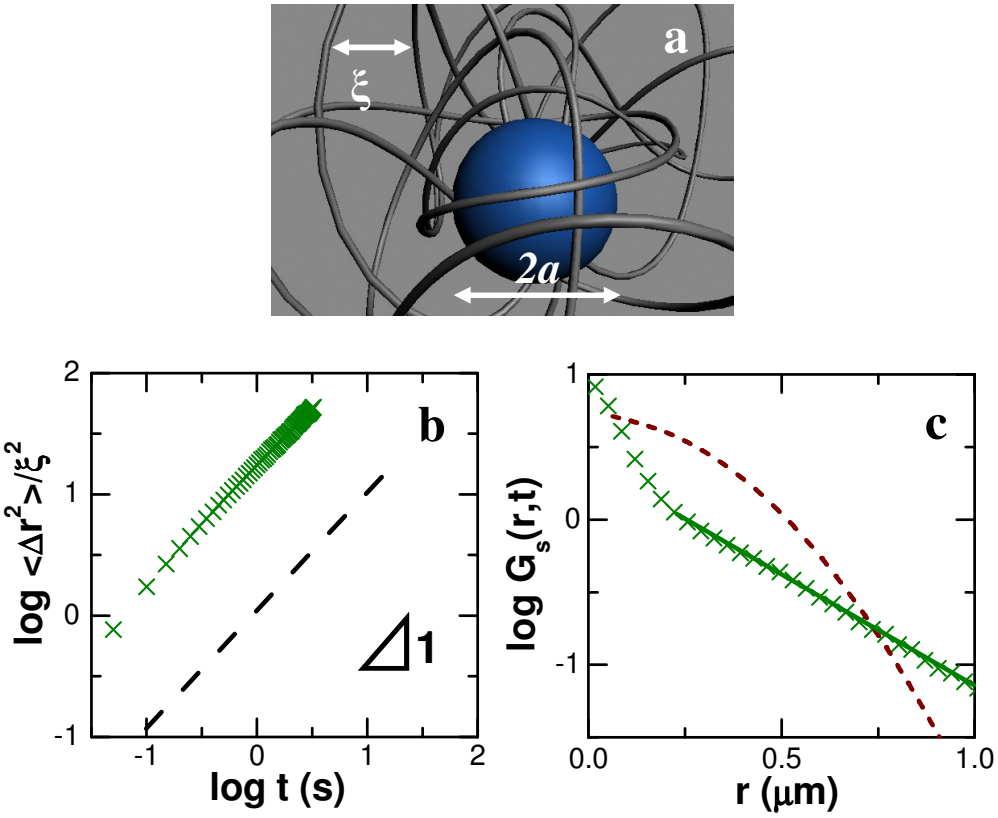

Figure 3.4

The second system: Nanospheres diffusing in entangled actin. (a) Schematic representation of particles diffusing in entangled actin networks. The mesh size (average spacing between filaments) in nm can be estimated as $\xi = \frac{300}{\sqrt{c}}$, where c is actin concentration in mg/mL. Their concentration is semi-dilute. The average particle-particle separation is ≈10 μm and their radius is a = 25 - 250 nm. (b) Mean square displacement (MSD) normalized by mesh size squared, plotted against time t on a log-log scale for particles in entangled F-actin at conditions of a = 50 nm, ξ = 300 nm, showing a slope of unity. (c) Corresponding displacement probability distributions $G_s(r,t)$ plotted logarithmically against linear displacement for delay time of 0.1 s. Here, $G_s(r,t)$ can be fitted with a combination of a Gaussian at small displacement and exponential at large displacement (solid line). In (b) the dashed line is MSD constructed according to the central Gaussian part in the displacement distribution. In (c), the dashed line shows a Gaussian distribution with the same diffusion coefficient as for (b).

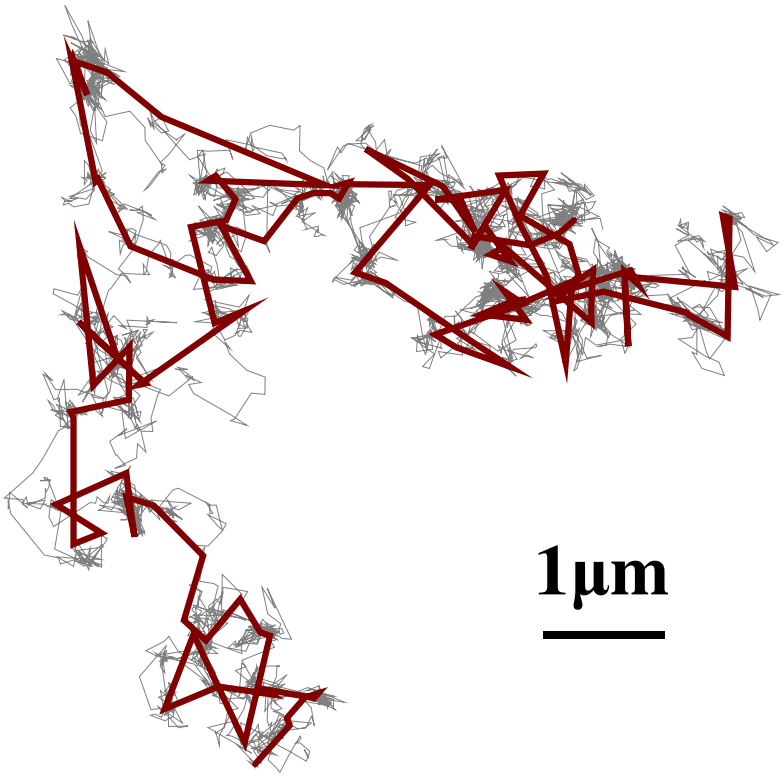

Figure 3.5

A typical trajectory of particle (a = 100 nm) diffusing in entangled F-actin (ξ = 300 nm) projected onto the x-y plane with 50 msec between frames (grey) or 2 sec between frames (red), measured for 250 sec. The eye distinguishes local vibrations and long jumps (gray line); for this sampling time, motion is determined to be subdiffusive, a pattern familiar in colloidal systems and commonly attributed to "caging". Increasing the time period of temporal sampling by a factor of 40 (red line) makes the long jumps more obvious to the eye, corresponding to reversion of motion to Fickian.

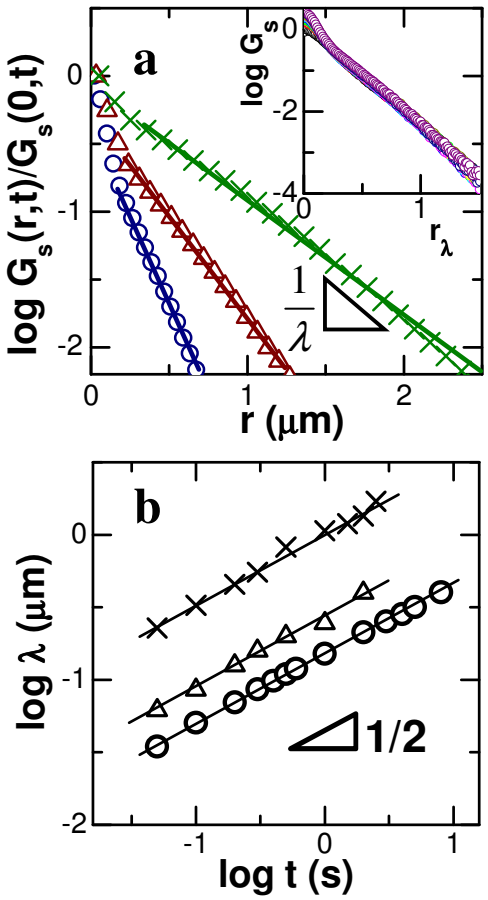

Figure 3.6

Temporal evolution of the displacement probability distributions. (a) $G_s(r,t)$ for diffusion of particles with radius 100 nm in F-actin (ξ = 300 nm) at delay time t: 1 s (circles), 5 s (triangles) and 20 s (crosses). Inset: master curve obtained by normalizing the probability distribution by the square root of the time step, $r_\lambda = r(t)/\sqrt{t}$, with delay times ranging from 50 ms to 5 s. (b) Decay lengths $\lambda(t)$ defined in panel A are plotted against time on log-log scales. Experimental conditions are a = 50 nm, ξ = 300 nm (crosses); a = 100 nm, ξ = 450 nm (triangles); and a = 100 nm, ξ = 300 nm (circles). Lines have slopes of 1/2. The uncertainty in fitting is less than the symbol size.

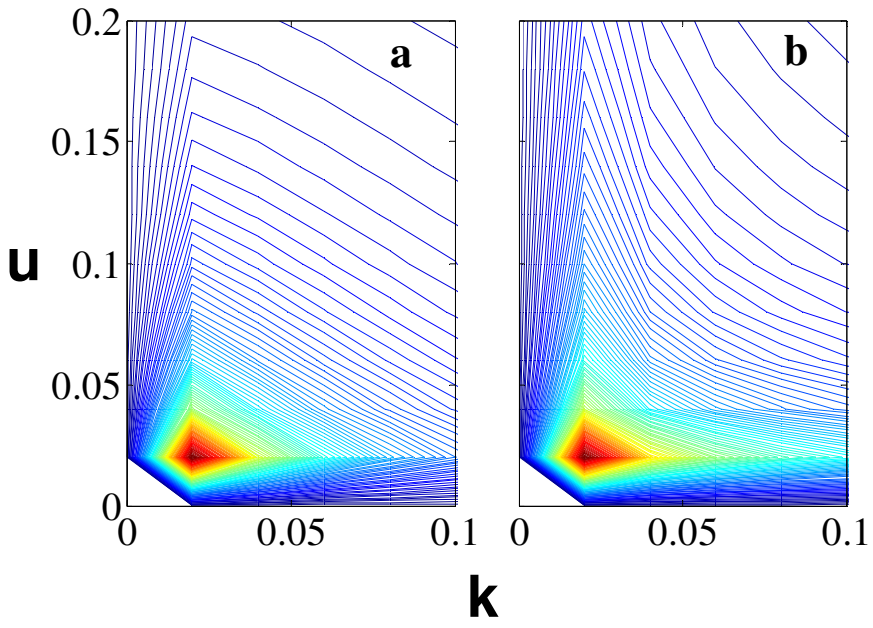

Figure 3.7

Contour plots of the self-part of van Hove functions of nanoparticles diffusing on lipid tubules in Fourier-Laplace domain obtained by inverse transforms of the distribution from (a) experiments and (b) simulated from Montroll-Weiss equation, with $\alpha = 0.2, \beta = 0.4$.

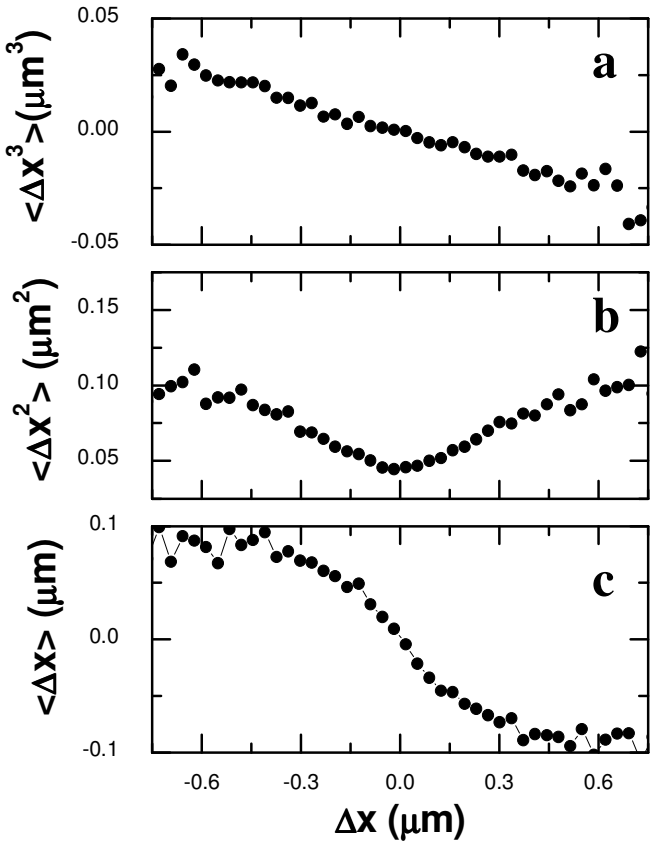

Figure 3.8

Conditional mean k-th (k=1,2,3) moments of displacements during the subsequent time interval given the displacements within time interval of 250 ms, for diffusion of particles with radius 100 nm in F-actin (ξ = 300 nm). At this condition, the dynamics is sub-diffusive. For the diffusive conditions, such as a = 50 nm, ξ = 300 nm, the first and third moments are zero, while the second moment has similar shape as shown in (b).

CHAPTER 4

THE CONFINING POTENTIAL WHEN A BIOPOLYMER FILAMENT REPTATES

Adapted with permission from Bo Wang, Juan Guan, Stephen M. Anthony, Sung Chul Bae, Kenneth S. Schweizer and Steve Granick (2010) The confining potential when a biopolymer filament reptates, Physical Review Letters, 104, 118301. Copyright 2010 American Physical Society.

4.1 Background

Polymer entanglement is imperfectly understood [1,2]. This impedes much progress, from processing of plastics to transport in the cell cytoskeleton. Historically it is modeled [1-3] with increasing sophistication as "reptation" of linear chains within a "tube" along a coarse-grained snake-like "primitive path" [4-7], but too little is known from experiment about the confining potential, a dynamical property that describes transient localization on time scales less than the disentanglement time, owing to the paucity of methods to do so.

Researchers in this field have been well aware of the desirability of this goal. In addition to the voluminous literature comparing models to measurements of mechanical properties and diffusion [6,8], which is indirect, we call attention to the direct measurements. The pioneering work of Sackmann confirmed anisotropy of diffusion for the system that we study here [9], semi-flexible filaments of F-actin, but was limited by colloidal bead markers attached to actin. Force measurements were made by dragging DNA through other similar DNA molecules [10] but nonlinear flows complicated interpretation. Computer simulations [6,11] to date are limited to modest degrees of entanglement, $N/N_e \approx 10$ or less (N degree of polymerization, N_e entanglement

onset). Here a novel fluorescence approach enables us to quantify distributions of monomer displacement normal to the primitive path for $N/N_e \approx 100$, with subdiffraction resolution. These measurements refer to times far shorter than the disentanglement time, ≈100 min for this system [4,11], and thus define a "confining potential" [12].

4.2 Results and Discussions

F-actin networks are chosen since the filaments are long enough to be visualized by fluorescence microscopy (Fig. 4.1a). The mean filament length (number averaged, L_n) of 23 μm has, from this sample preparation, weight-average to number-average polydispersity, L_w/L_n, of 1.3, and persistence length ~17 μm [13]. Semi-flexibility implies that "tube leakage", random looping between discrete entanglements, is unlikely. Sub-diffraction spatial resolution is achieved by *sparse* fluorescent labeling.

The experiment begins by mixing trace labeled probe filaments with entangled unlabeled filaments (0.2-2 mg/mL). Probe filaments are constructed by annealing short segments (~100 nm long), generated by passing a mixture of Alexa-568 labeled and unlabeled F-actin at a ratio of 1:10 through a 26 gauge syringe needle six times, then fixing the annealed filaments with phalloidin to prevent treadmilling and depolymerization [14]. Annealing proceeds for >12 h. Brownian motion of labeled segments was viewed in an epifluorescence microscope with air objective (63x, N.A. = 0.75) to focus deep into the sample (>100 μm) to avoid potential wall effects. Video images were digitized and analyzed using software written in-house [15]. Local changes in positions of labeled monomers are resolved with 10 nm precision (Fig. 4.1b).

Representative time traces of fluorescent labels along F-actin filaments show the expected reptation (Fig. 4.1c). We identify the primitive path by a B-spline fitting of the position point cloud using a squared distance minimization algorithm, and calculate the minimum distance

$r_\perp$ from every measured point to the primitive path with a quadratic approximation (Fig. 4.2) [16]. This one dimensional projection of the transverse fluctuation distance within the tube brings an extra experimental uncertainty of <10 nm, estimated from the variance of a single distance calculated from fitting with different initial conditions. As the average spacing between labels along the filaments exceeds the persistence length, this excludes potential spatial correlations of measured transverse fluctuations. Chain ends were excluded from analysis. Trajectories lasting 300-700 seconds were analyzed with a frame rate (0.5 sec) sufficiently slow that bending fluctuations, which are on the msec time scale [17], did not contribute. This time scale is longer than the entanglement time, the time that the movement of the filaments starts to become sterically confined by their neighbors [11].

In Fig. 4.3, histograms of root-mean-squared (RMS) transverse fluctuations, $\sqrt{\langle r_\perp^2 \rangle}$, of single time traces of filaments are shown for two actin concentrations. The right-skewed shapes deviate from the classical tube radius notion.

The ensemble-average dynamical confining potential felt by an actin monomer, $V(r_\perp)$, is extracted by combining the full trajectories from all filaments using the relation [9,12]: $\frac{V(r_\perp)}{k_B T} = -\ln \frac{P(r_\perp)}{P(0)}$, where $P(r_\perp)$ is the transverse distance probability distribution, and $k_B T$ is the thermal energy. Experimental limitations preclude measurement of the (expected weak for $N \gg N_e$) time dependence of $V(r_\perp)$ [12]. Fig. 4.4a shows an example of the displacement probability distribution spanning three orders of magnitude of transverse fluctuation. Data for a single filament (crosses) agrees with the ensemble average for many filaments (circles) though the former is noisier, showing that fluctuation on the single filament level is well represented by the ensemble distribution. For the first logarithmic decade of probability distribution, the transverse distance $r_\perp$ agrees with the classical picture of a harmonic constraining potential, the

Gaussian probability distribution $P(r_\perp) \propto \exp\left(-\frac{r_\perp^2}{R_e^2}\right)$, where R_e is the tube radius defined as the distance beyond which the constraining potential exceeds $k_B T$. Beyond this, it is better described by an exponential decay, $P(r_\perp) \propto \exp\left(-\frac{|r_\perp|}{\lambda}\right)$. This is the case for probabilities < 0.1, corresponding to a constraining potential of ~$2k_B T$ or more, a regime not probed in prior studies [9]. At other actin concentrations, the distribution was similar except that it broadened as concentration decreased. The concentration range studied was limited by the requirement to achieve entanglement at the low end and to avoid nematic ordering at the upper end [18].

Fig. 4.4b shows an effective equivalent restoring force, $-\frac{dV_\perp}{dr_\perp}$, plotted against the transverse distance. For small displacements, force increases linearly with transverse distance and the spring constant is the slope, as postulated in classic tube or slip-link models. But in the large displacement regime, the restoring force is constant and ~10 – 100 fN, the value depending on actin concentration. This softening is not included in theories of polymer dynamics of which we are aware. However, for these semidilute solutions whose mean concentration is so very small ($\approx 10^{-4}$ in terms of volume fraction for actin) large concentration fluctuations are present. It is then reasonable to expect the entangled network, which controls actin monomer displacements, to have a broad distribution of physical and mechanical mesh sizes. This we propose is the origin.

We now introduce a simple physical quantification of this idea. (i) It is reasonable to model spatial distribution of filaments as a random fluid of thin rods, since actin concentrations are below the nematic phase transition. (ii) Given (i), the physical mesh (ξ) distribution was determined by Ogston to be: $P_\xi(\xi) = 4\pi\rho\xi \cdot \exp\left(-2\pi\rho\xi^2\right)$, where ρ is the contour length per volume [19]. This implies that the suspension can be thought of as tiling space with meshes (groups of nearby filaments) of variable local density and size randomly distributed. (iii) As in

semidilute solutions of entangled flexible chains in a good solvent, a direct connection between physical mesh and entanglement (or localization tube) length applies. Mean field ideas [11] and a binary collision approximation (BCA) [20] show that average tube radius and mesh size are related as: $R_e = a\xi^{\frac{6}{5}} l_p^{-\frac{1}{5}}$ where l_P is the persistence length of semiflexible polymer and a is a numerical constant. This concentration dependence of the tube radius has been recently revisited [21,22] but we show below that this simple relation is consistent with our experimental data. The BCA allows us to employ $R_e = a\xi^{\frac{6}{5}} l_p^{-\frac{1}{5}}$ locally, on a mesh-by-mesh basis, in order to relate local spatial variation of actin density to local spatial variation of the tube radius. How correlation effects should be included is unknown, and (as we show) apparently unnecessary to adequately describe our observations. Then the probability a given actin monomer has displacement $r_\perp$ is given by probability density averaged over spatial and temporal fluctuations, $P(r_\perp) = \int d(R_e) \cdot P_{R_e}(R_e) \cdot \frac{1}{\sqrt{\pi R_e^2}} \exp\left(-\frac{r_\perp^2}{R_e^2}\right)$, where for each specific tube radius the distribution of transverse fluctuation is Gaussian. The implied distribution of tube radii, $P_{R_e}(R_e)$, is plotted in Fig. 4.5a. But the tube radius cannot be arbitrarily small, since filaments have finite size, so a lower limit of integration is introduced. This physical argument generates a dimensionless formulation of the 1D transverse distance distribution,

$$P(\tilde{r}_\perp) = c\int_\alpha^\infty d(\tilde{R}_e) \cdot \tilde{R}_e^{-\frac{1}{3}} \exp\left(-\frac{\pi}{4}\tilde{R}_e^{\frac{5}{3}}\right) \cdot \exp\left(-\frac{\tilde{r}_\perp^2}{\tilde{R}_e^2}\right) \qquad (4.1)$$

where $\overline{R}_e \equiv a(8\rho)^{-\frac{3}{5}} l_p^{-\frac{1}{5}}$, $\tilde{R}_e \equiv R_e / \overline{R}_e$, $\tilde{r}_\perp \equiv r_\perp / \overline{R}_e$, α is the dimensionless lower cutoff of the integration, and *c* is a normalization factor depending on $\overline{R}_e$ and α.

For large $r_\perp$, using the method of steepest descent Eq (1) predicts a nearly exponential tail:

$P(r_\perp) \propto e^{-1.2\left(\frac{r_\perp}{\bar{R}e}\right)^{\frac{10}{11}}} \approx e^{-\frac{r_\perp}{\lambda}}$ where $\lambda \approx \frac{\bar{R}_e}{1.2}$. Physically, the tail is the ensemble-average consequence of an effectively static disorder of harmonic tube constraints which follow the local variation of mesh sizes. This agrees with data at different actin concentrations and suggests (Fig. 4.4a) that $\alpha = 1$. This parameter mainly determines the position of transition from Gaussian to exponential-like distribution. A value of unity implies the mean tube radius (Fig. 4.5a):

$$\langle R_e \rangle \approx 1.6\bar{R}_e \approx 1.6\rho^{-\frac{3}{5}} l_p^{-\frac{1}{5}} \tag{4.2}$$

where $\bar{R}_e$, effective filament thickness, is plotted logarithmically versus actin concentration in Fig. 4.5c, and follows a power law $\bar{R}_e \propto c^{-\frac{3}{5}}$, consistent with its definition. Note that the cutoff generates a monotonically decreasing tube radius distribution, consistent with the observation of positive skewness of RMS fluctuations in Fig. 4.3. To illustrate the connection between the distribution and the mean value, the distribution rescaled by mean tube radius is also plotted in Fig. 4.5b. Fast thermal fluctuation of single filaments accounts for concentration dependence of the effective filament thickness, which is defined by the largest possible amplitude of bending fluctuation considering the statistically averaged inter-filament interaction. Another plausible physical origin of the cutoff is strong suppression of small meshes due to their high local osmotic pressure and hence large free energy cost.

4.3 Conclusions

The present experiments cannot discriminate between spatial and temporal heterogeneity, which remains as an enticing challenge. Another open question concerns the length scale of heterogeneity. That the distribution of fluctuations from a single filament's time trace is narrower (Fig. 4.3) than the theoretically deduced tube radius distribution suggests it to be smaller than the

filament length. That is supported by the fact that data for a single actin filament, Fig. 4.4a, is consistent with the ensemble average. However, the data does not allow us to distinguish between this and other small scales, the entanglement length and persistence length. Although the microscopic nature of this heterogeneity is not fully understood, we hope these findings will call attention to the prominence of distributions instead of "averaged" numbers, even in classical models [23].

4.4 References

1. Read DJ, Jagannathan K, Likhtman AE (2003) Entangled polymers: constraint release, mean paths, and tube bending energy. *Macromolecules* 41: 6843-6853.
2. de Gennes PG (1971) Reptation of a polymer chain in presence of fixed obstacles. *J. Chem. Phys.* 55: 572-579.
3. Doi M, Edwards SF (1986) *The Theory of Polymer Dynamics* (Clarendon, Oxford).
4. Käs J, Strey H, Sackmann E (1994) Direct imaging of reptation for semiflexible actin filaments. *Nature* 368: 226-229.
5. Perkins TT, Smith DE, Chu S (1994) Direct observation of tube-like motion of a single polymer chain. *Science* 264: 819-822.
6. Everaers R, *et al.* (2004) Rheology and microscopic topology of entangled polymeric liquids. *Science* 303: 823-826.
7. Wischnewski A, Monkenbusch M, Willner L, Richter D, Kali G (2003) Direct observation of the transition from free constrained single-segment motion in entangled polymer melts. *Phys. Rev. Lett.* 90: 058302.
8. Morse DC (1998) Viscoelasticity of concentrated isotropic solutions of semiflexible polymers. 2. linear response. *Macromolecules* 31: 7044-7067.

9. Dichtl MA, Sackmann E (1999) Colloidal probe study of short time local and long time reptational motion of semiflexible macromolecules in entangled networks. *New J. Phys.* 1: 18.
10. Robertson RM, Smith DE (2007) Direct measurement of the intermolecular forces confining a single molecule in an entangled polymer solution. *Phys. Rev. Lett*. 99: 126001.
11. Isambert H, Maggs AC (1996) Dynamics and rheology of actin solutions. *Macromolecules* 29: 1036-1040.
12. Zhou Q, Larson RG (2006) Direct calculation of the tube potential confining entangled polymers. *Macromolecules* 39: 6737-6743.
13. Limozin L, Bärmann M, Sackmann E (2003) On the organization of self-assembled actin networks in giant vesicles. *Eur. Phys. J. E* 10: 319-330.
14. Murphy DB, Gray RO, Grasser WA, Pollard TD (1988) Direct demonstration of actin filament annealing in vitro. *J. Cell Biol.* 106: 1947-1954.
15. Anthony SM, Zhang LF, Granick S (2006) Methods to track single-molecule trajectories. *Langmuir* 22: 5266-5272.
16. Wang W, Pottmann H, Liu Y (2006) Fitting B-spline curves to point clouds by curvature-based squared distance minimization. *ACM Trans. Graph.* 25: 214-238.
17. Brangwynne CP, *et al.* (2007) Bending dynamics of fluctuating biopolymers probed by automated high-resolution filament tracking. *Biophys. J.* 93: 346-359.
18. Käs J, *et al.* (1996) F-actin, a model polymer for semiflexible chains in dilute, semidilute, and liquid crystalline solutions. *Biophys. J.* 70: 609-625.
19. Ogston AG (1958) The spaces in a uniform random suspension of fibres. *Trans. Faraday Soc.* 54: 1754-1757.
20. Morse DC (2001) Tube diameter in tightly entangled solutions of semiflexible polymers. *Phys. Rev. E* 63: 031502.

21. Tassieri M, et al. (2008) Dynamics of semiflexible polymer solutions in highly entangled regime. *Phys. Rev. Lett.* 101: 198301.

22. Hinsch H, Wilhelm J, Frey E (2007) Quantitative tube model for semiflexible polymer solutions. *Eur. Phys. J. E* 24: 35-46.

23. Glaser J, *et al.* (2010) Tube width fluctuations in F-actin Solutions. *Phys. Rev. Lett.* 105: 037801.

4.5 Figures

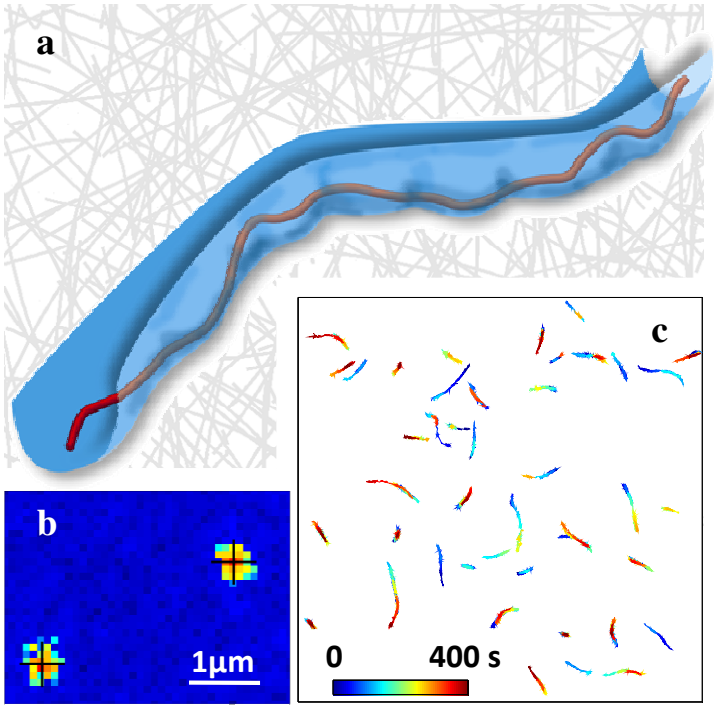

Figure 4.1

The main idea of this experiment. (a) Schematic representation of a chain constrained into a tube-like region by an effective harmonic potential, the collective topological effect of surrounding chains. Minima of this potential define the primitive path. As discussed in the text, the radius of the tube is irregular and polydisperse. (b) A representative image showing two labeled segments of a long actin filament. Analyzing the raw data using a two dimensional Gaussian spreading function allows one to determine the actual position of segments with sub-pixel resolution (~10 nm in this set of experiments), indicated by the crosses. (c) An overview of the variety of curvilinear-like diffusive motions of labeled actin segments in entangled F-actin networks. Colors denote time lapse of the trajectory. The F-actin concentration is 0.7 mg/mL. Temporal step is 0.5 s. The dimension of the view is 50µm×50µm.

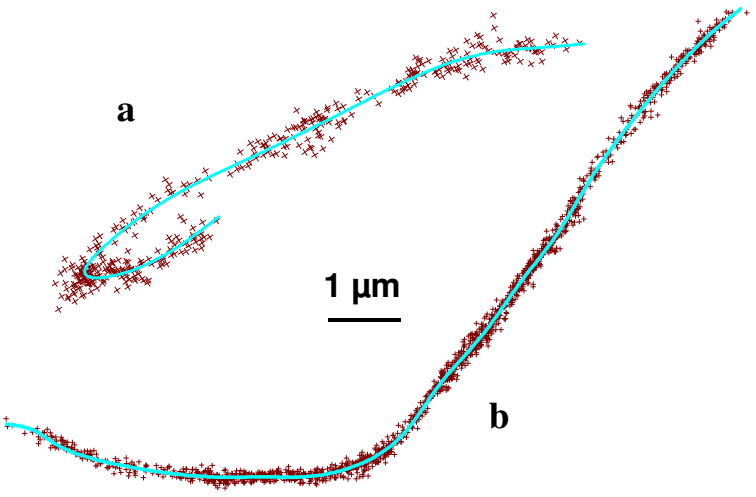

Figure 4.2

Representative trajectories of position clouds (crosses) obtained from segments along a chain at actin concentration 0.5 mg/mL (a) and 1 mg/mL (b). The primitive path (blue line) is generated by B-spline fitting of the point clouds.

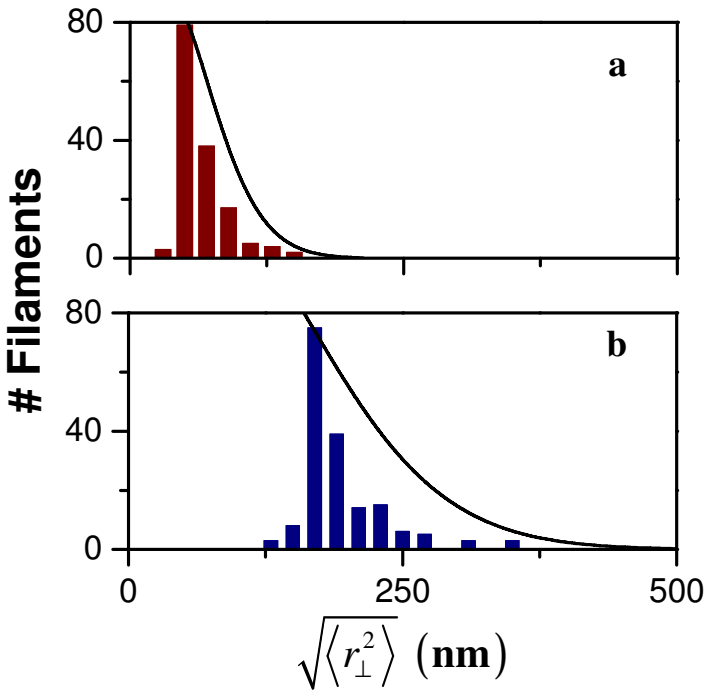

Figure 4.3

Histograms of RMS transverse fluctuations (distribution of "second moments") of single time traces along filaments at actin concentrations of 1 mg/mL (a) and 0.2 mg/mL (b). The solid lines compare to the expected distribution predicted by the ensemble-averaged model presented in the text, assuming that each filament feels a homogenous environment. The discrepancy between these two distributions demonstrates that the heterogeneity quantified here occurs on length scales smaller than the filament length.

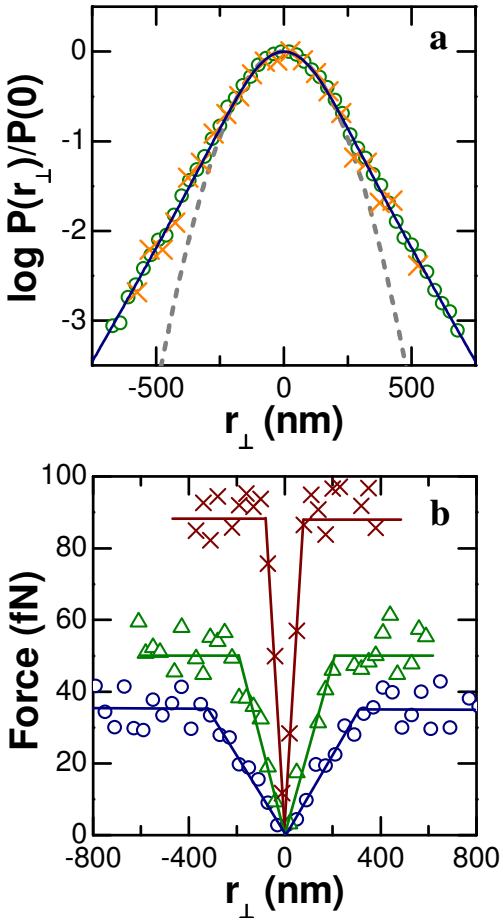

Figure 4.4

Illustrative transverse fluctuation distributions. (a) Transverse distance probability distributions, plotted against distance normal to the primitive path, for an ensemble of hundreds of filaments (circles) and for the trajectory of a single filament (crosses). Actin concentration is 0.5 mg/mL. The solid line is a fit using Eq. (4.1) with $\alpha = 1$. The dashed line is the corresponding Gaussian fit to the center part of the distribution. (b) Effective restoring forces, inferred from a Boltzmann distribution law as explained in the text, plotted against transverse distance. The actin concentrations are 1 mg/mL (crosses), 0.5 mg/mL (triangles), and 0.2 mg/mL (circles).

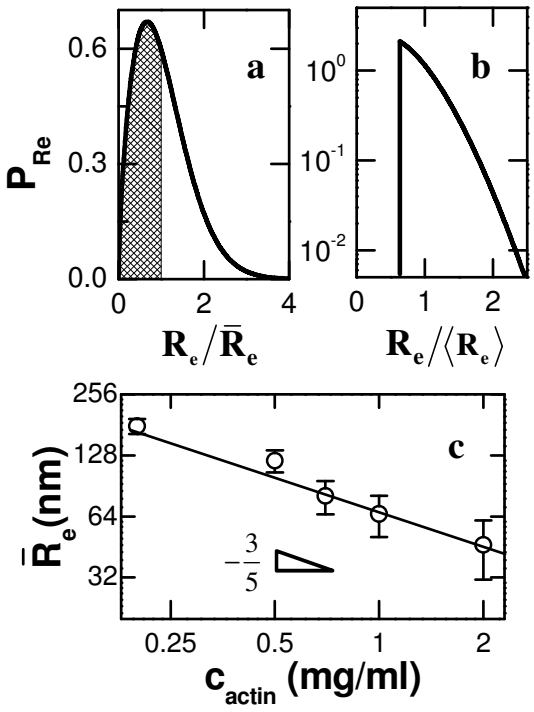

Figure 4.5

The tube radius distribution. (a) The distribution of tube radius, $\bar{R}_e P_{R_e}\left(\tilde{R}_e\right)=\frac{5\pi}{12}\tilde{R}_e^{\frac{2}{3}}\cdot\exp\left(-\frac{\pi}{4}\tilde{R}_e^{\frac{5}{3}}\right)$, is plotted against the dimensionless $\tilde{R}_e$ defined in the text, on linear scales. The shadowed region shows the needed lower cutoff determined by fitting the data. (b) The distribution of tube radius plotted on semilogarithmic scales rescaled by mean tube radius, taking lower cutoff into consideration so that the average tube radius $\langle R_e \rangle = 1.6\bar{R}_e$. (c) Logarithmic plot of $\bar{R}_e$ versus actin concentration. The error bars show the standard deviation from many experiments. The solid line has slope -3/5.

CHAPTER 5

SINGLE-MOLECULE IMAGING OF REPTATION VIA ROUSE DYNAMICS

The contents of this chapter are based on experiments done by Bo Wang, Juan Guan, James Kuo, Sung Chul Bae, and Steve Granick. Additionally, the methods part has been published as Juan Guan, Bo Wang, and Steve Granick (2011) Automated single molecule imaging to track DNA shape, Langmuir, 27, 6149-6154.

5.1 Background

A canon of polymer physics is that the dynamics of entangled polymer liquids transpires by reptation such that the average chain, confined in a virtual "tube" of topological constraints by surrounding chains, finds it easiest to diffuse preferentially along the chain contour. Intrachain fluctuation, probed in the experiments below, arises as a chain of coupled harmonic springs with the decomposed normal modes described by quasi-one-dimensional Rouse dynamics [1]. While vast literature confirms the existence of this virtual tube [2-6], single-molecule imaging presents the opportunity to test this model quantitatively in real space and time, an approach that differs from spin-echo spectroscopy [6]. Moreover, the use of entangled DNA presents an experimental system considerably more highly entangled than can be achieved in current computer simulations [3,7]. Here, we use single-molecule imaging to contrast the diffusion trajectories of the same DNA in two entangled networks: actin networks whose tube is transient, and agarose networks whose tube constraints are permanent, their mesh size being matched to be similar. The scaling laws predicted by theory are verified without ambiguity for what is considered to be the first time. We also investigate heterogeneity in the ensemble average, some of which appears to be

configurational entropy of the tube, some of which likely originates in the intrinsic local density fluctuations of entangled solutions.

5.2 Results and Discussions

To test quasi-one-dimensional Rouse scaling, we chose a polymer large enough to visualize with an optical microscope, under conditions such that the Rouse time of 0.1 – 1 s far exceeded the experimental resolution of 10 ms. Lambda phage DNA (λDNA, 48.5 kbp, contour length ~16 μm, radius of gyration R_g ~400 nm) was covalently labeled with TM-Rhodamine (Mirus Bio) at a density of 1 dye per 4 base pairs, covalent attachment eliminating the extension of contour length that results from using conventional intercalated dyes [3]. The DNA was entangled within matrices at ionic strengths (>100 mM) such that intramolecular electrostatic repulsion was largely screened with the persistence length of ~ 50 nm signifying that long DNA was a flexible polymer coil [3]. The matrices properties are well understood from other studies: F-actin networks (2 mg/mL) polymerized *in vitro* as described elsewhere [4], and agarose gel (1.5% w/w) which is standard in gel electrophoresis [8,9]. Both matrices have a mesh size (ξ) of ~200 nm, so λDNAs are well entangled with the surrounding chains for $\frac{N}{N_e} \sim \left(\frac{2R_g}{\xi}\right)^2 \sim 20$, with reptation time on the scale of 10 – 100 s. Here, N_e is the degree of polymerization between effective entanglements. It was critical to mix the DNA into its matrix before matrix polymerization, in order to guarantee homogenous entanglement and an equal sampling of all the microscopic configurations. Otherwise, insufficient mixing and extremely slow relaxation of DNAs in entanglements often resulted in highly heterogeneous populations and collapsed coil conformation of DNAs in solvent pockets.

The labeled DNAs were viewed on a homebuilt microscope using highly laminated illumination to improve the signal-to-noise ratio [10]. The focus was deep into the sample (~20

μm) to avoid potential wall effects. Fluorescence images were taken at frame rate of 80 Hz by a back-illuminated EMCCD camera. Movies typically lasting 5,000 frames were analyzed by a line tracking program written in house, tracking the apparent backbone stretching defined by the longest path of a minimum spanning tree constructed on the two-dimensional projected fluorescence image (Fig. 5.1a) [9]. Although the image of the backbone was of course optically limited, sub-diffraction resolution was achieved by fitting the cross-section intensity profile at each point along the backbone to a Gaussian spreading function [9], with the efficacy of doing so confirmed experimentally by tracking these same static DNA adsorbed on glass slides. The center of mass of each molecule in each frame was located with a precision of ~30 nm assuming fluorescence intensity proportional to the local mass. Also, the curvilinear center along the contour was defined as the middle point of the apparent backbone, with a precision of ~60 nm; the center was selected for analysis, not the ends, since ends are expected to escape from the tube quickly and have larger tracking error. Fig. 5.1b illustrates the trajectories of center of mass and curvilinear center for a typical molecule. Note that the trajectories suggest a hopping scenario corresponding to retraction events followed by stretching into a new tube as illustrated in Fig. 5.1c, which plots the apparent 2D projected backbone contour length versus time. This whole-chain contour length fluctuation has the long time scale of ~10 s, indicating a high activation energy as predicted in theories [11]. While this mode of relaxation is readily accessible via our methodology, it is infrequent, so the remainder of this chapter focuses on confined Rouse dynamics on time scales shorter than 10 s.

Fig. 5.2 shows ensemble averaged mean-square displacement, MSD. It contrasts the time dependence of the center of mass and the curvilinear center, in F-actin network and in agarose gel. Theoretically, as predicted by standard Rouse and reptation models, the MSD, $\left\langle \Delta r^2 \right\rangle$, of the center of mass scales as $\left\langle \Delta r_c^2(t) \right\rangle \propto t^{\frac{1}{2}}$, and the segmental diffusion scales as $\left\langle \Delta r_s^2(t) \right\rangle \propto t^{\frac{1}{4}}$ for

$t < \tau_R$, where τ_R is the Rouse time of the chain. At times longer than τ_R, all segments move coherently, so scaling changes to $\left\langle \Delta r_s^2(t) \right\rangle \propto t^{\frac{1}{2}}$ [1]. Remarkably, in both systems, we observe directly that the center of mass diffusion follows a scaling law $\left\langle \Delta r_c^2(t) \right\rangle \propto t^{\frac{1}{2}}$ at times below 1 s, which subsequently gradually converges to diffusive motion. Meanwhile, for the curvilinear center, the segmental MSD scales with time as $\left\langle \Delta r_s^2(t) \right\rangle \propto t^{\frac{1}{4}}$ at times below 0.4 s, after which the curves bend up. In the F-actin networks, a clear crossover to a second regime where $\left\langle \Delta r_s^2(t) \right\rangle \propto t^{\frac{1}{2}}$ is observed, defining from experiment the Rouse time of 0.6 s. This number agrees well with literature values when additional local friction from the matrices is considered [12-14]. On time scales longer than Rouse time, the center of mass and segmental MSDs gradually converge confirming the chains start to move coherently. However, the broad transition regimes between power law regimes, especially in agarose gel, indicate that heterogeneous dynamics is buried in the ensemble averaged behavior.

The single molecule motion of many individual DNA molecules is plotted in Fig. 5.3. Here ≈200 molecules have been studied in each network, each of them monitored over a mean trajectory of ~30 s, 50 times of the Rouse time. Notice that the variation between single molecule responses spans one order of magnitude at short times and even more on time scales longer than the Rouse time. Depending on the trajectory, MSDs of the curvilinear center can deviate from the ensemble-averaged power law relationship $\left\langle \Delta r_s^2(t) \right\rangle \propto t^{\frac{1}{4}}$ characteristic of confined Rouse motion as early as 0.1 s, which is the Rouse time of free λDNA in water [12]. This variation cannot be explained by the lack of statistics of single trajectories, since below 1 s each data point represents 50-1000 independent measurements.

We extract the scaling power of the single molecule MSDs versus time between 30 ms – 0.3 s (the time regime for which reliable fitting of power laws for single-molecule statistics could be acquired), and report the histograms, normalized by the peak values, in Fig. 5.4. For both systems, the histograms peak sharply at the ensemble average values, 1/2 for center of mass and 1/4 for curvilinear center, but with broader spreading for DNA in agarose gel which we attribute to transient entropic trapping of DNA within the broad mesh size distribution of agarose gels [15]. Noteworthy is that the histograms for center of mass motions are symmetric, for DNA in F-actin, it can be fit well empirically with a Gaussian distribution. To the contrast, the histograms for curvilinear centers exhibit significant asymmetricity.

To investigate whether the power laws decouple from the magnitude of displacements, we grouped the molecules into three populations using the scaling of segmental MSDs, with slope smaller than 0.15 as slow population, anything above 0.35 as fast population, anything in between as medium population. The MSDs of each group can be calculated for both curvilinear center and center of mass. No crossover was observed (Fig. 5.3), suggesting everything is coupled: the scaling and the magnitude of displacements; short time behaviour and long time behaviour since the data are grouped according to the scaling law below 0.3 s, the center of mass and the curvilinear center as the molecules are combined via curvilinear center motions. The separation of these distinct populations presents a logical paradox, since in classic reputation model, while the magnitude of displacements might reflects the fluctuations of the local friction, the scaling law should be conserved.

As a second quantification, we measured the histogram of Rouse time, defined as the times of individual molecules to travel the ensemble averaged Rouse distance, and the histogram of Rouse distance, defined as the mean squared distances traveled at ensemble averaged Rouse time (Fig. 5.5), in the focus that this quantities reflect the characteristic time and length scales on the single molecular level. Similar to our results on scaling power laws, while all data peak at the ensemble average, the distributions, especially for the time distributions, are remarkably broad.

To be able to understand the observed heterogeneity, one has to consider fluctuations on three levels. First, it is reasonable to expect the stochastic curvilinear intramolecular fluctuations of a Rouse chain in a predefined tube is averaged out with our trajectories more than 10 times longer than the Rouse time, and therefore unlikely to contribute to the spreading discussed here. Second, on times shorter than reptation time, the "configurational entropy" of the virtual tube, in other words, how the tube itself stretches in the lab frame of reference could introduce significant heterogeneity. While the degrees of freedom parallel and perpendicular to the tube decouple, they are coupled in lab frame [16]. Thus, the chain dynamics in real space is anticipated to depend on the topological configuration of the tube, an effect more prominent when N/N_e becomes smaller. Third, the observed broad distributions can be the response to the intrinsically heterogeneous local environments. Indeed, it is easy to show that over the experimental time window of 1 s, the typical molecule samples a spatial length <5 μm. The heterogeneity of actin networks on this length scale was noted previously [4,5]. To fully disentangle the fluctuations into separate physical contributions, reductive simulations are needed to add these elements one by one [17].

5.3 Conclusions

This study not only demonstrates pleasing agreement with ensemble-averaged theory applied widely to explain and predict the mechanical properties and diffusivity of entangled polymer materials over the past half century [1,7,8,18], but also the limits of its validity when applied to particular experimental situations. The prominent single molecule heterogeneity that we observe, enabled by recent technical advances [9,19], is not addressed by the classical mean-field theories whose predictions we here confirm. It is reasonable on physical grounds to anticipate that the subpopulation of fastest-moving chains may dominate transport and the slower subpopulation dominate mechanical relaxation, although the main point of this study is to present experimental data. We conclude by noting that the systems explored here have bearing on

understanding fundamental transport processes in biophysical applications including drug delivery and electrophoresis, where DNAs also navigate through the entangled cytoskeleton or cross-linked gels. In those important situations, so few molecules are present that distributions of single-molecule response may be expected to control relevant properties.

5.4 Materials and Methods

DNA labeling

Lambda-DNA (48.5 kbp, Promega) was labeled by covalently attaching dye, a Rhodamine B derivative (Mirus) to heteroatoms on DNA, at a labeling density of roughly 1 dye per 4 base pairs. For F-actin networks, labeled DNAs were added to G-actin (from skeletal muscle) solution in fresh G-buffer (5 mM Tris at pH 8.0, 0.2 mM $CaCl_2$, 1 mM ATP, 0.2 mM DTT and 0.01% NaN_3), and then the polymerization of F-actin was induced by addition of salt (100 mM KCl and 2mM $MgCl_2$). For agarose gel, DNAs were stirred in agarose solution in 0.5x TBE buffer (45 mM Tris, 45 mM borate, 1mM EDTA) at 55 °C, and then cross-linking was allowed to proceed as the mixture was slowly cooled down to room temperature. Ascorbic acid (5-10 mM) was supplemented in the buffer to counter photo-bleaching and photo-chemically induced severing of the molecules.

DNA tracking

To quantify, within the limits of optical resolution, the linear shapes of DNA images that are noisy, faint, and diffraction-blurred, we take the approach that it is better to reject data from consideration than to improperly include it in subsequent analysis. This method consist of three elementary stages: first, to discriminate the shapes of macromolecules from noise, which we refer to as “feature finding”; second, to approximate those shapes as lines, which we refer to as

"line tracking"; third, to discriminate reasonable from unreasonable fitted conformations in the time domain, which we refer to as "temporal consistency check".

While the details are described in ref. [9], the basic architecture of the algorithm is:

1. Filter digitized images to remove shot noise by performing a two-dimensional Gaussian smoothening.

2. Calculate the mean and variance of the intensity of pixels in each image and keep high intensity pixels as candidate molecules.

3. Group pixels/points into separate molecules using a specified threshold distance.

4. Identify a longest path through each group of points using an intensity-weighted minimum spanning tree.

5. Local quadratic fits to adjust the positions of the pixels.

6. Additional position refinement by Gaussian fit to find the center using the cross-section intensity profile at each position.

7. Find a new longest path from these points by generating a new minimum spanning tree from these points.

8. Smoothen the line with a discrete wavelet filter.

9. Perform pre-screening to reject unreasonable lines such as those which drastically fluctuate in length, are looped, or are from molecules that are out of focus.

10. Validate line with previous and subsequent lines in time.

The method is intrinsically coarse-grained, incapable of discriminating internal conformations smaller than the optical resolution, hence yields lines (Fig. 5.6) designed to describe the contour of the macromolecule without attention to any structure smaller than the optical resolution.

5.5 References

1. Doi M, Edwards SF (1986) *The Theory of Polymer Dynamics* (Clarendon, Oxford).
2. Käs J, Strey H, Sackmann E (1994) Direct imaging of reptation for semiflexible actin filaments. *Nature* 368: 226-229.
3. Perkins TT, Smith DE, Chu S (1994) Direct observation of tube-like motion of a single polymer chain. *Science* 264: 819-822.
4. Wang B, Guan J, Anthony SM, Bae SC, Schweizer KS, Granick S (2010) Confining potential when a biopolymer filament reptates. *Phys. Rev. Lett.* 104: 118301.
5. Glaser J, *et al.* (2010) Tube width fluctuations in F-actin Solutions. *Phys. Rev. Lett.* 105: 037801.
6. Wischnewski A, Monkenbusch M, Willner L, Richter D, Kali G (2003) Direct observation of the transition from free constrained single-segment motion in entangled polymer melts. *Phys. Rev. Lett.* 90: 058302.
7. Everaers R, *et al.* (2004) Rheology and microscopic topology of entangled polymeric liquids. *Science* 303: 823-826.
8. Fakhri N, MacKintosh FC, Lounis B, Cognet L, Pasquali M (2010) Brownian motion of stiff filaments in a crowded environment. *Science* 330: 1804-1807.
9. Guan J, Wang B, Granick S (2011) Automated single-molecule imaging to track DNA shape. *Langmuir* 27: 6149-6154.
10. Tokunaga M, Imamoto N, Sakata-Sogawa K (2008) Highly inclined thin illumination enables clear single-molecule imaging in cells. *Nat. Methods* 5: 159-161.
11. Milner ST, McLeish TCB (1998) Reptation and contour-length fluctuations in melts of linear polymers. *Phys. Rev. Lett.* 81: 725-728.
12. Teixeira RE, Dambal AK, Richter DH, Shaqfeh ESG, Chu S (2007) The individual dynamics of entangled DNA in solution. *Macromolecules* 40: 2461-2476.

13. Hsieh C-C, Balducci A, Doyle PS (2007) An experiment study of DNA rotational relaxation time in nanoslits. *Macromolecules* 40: 5196-5205.
14. Robertson RM, Smith DE (2007) Direct measurement of the intermolecular forces confining a single molecule in an entangled polymer solution. *Phys. Rev. Lett*. 99: 126001.
15. Valentine MT, *et al.* (2001) Investigating the microenvironments of inhomogeneous soft materials with multiple particle tracking. *Phys. Rev. E* 64: 061506.
16. The simulation to understand the data is in progress in collaboration with Zuowei Wang and Ronald G. Larson.
17. Han Y, *et al.* (2006) Brownian motion of an ellipsoid. *Science* 314: 626-630.
18. Hou JX, Svaneborg C, Everaers R, Grest GS (2010) Stress relaxation in entangled polymer melts. *Phys. Rev. Lett.* 105: 068301.
19. Granick S, *et al.* (2010) Single-molecule methods in polymer science. *J. Polym. Sci. Pt. B-Polym. Phys.* 48: 2542-2543.

5.6 Figures

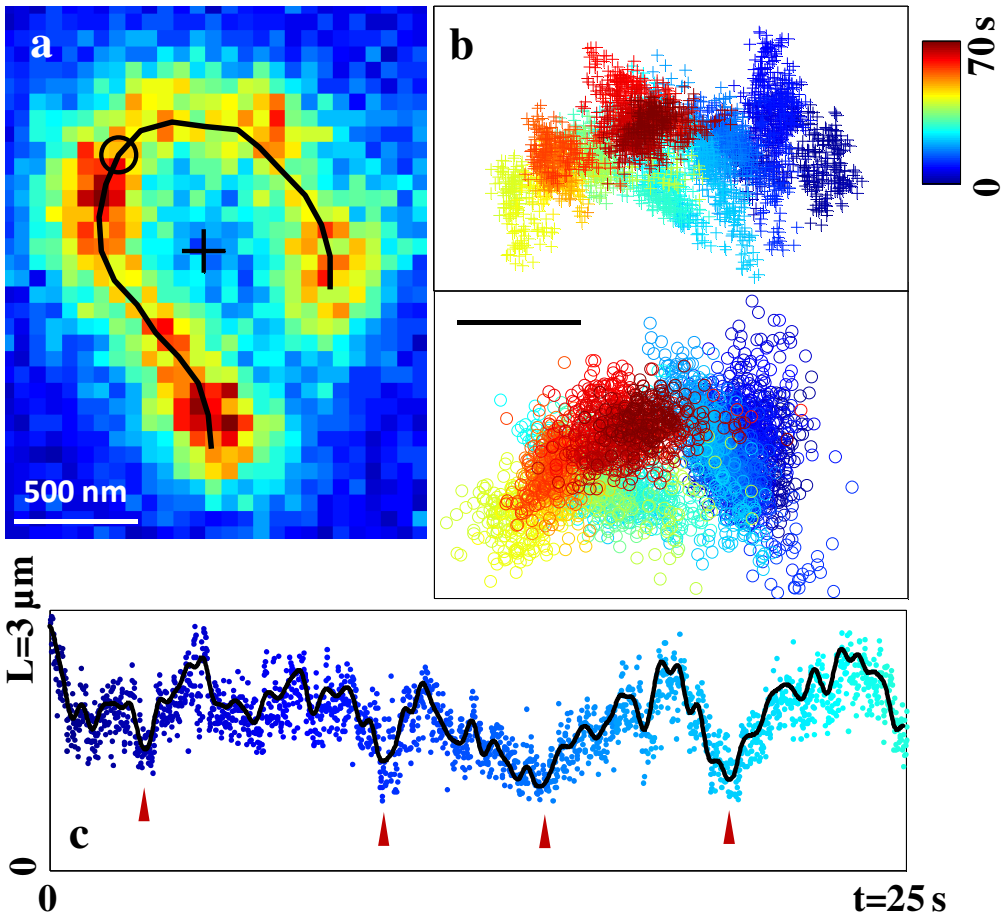

Figure 5.1

(a) A fluorescence image of a λDNA molecule in an F-actin network at one instant of time, with its center of mass (cross), apparent backbone (solid line), and curvilinear center (circle) highlighted. (b) Trajectories of center of mass (upper panel) and curvilinear center (lower panel) of this molecule are illustrated. Color, from blue to red, represents time from 0 to 70 s. The scale bars are 500 nm. (c) The apparent 2D projected backbone contour length, *L*, is plotted against time for the first 25 s of the same trajectory as in (b). Hopping events, at which *L* also exhibits local minima, are indicated by the arrows.

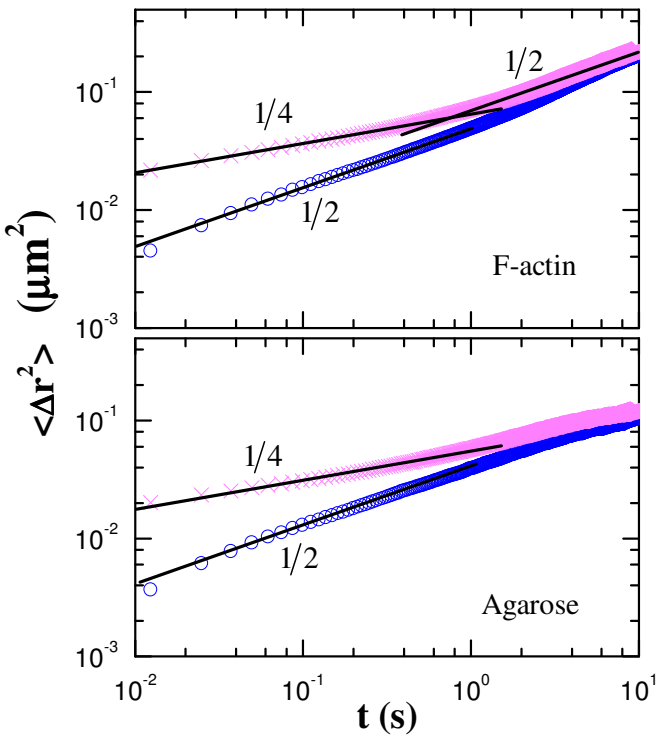

Figure 5.2

Ensemble-averaged MSDs of center of mass (circles) and of curvilinear center (crosses) are plotted against logarithmic time for DNA in entangled F-actin networks (upper panel) and in agarose gel (lower panel). Slopes of the solid lines are indicated in the figure.

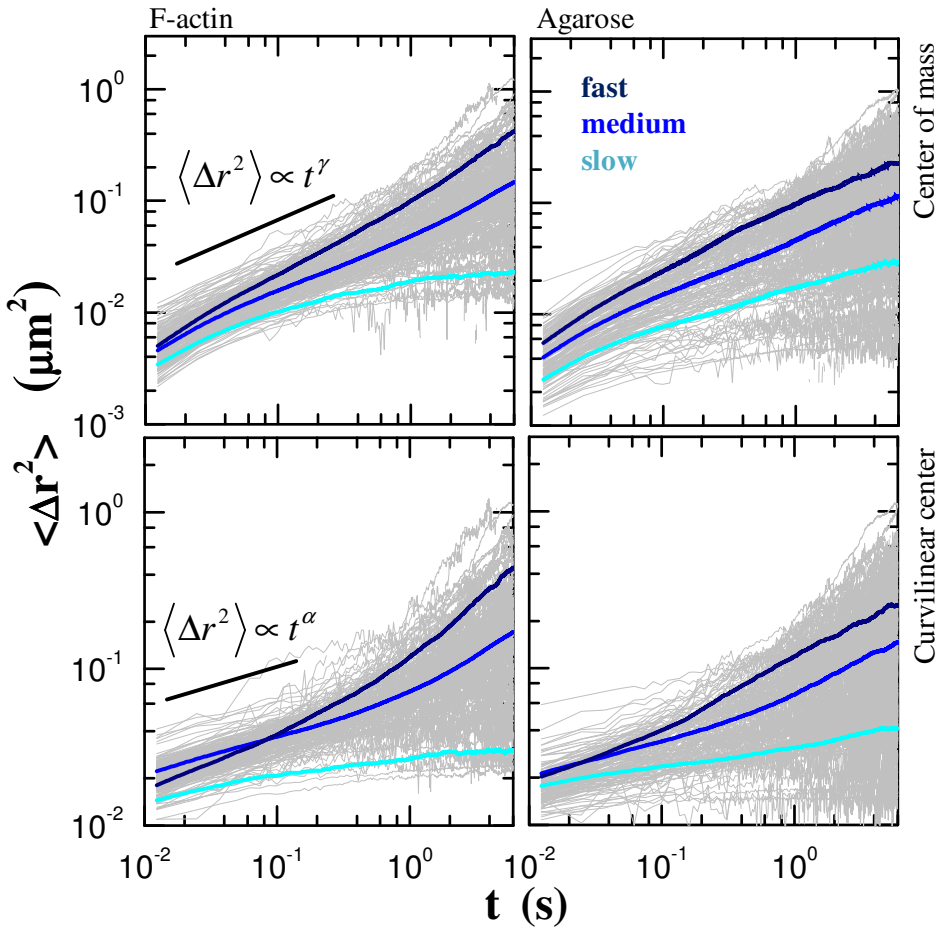

Figure 5.3

Single molecule MSDs of center of mass (upper panels) and of curvilinear center (lower panels) are plotted against time on log-log scales for DNA in entangled F-actin (left panels) and agarose gel (right panels). The averages for fast, medium and slow populations are highlighted as colored lines. The populations are separated according to the scaling power of single molecule MSDs of curvilinear center, $\alpha < 0.15$ as slow (cyan), $\alpha > 0.35$ as fast (navy), anything in between as medium (blue) populations.

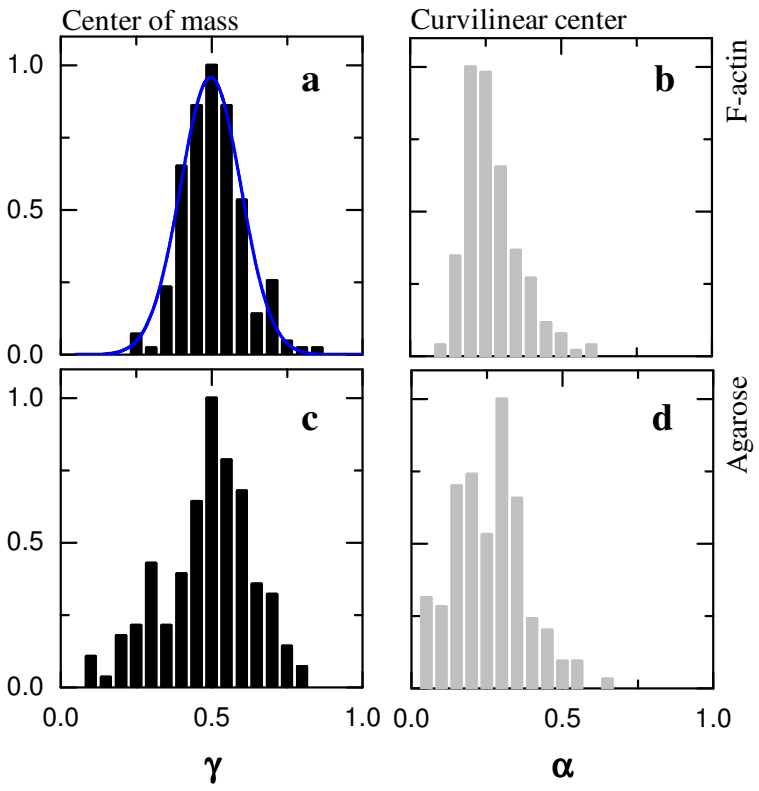

Figure 5.4

Histograms of the scaling power of single-molecule MSD versus time, for center of mass (γ, left panels, black bars) and for curvilinear center (α, right panels, grey bars). The power is extracted over the time window of 30 ms – 0.3 s for DNAs in entangled F-actin network (upper panels) and agarose gel (lower panels), where straight power law relationships are found. The histograms are normalized according to their peaks. The solid line in (a) is a Gaussian fit.

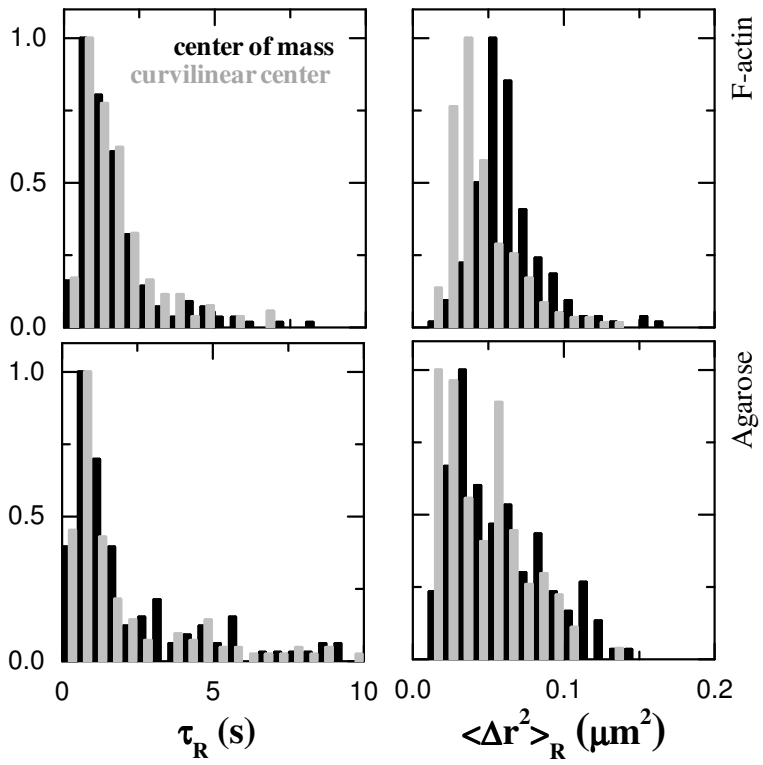

Figure 5.5

Histograms of Rouse time (τ_R , defined as the time of individual molecules to travel the ensemble averaged Rouse distance 0.03 μm^2 for center of mass and 0.05 μm^2 for curvilinear center, left panels) and Rouse distance ($\left\langle \Delta r^2 \right\rangle_R$, defined as the mean squared distance traveled at ensemble averaged Rouse time 0.6 s, right panels). The black bars are data for center of mass, the grey bars are for curvilinear center. The top plots are for entangled F-actin, the bottom plots for agarose. The histograms are normalized according to their peaks.

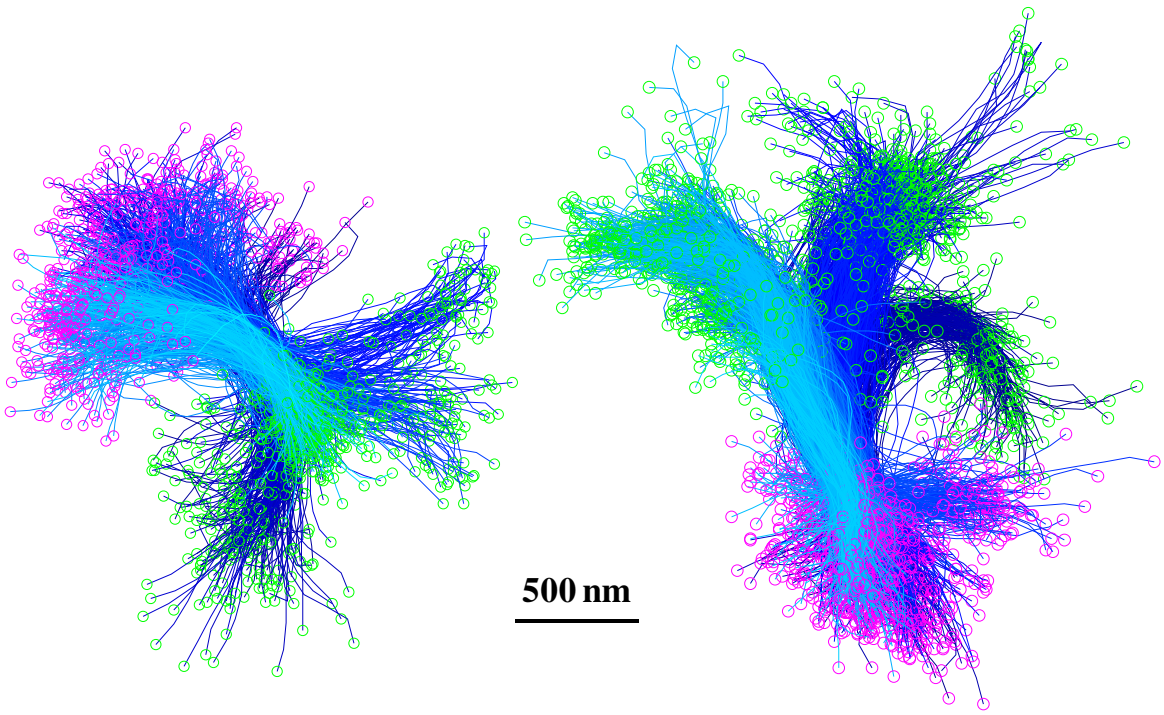

Figure 5.6

Representative curvilinear backbone overlay of two DNA molecules in F-actin network. Two ends are highlighted by green and pink circles respectively. The backbones are overlaid for 20 s, with color encoding the time from navy to cyan.

CHAPTER 6

BIPHASIC ACTIVE CARGO TRANSPORT IN LIVING CELLS

The contents of this chapter are based on a manuscript in preparation by Bo Wang, Kejia Chen, Sung Chul Bae, and Steve Granick.

6.1 Background

It is generally assumed that active cargo transport in living cells proceeds in a highly directed manner. In the popular scenario of "bidirectional motion", cargo is dragged along microtubules towards either the cell periphery or the perinuclear space, accomplished by motor proteins that link cargo to microtubules and walk along microtubules in predetermined directions. During the last quarter century, this process has become widely accepted as textbook knowledge [1-3], and it is believed to be an important factor in processes such as signal transduction and metabolism, which depend on active transport. However, the concept of bidirectional motion is based on measurements performed largely in model systems, where rectilinear directionality is reasonable to expect, such as vesicular transport in axons and cilia [4-7], as well as numerous *in vitro* studies [2,8,9]. This assumption is not self-evident in general. For endosomes, which are the focus of this study, it is anticipated that the directionality in a living cell must diversify according to whether their fate will be degradation, recycling, or retrograde transport to Golgi or endoplasmic reticulum [10-12], so the natural question arises, how cellular machinery selects direction, especially when microtubules form entangled networks whose strands are known to run in multiple directions and to cross paths (Fig. 6.1a) [13-15].

Taking stock of a vast literature, we note that although endosome dynamics has been studied on genomic scales [10] and single-molecule techniques have revealed the biochemical steps of individual molecular motors alone and when they tug in different directions [2,8,9,15], the link remains elusive to transport over long distances, which in practice may be on the scale of entire cells. The mechanisms of active transport have been modeled theoretically, mainly in the framework of bidirectional motion [16], but the results are inconclusive as to alternative possibilities. Full understanding will require quantitative analysis of the transit of cargos in real time through their pathways in living cells. Here, studying the trajectories of individual endosomes by fluorescence imaging and single particle tracking [17], we address this unmet need.

6.2 Results and Discussions

Two technical advances made this study possible (Fig. 6.2). Most importantly, we developed a new, robust method to discriminate active transport from passive Brownian diffusion. The resulting automated data analysis allows millions of data points to be analyzed (Table 6.1). This method, based on wavelet transforms, circumvents the model-dependence of earlier approaches (see Methods). We validated it vigorously with control experiments and simulated trajectories. A second enabling advance was experimental. In these experiments, we implemented methods of highly inclined illumination optical (HILO) geometry with the laser beam inclined and laminated as a thin optical sheet with thickness of ~1 μm into the cells [18]. This allowed us to avoid possible artifacts of 2D projection while at the same time locating the centers of endosomes with uncertainty <5 nm.

Fig. 6.1b shows two representative trajectories to illustrate the main conclusion of this study, the splitting of active transport into transport (T) and search (S) phases. Passive Brownian diffusion was negligible (grey dots) and active transport dominated (open circles and lines). In addition to periods of several consecutive runs ("run" refers to a non-stop active term without

directional reversal) which are persistent in direction (T phase), we also identify frequent time periods during which active transport consists of sharp changes in the directions of multiple short runs (S phase). In thousands of other trajectories, a clustering algorithm confirms this biphasic pattern (Methods, Table 6.1). Earlier criteria of active transport might mistakenly assign many S periods as passive diffusion, as they do not traverse long spaces and are not persistent over long distances, as active transport has in the past been presumed to be. Sometimes they even make closed loops (asterisk in Fig. 6.1c). Putting this phenomenological observation into context, it is worth noting that while microtubules are so stiff as to be straight on the scale of millimeters, they point in multiple directions and cross paths intermittently, at spacing known as the mesh size of their network. In spite of limited information from previous studies about the mesh size, cryo-electron microscopy of epithelial cells reveals the mesh size to be <1 μm [13,14], which is suggestively close to the directional persistence of the trajectories that we observe. Of probable biological relevance is that this intermittent switching between S and T phases makes good mathematical sense as a random searching process, using relocation to reduce oversampling, thus improving the searching efficiency [19,20]. Similar patterns have been observed in gene expression [21] and foraging [22], although searching was carried out by facilitated diffusion or animal action in those cases but by active transport in the present study. This mechanism allows endosomes to search randomly without predetermined directionality but quite "intelligently" until they reach the right spots for their biological missions.

Tests show this pattern to appear ubiquitous. We compared across three mammalian cell lines, as summarized in Fig. 6.3, confirming this biphasic pattern. The cell lines are HeLa, Marc145 (a monkey kidney epithelium cell line) and DU145 (a human prostate cancer cell line derived from brain metastasis). In each of these cell line, three distinct endosome populations were studied, each of them known to be transported through different sets of scaffold and motor proteins and have different ranges of cargo sizes: epidermal growth factor (EGF), low density lipoprotein (LDL) containing endosomes, and late endosomes tagged by lysosomal-associated

membrane protein 1 (LAMP1) [12]. Noteworthy is that late endosomes, tagged by LAMP1, spend more time in the T phase than do any of the other cases, although this actually accounts for a lesser fraction of the total active transport (Fig. 6.7). Various intriguing second-order influences were observed. When the cells were perturbed by Y27362 selectively inhibiting Rho-associated protein kinase p160ROCK [23], the time fraction changed. Microtubule-associated protein 4 (MAP4) decreased the fraction of T phase; the physical interpretation is that it acted as a road blocker on microtubules [24]. Trichostatin A (TSA), which induces microtubule acetylation that enhances the processivity of the motor proteins [25], had the anticipated opposite effect. A major conclusion is that while the time fraction of T phase varied between 30% and 80% depending on the experimental conditions, the displacement fraction was robust to these changes, always ≈75%.

These biphasic random walks, their persistence tightly regulated as we explain below, lack the directionality of the traditional bidirectional transport scenario [2-9]. Going beyond this, we compared the squared end-to-end displacement, R^2, of each individual period, to the total curvilinear distance traveled along the track within that period, s, which presumably correlates with time assuming the cargos move with certain speeds. Fig. 6.4 reveals two distinct families of behavior with astounding statistical regularity, an analysis which is possible because the large standard deviation can be averaged out by the millions of data points accumulated in this study. Truly random walks scale as $\langle R^2 \rangle \approx bs$, where b is the equivalent step length over which transport would be perfectly straight, on average. This we observed for the S phase; without any normalization of the data it all collapses onto the same line, described quantitatively by $b \approx 260\, nm$. This contrasts strongly with the T phase, whose power-law slope of 2 at short distances, indicating nearly linear directed motion, then decreases smoothly. The T phase data agree quantitatively with the Kratky-Porod model, known in the field of polymer physics to characterize semiflexible trajectories [26], which allows us to extract a length scale $2l_p \approx 6\, \mu m$

over which the motion is directionally persistent. Noting that this persistence length is several orders of magnitude smaller than that of microtubules suggests that in the T phase cargo also hops and switches between microtubules [15], but with frequency much lower than for the S phase.

The fact that all these data collapse without normalization, when compared across three cell lines and numerous control variables, signifies that the characteristic lengths of S phase (260 nm) and T phases ($2l_p \approx 6\mu m$) or in other words the switching probability between microtubules, are conserved across all of these changes. Similar statistical regularity emerges when one compares the mean speed and run time (Fig. 6.5). Mean speeds in the S phase scale as ¾ of speeds in the T phase, and mean run times scale as ½. To observe simple fractional relations is a great surprise.

These observations lead us to an alternative scenario of active transport which differs from bidirectional motion – cargos travel on a disordered microtubule network [19] with their directional processivity differentially controlled in two phases. It is at first tempting to inquire if the biphasic dynamics is simply engraved by the local density of microtubules, but our finding that decorating the microtubules with MAP4 alters this behavior does not support such a picture. Alternatively, it could reflect the binding and activation of the motor proteins, more motors being engaged during T phase than S phase. Indeed, pioneering *in vitro* experiments suggest that changes in the number of active motors could induce different responses of cargo transport at the intersection of microtubules [15]. This mechanism is also qualitatively consistent with the simple fractional relations of speed and run time between two phases that we observe (Fig. 6.5). This line of logic further implies that the numbers of active motors on the cargos have to be tightly regulated, not stochastic as previously assumed [5,6,16], since the displacement fractions of the two phases presents surprising invariance (Fig. 6.3). It may be instructive to revisit the present set of regulatory components known to play critical roles in endocytosis (10), to see which phase they affect and how they regulate this search of biological targets.

6.3 Active Transport Detection

Detection

To study active processes uncontaminated by passive fluctuations, strict discrimination of the two is critical. Since faultless separation is impossible without full knowledge of the molecular mechanism, in practice one only can do so with a certain level of statistical confidence, depending on the method used. The existing methods fall into two categories. One approach is to detect extended, linear motion with long-range directionality [27-29], but while this is intuitively appealing, it carries strong assumptions about the nature of active transport and thus all ensuing analysis is predicated on this subset of trajectories. A second approach used in current literature is discrimination based on ensemble-averaged statistical quantities within sliding time windows, such as the mean squared displacement (MSD) or autocorrelation functions [30-32]. In practice, to gain needed statistical significance, it is necessary to average these quantities over a time window corresponding to at least a few hundred of data points. Efforts to push this approach to narrower time windows and fewer data points involve thresholding that must be carefully and manually balanced because inevitably it must be arbitrary [30-32]. A proper threshold can be difficult to select rationally owing to the intrinsic temporal and spatial heterogeneities of both active and passive motion. The new methods described below are believed to present an improvement. We validate them on the one hand by logical argument, but also on the other hand by testing them against simulated data, data selected to emulate the known experimental conditions.

Our scheme to detect active transport based on wavelet transforms is summarized in Fig. 6.2. The basic logic is to consider statistical drifts of position. Passive diffusion produces no drift in the average position but active motion causes it to change. This drift can be detected by using the continuous time wavelet transform (CWT), which calculates the *local* integral of time series

over various scales with weighting defined by the wavelet function used [33]. In this study we adopted the Haar wavelet, since it offers simplicity for the present purpose. As the first step, a 1D trajectory was transformed into time series of CWT coefficients over various scales (Fig. 6.6). Then a scale was chosen; the smaller the scale, the more contaminated by random passive motions are the coefficients but the greater the time resolution. In this study, we used coefficients over the scale $\tau = 32$, while noting that the time resolution of this detection is related but not limited to this scale. As pointed out in the validation described below, the method allows us to detect active transport as short as five consecutive frames. The threshold to distinguish active and passive components of the trajectory (Fig. 6.2c) was calculated based on the so-called universal threshold well-known in the wavelet analysis literature [33], $\delta = \tilde{\sigma}\sqrt{2\ln N}$, where N is the number of data points in this trajectory excluding first and last 16 data points, and $\tilde{\sigma}$ is the estimate of the standard deviation characterizing the contribution from passive motion. Here, $\tilde{\sigma}$ is first estimated on the scale $\tau = 2$ using the median absolute deviation (MAD) $\sigma \equiv \dfrac{median\{\left|c^{x,y}_{i=1,\ldots,N}(2)\right|\}}{0.6745}$, since on this scale the signal is dominated by noise (passive motion), and then amplified by $\tilde{\sigma} \equiv \sigma\sqrt{\tau}$ assuming the passive motion to evolve with time according to Fickian diffusion. Notably, while the detection of active steps is local, the estimate of passive fluctuations is global. This gives thresholding that adapts automatically to each separate trajectory, with thresholds reflecting the heterogeneity of the intracellular dynamics. Indeed, as illustrated in Fig. 6.7, the threshold in the present study can vary by two orders of magnitude, depending on the trajectory.

The tentative assignment of active transport proceeds by combining the time periods whose coefficients exceed this threshold on either the *x* or *y* dimension of space. It is then refined using an iteration step to fine-tune the threshold. For each individual trajectory (Fig. 6.1b), the MSD of the assigned passive portion were calculated and fitted with a power law versus time

with exponent α, $\left\langle \Delta r^2 \right\rangle \propto t^{\alpha}$, where $\alpha < 1$ is expected for passive motion [30]. If the fitted α exceeded 1.1, the threshold for that trajectory was decreased and the process repeated iteratively until the criterion $\alpha \leq 1.1$ was satisfied. However, we found this iteration step necessary for only <10% of all trajectories. They are the trajectories for which to estimate the noise level corresponding to passive motion using MAD (Fig. 6.7) was unreliable, as active transport comprised a prohibitively large fraction of the overall trajectory.

Dimension reduction

While the active transport studied here is expected to be linear along microtubules, the original tracking is done in x-y space. Naturally, transverse fluctuations of microtubules and the swinging motions of organelles might introduce significant fluctuations perpendicular to the microtubule. This issue cannot be resolved by simple polynomial fitting of the track, since the trajectories often exhibit high local curvature which we attribute to hopping between microtubules. To deal with this complication, wavelet transforms were useful to smoothen the raw trajectories of active transport. Briefly, Daubechies-16 discrete wavelet transform (DWT) coefficients over level 2 corresponding to neighboring 3-4 data points were calculated and a universal threshold δ was specified accordingly. A soft-thresholding function was then applied in which DWT coefficients exceeding δ in magnitude were pushed toward zero by δ, while those less than or equal to δ were set to zero [33]. The smoothened trajectory was obtained by inverse transforming the coefficients after thresholding (Fig. 6.2a). The smoothening was always performed over level 2, on which signal is expected on physical grounds to be dominated by noise. This avoids introducing possible long time correlation artifacts.

We find that displacement perpendicular to the imputed track has distributions fit well by Gaussian functions with variance of 20 nm. This is a pleasing number, because it coincides with

the sum of microtubule radius and the length of motor protein stalk, both of which are known independently. Microtubule fluctuation of this kind is therefore a minimal, second-order effect.

Validation

Because active portions of trajectories comprise normally just 10-20% of all steps, even 1% false detection might amount to 10% incorrect steps in the datasets of active transport. Our validation of the method began by disrupting the microtubules using nocodazole, and then the trajectories were analyzed for active transport as outlined in Fig. 6.2b. This confirmed that fewer than 0.1% of total steps were mistakenly assigned as active motion. However, this sets just a lower bound of false detection, as transitions between passive and active motion is expected to introduce further error.

Further testing the reliability of this method, we analyzed simulated trajectories. The following properties were fed into simulations: 1) the active transport had an exponential distribution of step size, the average being the experimentally-measured value, ~40 nm/step (50 ms); 2) the direction between adjacent active steps was allowed to vary by an angle selected at random from a uniform distribution bounded by $\pi/50$ to mimic the upper limit of the curvature observed in experimental trajectories (~ 1 μm); 3) fluctuations perpendicular to linear active transport were introduced as a Gaussian noise with width equal to the experimentally-measured value of 40 nm; 4) passive motion was simulated so as to generate sub-diffusive MSD curves similar to those we observed in cells whose microtubules had been disrupted by nocodazole; this was accomplished by positioning the steps randomly within an area defined by a 2D Gaussian spreading function centered at the average position of the previous 50 passive steps with width of 100 nm; 5) the transition between passive and active motion was assumed to be Poissonian with transition probabilities set to reproduce the observed average length of active runs, which was 20 steps (~1 s), the total active portion being ~20%. We emphasize the critical point that active steps were not assumed to be longer than passive ones.

Subjecting these simulated trajectories to the wavelet analysis described above, we found robustly that false-positive identification of active steps amounted to less than 1% of the total active steps. These mistaken identifications, mostly amounting to false runs typically of two or so frames, can be excluded easily if needed.

Though the abundance of false positives was <1% as noted, about 30-40% of the active steps were missed by the wavelet analysis, which can be expected since the universal threshold is known as a strict one [33]. In real data, the detection misses are expected to be fewer than this, since one of the purposes of the simulation was to identify the conditions under which the method breaks down. Most of the missed steps belonged to runs shorter than 5 steps; this is reasonable since their active time was too short to consistently shift the average position. Also often missed were the two ends of active runs, especially for the short runs; again, without significant distortion of the statistics. We noticed that long runs, which we knew to be true long runs because the data was simulated, were sometimes broken by the wavelet analysis into several shorter runs at locations where several consecutive steps were by chance small. In principle this could be improved by decreasing the threshold and/or extending the ends of the detected runs, but was not attempted in the present study since accuracy was most critical. This could also be improved by using other more complicated thresholds, because methods to do so are known [33], but was not attempted in the present study either, as we sought to keep the method simple and straightforward. In fact, the neglect of so many active steps is not considered serious. It is a necessary corollary of being stringent in excluding false positives.

Knowing the true averages for this simulated data, we confirmed that the active steps missed by wavelet analysis did not bias the average. Indeed, on the experimental side, the mean run time and speed measured with this method agree with literature [5,34-36], but we are equipped to analyze voluminous data.

Regarding validating the methods described above to account for fluctuations normal to the trajectory, we found that they performed well: they reproduced the known track with an average error at individual points of ~5 nm.

The performance reported here exceeds that of other methods which we are aware of. Looking to its possible applications, we emphasize that the method is general, and is expected to be useful in analyzing other dynamic systems in which active motion driven by force is mixed with passive fluctuation. The algorithm does not assume that active motion proceeds along a track; we assumed so here because it is known to be so for physical reasons. However, when considering other systems, the analysis threshold should be adjusted to the nature of the dynamics; for example, we found it useful to increase the universal threshold by a factor of 2 when passive motion was considered to be a diffusive random walk rather than the subdiffusive motion characteristic of the specific system described above. In any case, since thresholding scales with the universal thresholds described above, this argument adapts easily and automatically to whatever the local dynamic heterogeneity is, regardless of whether its passive components are Fickian or subdiffusive.

6.4 Materials and Methods

Materials and cells

HeLa cells (ATCC) and Marc-145 cells [37] were grown in Dulbecco's modified Eagle medium (DMEM), and DU145 cells (ATCC) were maintained in minimum essential medium (MEM). Both media were supplemented with 10% fetal bovine serum (FBS) and penicillin-streptomycin (100 U/mL and 50 µg/mL). To fluorescently label specific populations of endosomes, either 0.15 µg/mL biotinylated EGF complexed to Alexa-555 streptavidin or 10 µg/mL DiI conjugated LDL (Invitrogen) was applied to cells for 20 min and removed by washing with PBS. To label late endosomes, cells were transiently transfected with LAMP1 fused to

tagRFP (Invitrogen). To confirm that the active transport was along microtubules, 5 μg/mL nocodazole was supplemented in the medium and no active transport was observed afterwards. To increase the level of microtubule acetylation, 5 μM trichostatin A (TSA) inhibiting HDAC6 activity was added 60 min before imaging [38]. For experiments on cytoskeleton reorganization, 50 μM Y-27632 was applied to cells 30 min before imaging. All drugs were obtained from Sigma-Aldrich. Overexpression of microtubule-associated protein 4 (MAP4) was achieved by transient transfection of MAP4 fused to Emerald GFP (Invitrogen). Cells with bright green fluorescence, indicating MAP4 expression at high level, were chosen for imaging.

The labeling approaches were carefully selected and optimized to satisfy two stringent criteria. First, we required specific labeling of organelles whose fate within the cell is known. Second, the labeling must be highly specific and present bright and stable fluorescent spots with average organelle separation larger than 3 μm, so as to allow position information to be extracted below the optical diffraction limit, < 5 nm using the methods described below.

Imaging and tracking

For imaging, cells were plated onto growth dishes with collagen-coated glass coverslip bottoms (MatTek) and allowed to adhere and spread overnight. Live cells were imaged in phenol-red free OPTI-MEM medium (Invitrogen) supplemented with 4% fetal bovine serum (FBS), a medium empirically found to reduce the background and prolong photostability of fluorescent molecules. The imaging was carried out on a homebuilt microscope with objective-based total internal reflection geometry, using an α-Plan Fluor 100×, NA = 1.45 oil immersion objective (Zeiss). The microscope was equipped with diode-pumped crystal lasers (CrystaLaser) as excitation sources. The laser beam was focused to the edge of the back focal plane of the objective, with the incident angle adjusted to be slightly smaller than the critical angle so that the beam was highly inclined and laminated as a thin optical sheet into the cells, a method known as HILO (18). Throughout the experiments, a miniature incubator (Bioscience Tools) mounted on

the microscope stage allowed the temperature to be maintained at 37 °C and the ambient CO_2 concentration at 5%. Cell viability on stage was confirmed for as long as a week. To avoid focal plane drifting, the objective was simultaneously heated and immersion oil with ultralow fluorescence standardized at 37 °C (Cargille) was used. All movies were taken within ~3h after labeling.

Fluorescence images were collected through the objective and detected by a back-illuminated electron multiplying charge-coupled device (EMCCD) camera (Andor iXon DV-897 BV). Typically, each movie lasted 4,000 frames at a frame rate of 20 fps. This time scale is intentionally chosen to be longer than the molecular motor stepping time on microtubules (~1 ms) to filter out the expected noise due to fluctuations on the molecular level, since molecular steps are not the primary interest of this study. The movies were converted into digital format and analyzed using single-particle tracking programs, locating the center of each particle in each frame and stringing these positions together to form trajectories, using software written in-house [17, 39]. The tracking uncertainty is < 5 nm.

We focused on the basal side of the cells. No statistical difference in speed was detected between different positions. To exclude possible artifacts from imperfect statistics, we only analyzed those trajectories longer than 15 s, which is 300 frames. The statistics of the datasets collected in this series of experiments are summarized in Table 6.1.

Discrimination between T and S active motion

Since the T and S phases differ in their directional persistence, it is at first tempting to seek to use minimum spanning tree or other clustering methods based on graphic theory to separate them. However, there is as yet no general solution to this problem [40]. For the problem at hand, we developed the algorithm described below.

Although two qualitatively different types of active motion are obvious to eyes in the original trajectories (Fig. 6.1b), automated discrimination of persistent transport (T) and local

searching (S) performed better on the coarse-grained trajectories depicted in Fig. 6.8. To perform the discrimination automatically, our cluster algorithm began by representing individual runs with "nodes" at their average positions, then connected adjacent nodes with "edges". Short runs, those with curvilinear distances less than 2 μm, at which the angle between edges was less than 4/5π, were flagged as the first guess of S runs. Also, the first and last runs of each trajectory were flagged as S if they were shorter than 1 μm. Then, nodes between two consecutive S runs were flagged as S if the total traveled curvilinear distance was less than 1.5μm. These values of discriminatory distance were chosen empirically to give best performance. All other runs were classified as T runs. As a final adjustment, the S nodes bracketing T runs, were converted to T because they represented the end points of persistent transport periods. Also, singular S nodes were converted to T. For analysis of S and T runs, we constrained ourselves to the trajectories in which at least 6 runs were detected.

6.5 References

1. Welte MA (2004) Bidirectional transport along microtubules. *Curr. Biol.* 14: R525-R537.
2. Roostalu J, *et al.* (2011) Directional switching of the kinesin Cin8 through motor coupling. *Science* 332: 94-99.
3. Presley JF, *et al.* (1997) ER-to-Golgi transport visualized in living cells. *Nature* 389: 81-85.
4. Scholey JM, Anderson KV (2006) Intraflagellar transport and cilium-based signaling. *Cell* 125: 439-442.
5. Hendricks AG, *et al.* (2010) Motor corrdination via a tug-of-war mechanism drives bidirectional vesicle transport. *Curr. Biol.* 20: 697-702.

6. Schuster M, Lipowsky R, Assmann M-A, Lenz P, Steinberg G (2011) Transient binding of dynein controls bidirectional long-range motility of early endosomes. *Proc. Natl. Acad. Sci. USA* 108: 3618-3623.
7. Ally S, *et al.* (2009) Opposite-polarity motors activate one another to trigger cargo transport in live cells. *J. Cell Biol.* 187: 1071-1082.
8. Yildiz A, Tomishige M, Gennerich A, Vale RD (2008) Intramolecular strain coordinates kinesin stepping behavior along microtubules. *Cell* 134: 1030-1041.
9. Bormuth V, Varga V, Howard J, Schäffer E (2009) Protein friction limits diffusive and directed movements of kinesin motors on microtubules. *Science* 325: 870-873.
10. Collinet C, *et al.* (2010) Systems survey of endocytosis by mutiparametric image analysis. *Nature* 464: 243-249.
11. Gould GW, Lippincott-Schwartz J (2009) New roles for endosomes: from vescular carriers to multi-purpose platforms. *Nat. Rev. Mol. Cell Biol.* 10: 287-292.
12. Verhey KJ, Rapoport TA (2001) Kinesin carries the signal. *Trends Biochem. Sci.* 26: 545-549.
13. Reilein A, Yamada S, Nelson WJ (2005) Self-organization of an acentrosomal microtubule network at the basal cortex of polarized epithelial cells. *J. Cell Biol.* 171: 845-855.
14. Marsh BJ, Mastronarde DN, Buttle KF, Howell KE, McIntosh JR (2001) Organellar relationships in the Golgi region of the pancreatic beta cell line, HIT-T15, visualized by high resolution electron tomography. *Proc. Natl. Acad. Sci. USA* 98: 2399-2406.
15. Ross JL, Shuman H, Holzbaur ELF, Goldman YE (2008) Kinesin and dynein-dynactin at intersecting microtubles: motor density affects dynein function. *Biophys. J.* 94: 3115-3125.

16. Müller MJI, Klumpp S, Lipowsky R (2008) Tug-of-war as a cooperative mechanism for bidirectional cargo transport by molecular motors. *Proc. Natl. Acad. Sci. USA* 105:4609-4614.

17. Wang B, Anthony SM, Bae SC, Granick S (2009) Anomalous yet Brownian. *Proc. Natl. Acad. Sci. USA* 106: 15160-15164.

18. Tokunaga M, Imamoto N, Sakata-Sogawa K (2008) Highly inclined thin illumination enables clear single-molecule imaging in cells. *Nat. Methods* 5: 159-161.

19. Kahana A, Kenan G, Feingold M, Elbaum M, Granek R (2008) Active transport on disordered microtubule networks: the generalized random velocity model. *Phys. Rev. E* 78: 051912.

20. Benichou O, Loverdo C, Moreau M, Voituriez R (2011) Intermittent search strategies. *Rev. Mod. Phys.* 83: 81-130.

21. Elf J, Li G-W, Xie XS (2007) Probing transcription factor dynamics at the single-molecule level in a living cell. *Science* 316: 1191-1194.

22. Edwards AM, *et al.* (2007) Revisiting Lévy flight search patterns of wandering albatrosses, bumblebees and deer. *Nature* 449, 1044-1048.

23. Gasman S, Kalaidzidis Y, Zerial M (2003) RhoD regulates endosome dynamics through Diaphanous-related Formin and Src tyrosine kinase. *Nat. Cell Biol.* 5: 195-204.

24. Bulinski JC, McGraw TE, Gruber D, Nguyen HL, Sheetz MP (1997) Overexpression of MAP4 inhibits organelle motility and trafficking in vivo. *J. Cell Sci.* 110: 3055-3064.

25. Dompierre JP, *et al.* (2007) Histone deacetylase 6 inhibition compensate for the transport deficit in Huntngton's disease by increasing tubulin acetylation. *J. Neurosci.* 27: 3571-3583.

26. Dhar A, Chaudhuri D (2002) Triple minima in the free energy of semiflexible polymers. *Phys. Rev. Lett.* 89: 065502.

27. Pangarkar C, Dinh AT, Mitragotri S (2005) Dynamics and spatial organization of endosomes in mammalian cells. *Phys. Rev. Lett.* 95: 158101.

28. Rogers SS, *et al.* (2010) The first passage probability of intracellular particle trafficking. *Phys. Chem. Chem. Phys.* 12: 3753-3761.

29. Zaliapin I, Semenova I, Kashina A, Rodionov V (2005) Multiscale trend analysis of microtubule transport in melanophores. *Biophys. J.* 88: 4008-4016.

30. Arcizet D, Meier B, Sackmann E, Rädler J, Heinrich D (2008) Temporal analysis of active and passive transport in living cells. *Phys. Rev. Lett.* 101:248103.

31. Thompson MA, Casolari JM, Badieirostami M, Brown PO, Moerner WE (2010) Three-dimensional tracking of single mRNA particles in Saccharomyces cerevisiae using double-helix point spread function. *Proc. Natl. Acad. Sci. USA* 107: 17864-17871.

32. Huet S, *et al.* (2006) Analysis of transient behavior in complex trajectories: application to secretory vesicle dynamics. *Biophys. J.* 91: 3542-3559.

33. Percival DB, Walden AT (2000) *Wavelet Methods for Time Series Analysis* (Cambridge University Press).

34. Shubeita G, *et al.* (2008) Consequences of motor copy number on the intracellular transport of kinesin-1-driven lipid droplets. *Cell* 135:1098-1107.

35. Cui B, *et al.* (2007) One at a time, living tracking of NGF axonal transport using quantum dots. *Proc. Natl. Acad. Sci. USA* 104:13666-13671.

36. Kural C, *et al.* (2007) Kinesin and dynein move a peroxisome in vivo: a tug-of-war or coordinated movement? *Science* 308:1469-1472.

37. Yoo D, Wootton SK, Li G, Cheng S, Rowland RR (2003) Colocalization and interaction of the PRRS virus nucleocapsid protein with the small nucleolar RNA-associated protein fibrillarin. *J. Virol.* 77: 12173-12183.

38. Tökési N, *et al.* (2010) TPPP/P25 promotes tubulin acetylation by inhibiting histone deacetylase 6. *J. Biol. Chem.* 285: 17896-17906.

39. Anthony SM, Granick S (2009) Image analysis with rapid and accurate two-dimensional Gaussian fitting. *Langmuir* 25: 8152-8160.

40. Stojmenović M, Nayak A, Zunic J (2008) Measuring linearity of planar point sets. *Pattern Recognit.* 41: 2503-2511.

6.6 Figures

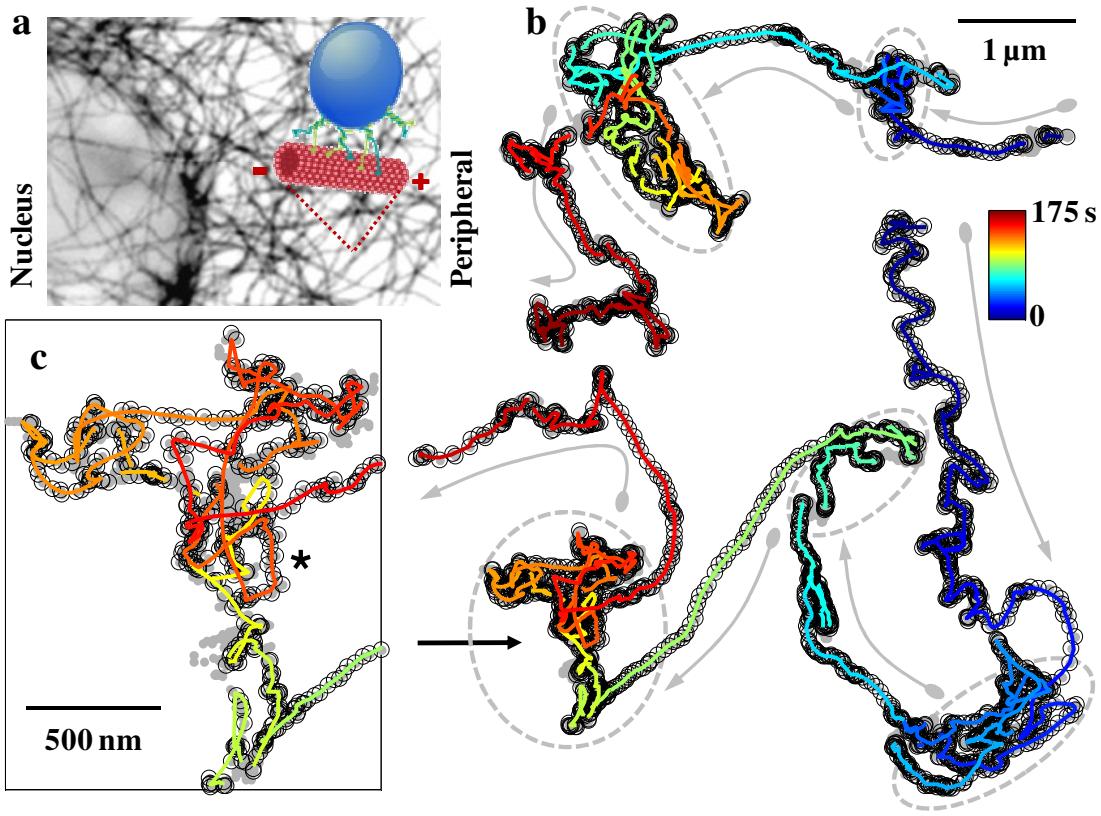

Figure 6.1

Active transport of endosomes along microtubules exhibits two phases, persistent transport (T) and local searching (S). (a) Illustration that cargos are actively transported through microtubule networks in cells with length scale set by mesh size ξ. The inset illustrates a heuristic model of what happens on the molecular scale— cargo is dragged by motor proteins as they walk along the microtubules either to plus (cell periphery) or minus (perinuclear space) ends. (b) Two representative trajectories of individual EGF-containing endosomes in HeLa cells. The smoothened paths of active transport shown as lines with color denoting the elapsed time are overlaid on the original tracked positions (gray dots) with the active portion detected by wavelet analysis highlighted by black open circles (see Methods). The flow of alternating T and S periods is indicated by arrows and dashed circles respectively. An S period is magnified in (c). The asterisk highlights a closed loop in the trajectory.

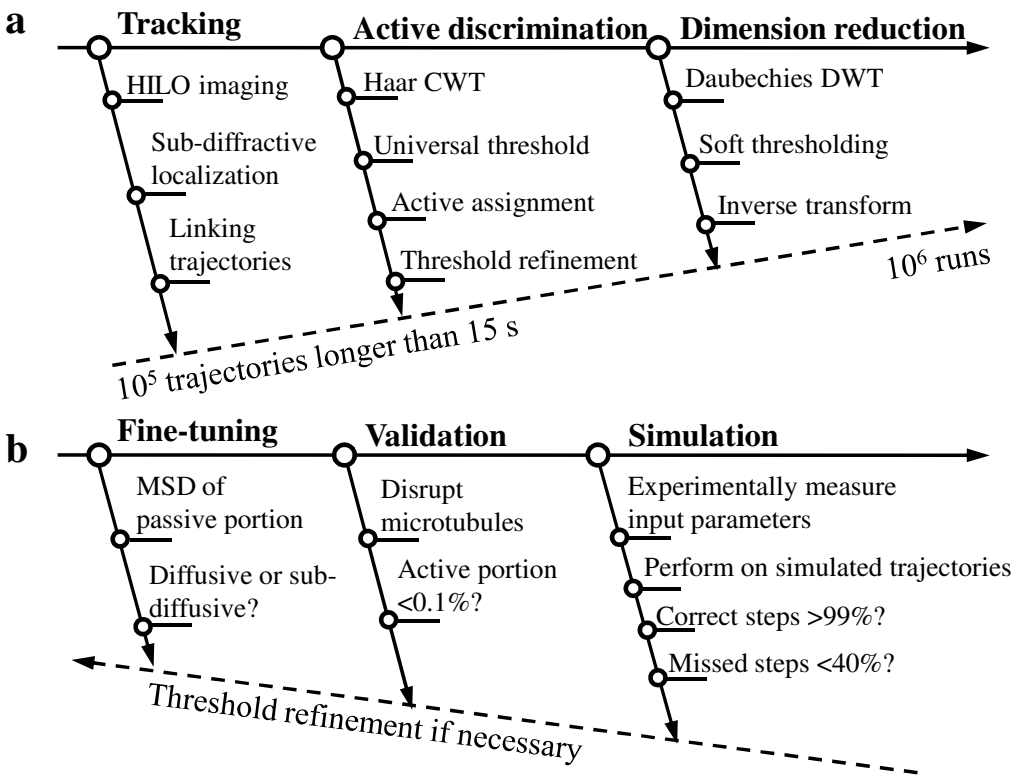

Figure 6.2

Flow chart of the methods used in this study. For details see Methods.

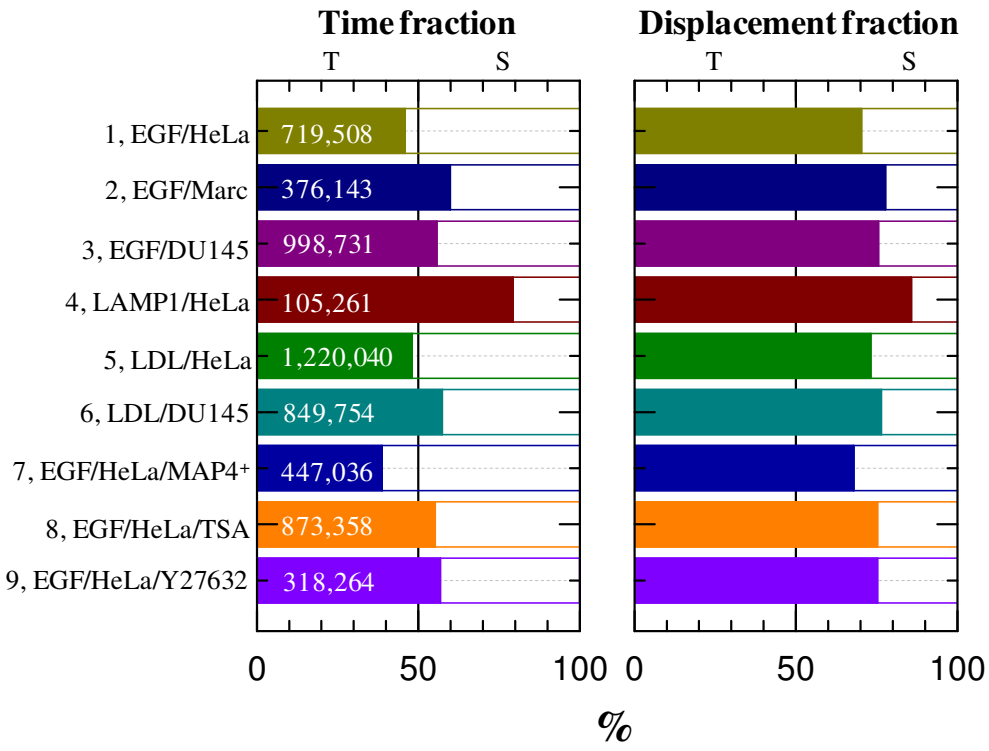

Figure 6.3

Chart summarizing the robust observation of biphasic active transport across 9 situations of live cell transport. This includes 3 mammalian cell lines, variation of different motor type and scaffold protein, decoration of microtubules with protein, and modulation of the cytoskeleton. The time fraction (left column) and displacement (defined as the end-to-end distance of individual periods) fraction (right column) of persistent transport, T (filled bars), and local searching, S (open bars) are plotted for each condition. For each condition, the total number of active frame-to-frame steps (frame rate 20 fps) is also reported. More complete statistics are specified in Table 6.1.

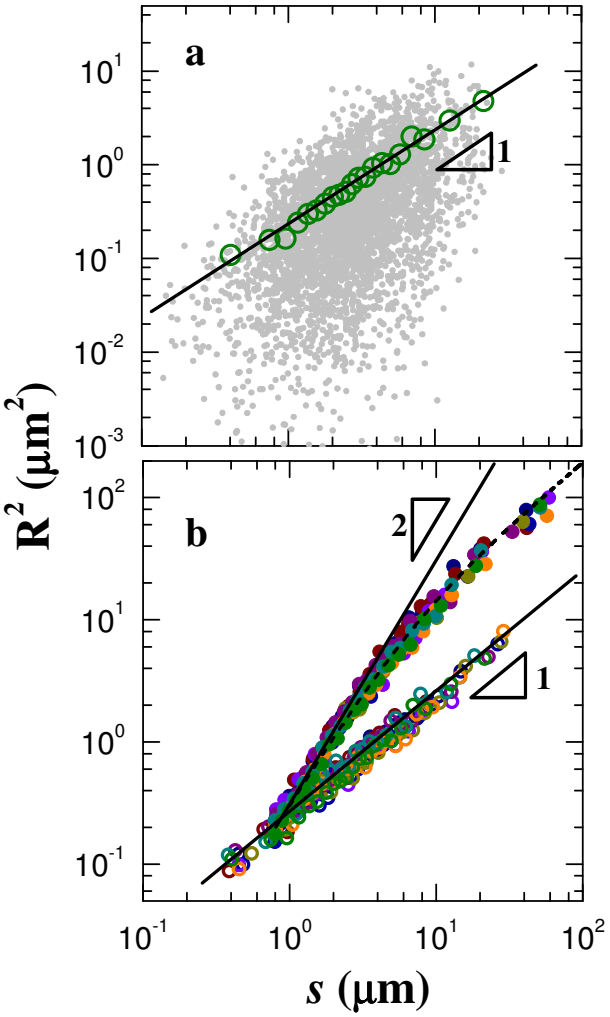

Figure 6.4

The transport T and searching S phases follow different scaling laws. (a) Log-log plot of squared displacements made in S periods of LDL-containing endosomes in HeLa cells (R^2) versus their curvilinear distance along microtubules (s). To correct transverse fluctuations, the curvilinear distance was calculated only along the smoothened track (see Methods). The circles, averaged from ~4,000 periods (raw data shown as grey dots), have the slope indicated in the figure. (b) Collapse of such data for all 9 conditions in Fig. 6.3, using the same colors as in Fig. 6.3. The solid lines, with indicated slopes, highlight power law scaling. The dashed line represents the fit to the Kratky-Porod model $\left\langle R^2 \right\rangle \propto l_p s - 2l_p^2\left(1-\exp\left(-\frac{s}{l_p}\right)\right)$, where $l_p \approx 3\mu m$. Note that in this model, the slope at small s is 2 but at infinitely large s it is 1, i.e. $\left\langle R^2 \right\rangle \approx 2l_p s$. This is why the data confirm the slope of 2 and, at the largest observed s, continue to bend downward towards the slope of 1.

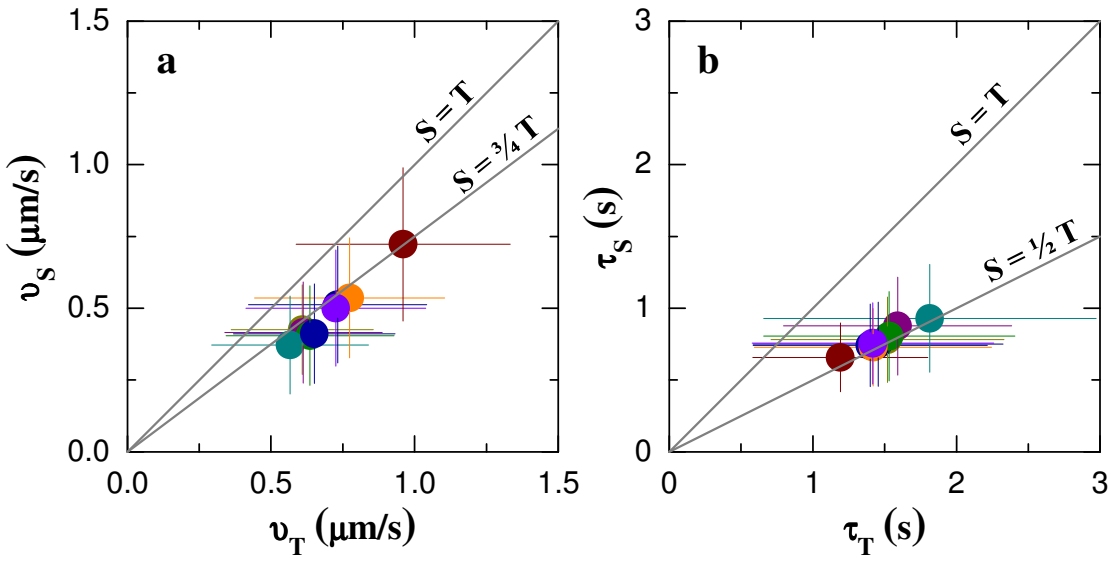

Figure 6.5

The mean speed and run time are regulated differently in S and T phases. The mean speed (a) and run time (b) of active transport in the searching S phase are plotted versus those in the transport T phase, falling phenomenologically on lines with slopes of ¾ and ½, respectively. The frame-to-frame speed was defined as displacement along the smoothened track divided by the time between frames (50 ms). The color representation is the same as in Fig. 6.3. The error bars are half a standard deviation. The large spread of the data is due to the intrinsic heterogeneity of intracellular transport. Averaging over our large datasets, measurement uncertainty is less than the size of the data points.

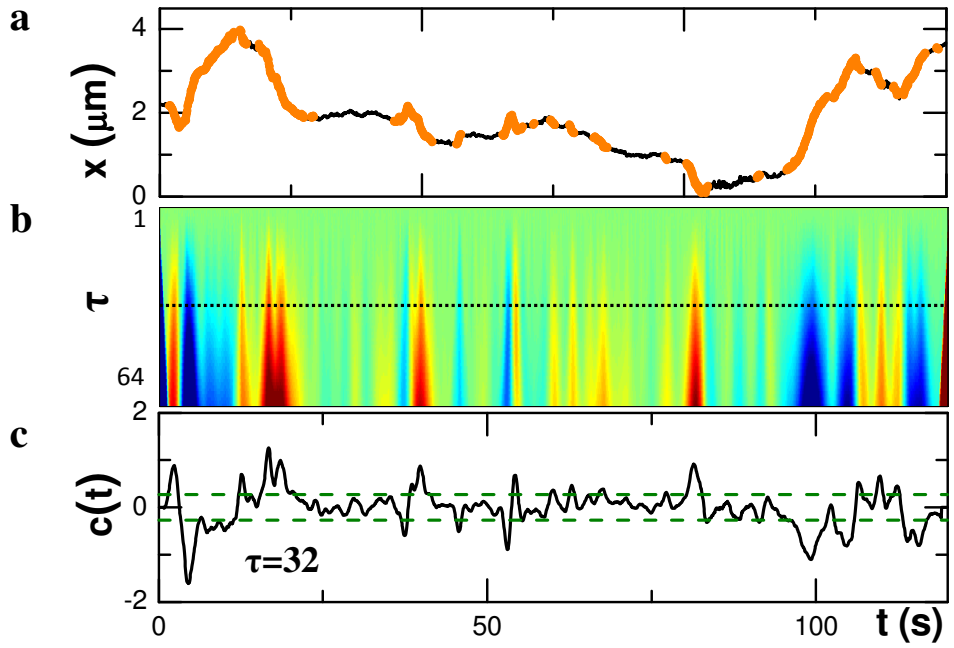

Figure 6.6

Wavelet analysis to distinguish active transport from passive motion. (a) A representative 1D trajectory of an EGF-containing endosome in a living Marc-145 cell and (b) its Haar continuous time wavelet transform (CWT) are plotted versus time. The vertical axis of (b) is scale τ, ranging from 1 to 64 time steps. A cross section at scale 32, corresponding to the dashed line in (b), is shown in (c). (b) is color coded with the same scale as (c) so that red and blue colors correspond to positive and negative coefficients, respectively. Dashed lines in (c) show the threshold above which the periods are identified as active transport for this trajectory. Combining the periods with coefficients above this threshold on either *x* or *y* spatial dimensions, the active 'runs' detected are highlighted in orange as in (a). Runs with reversed directions are automatically separated.

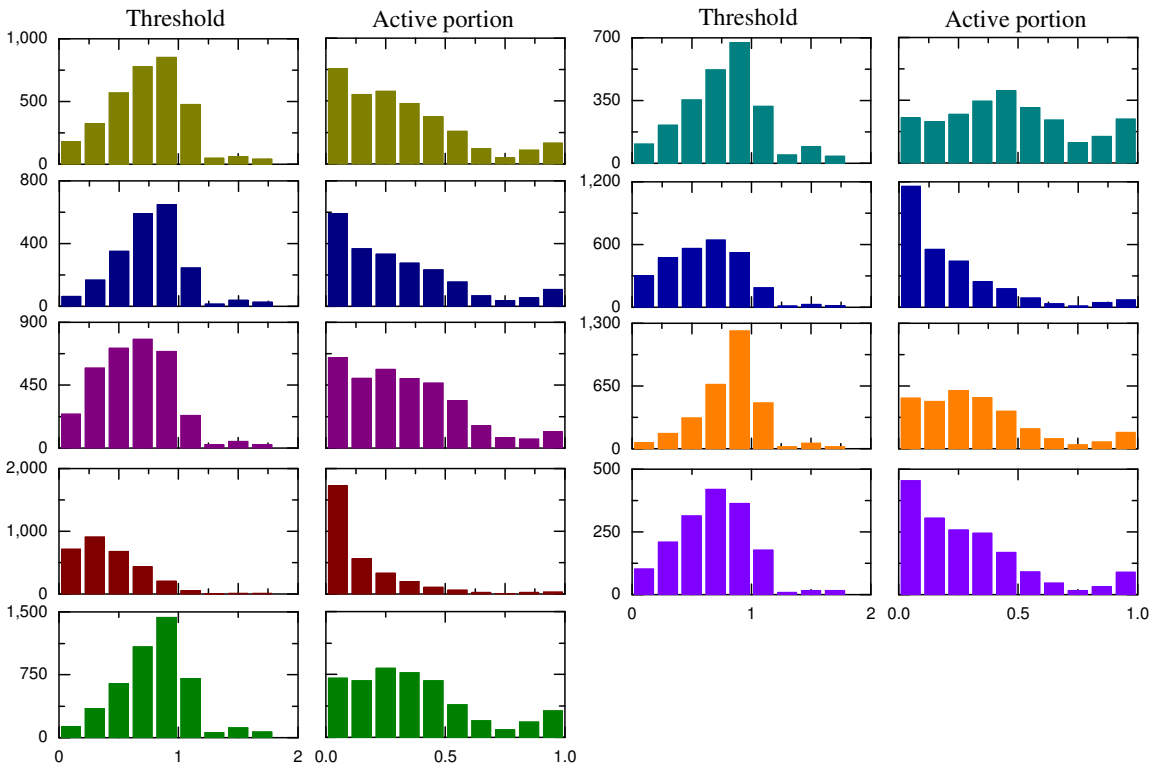

Figure 6.7

Histograms of the thresholds used and the active portions of individual trajectories under different experimental conditions. The color representation is the same as in Fig. 6.3. The active portion of individual trajectories is defined as the ratio of the number of detected active frame-to-frame steps to the total number of steps for that particular trajectory, where the total number of active steps include both T and S phases.

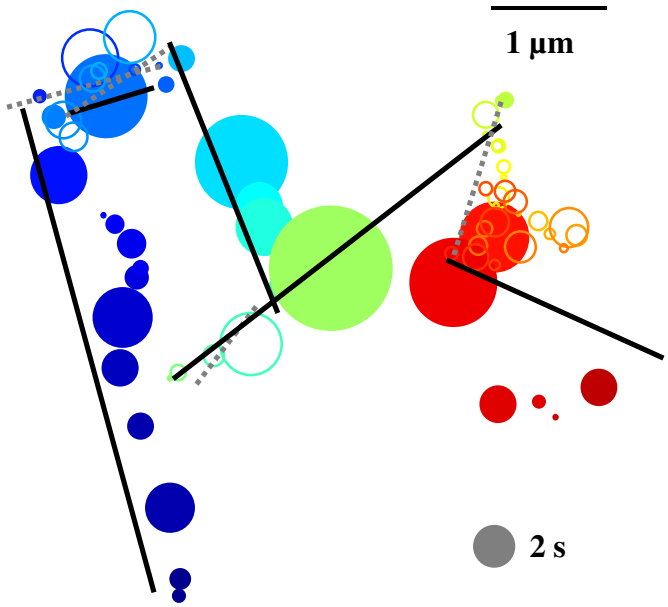

Figure 6.8

Coarse-grained representation of the active transport on the level of runs. Each circle represents an individual run, centered at the average position of that particular run with color denoting the elapsed time as same as Fig. 6.2b and size scaling with the duration. The clustering algorithm groups automatically the runs into transport periods (filled circles, solid lines) and searching periods (open circles, dashed lines), with lines linking the starting and end positions of that period, from which displacements can be measured.

6.7 Table

Table 6.1

Statistics of the datasets in this study.

Experiment[a]	Trajectories >15 s			Trajectories with >6 runs		
	# total steps[b]	#trajectories	#runs	# active steps[b]	#trajectories	#runs
1	3,325,395	3,443	44,058	719,508	1,691	36,837
2	1,786,336	2,222	21,131	376,143	1,159	17,966
3	3,754,471	3,424	47,303	998,731	2,148	43,095
4	1,777,094	3,082	10,445	105,261	538	5,202
5	4,552,263	4,833	64,349	1,220,040	3,250	59,028
6	2,561,474	2,552	35,837	849,754	1,780	33,186
7	2,945,105	2,826	28,552	447,036	1,319	22,458
8	3,519,079	3,125	47,578	873,358	2,137	44,221
9	1,547,366	1,702	17,725	318,264	949	15,601

[a] experimental conditions are the same as in Fig. 6.3.

[b] steps of 50 ms (time interval between adjacent frames).

CHAPTER 7

BURSTS OF ACCELERATION DURING ACTIVE TRANSPORT

The contents of this chapter are based on a manuscript in preparation by Bo Wang, Jame Kuo, Sung Chul Bae, and Steve Granick.

7.1 Background

One of the most fundamental differences between the inanimate and living world is that while transport of matter owing to diffusion in the former is well advanced by work dating to Einstein and earlier, active transport in living systems is driven by the proteins known as molecular motors [1]. These molecular machineries underpin essential functions, among them locomotion, cell cycle, signaling and intracellular transport. Present understanding of this problem has focused on the molecular mechanisms of elementary steps taken by the motors [2-5], but how these steps coordinate in the context of crowded cellular environment remains unknown. Progress has been impeded by the paucity of methods to perform live-cell imaging with high quality at the single-particle level, as well as by difficulties to separate active from passive transport. Predicating this study on advances regarding both of these impediments as described in chapter 7, here we reveal large nonlinearities of cargo transport within living cells. Statistical commonality with driven motion in jammed nonliving system manifests its conceptual connection to delocalization in glassy dynamics.

Significant nonlinear effects are expected when a particle is dragged by an external force in model glass forming/jammed systems due to their intrinsic dynamic heterogeneity [6-11]. The particle needs to be pulled free out of its transient neighbor cage, with the surrounding structure

distorted and local stress relaxed accordingly. With the analogy between cell mechanics and soft glass in mind [12,13], this expectation led us to the hypothesis that as a vesicular cargo, such as endosome or lysosome, dragged by motor proteins (say kinesin or dynein) along a microtubule (MT) through the crowded, heterogeneous cytoplasm of a living cell (Fig. 7.1a), speed would decrease as stress builds up, the environment pushing against cargo motion; then, bursting free, the cargo would speed up. While on short time and length scales of ~10 nm and ~1 ms the dynamics is dictated by the molecular kinetics, slow structural rearrangement instead overrules the cargo transport on larger scales, ~100 nm and ~1 s.

7.2 Results and Discussions

To test this hypothesis, we re-analyzed the data obtained in chapter 6, but with emphasis on fluctuations of the frame-to-frame speed on scales shorter than individual runs, therefore smaller than what has been examined there.

A typical run of uninterrupted motion in one direction is illustrated by the raw data in Fig. 7.1b. Temporally-resolved speed versus time in other discrete runs (Fig. 7.2a) reveals large fluctuations, different from ordinary noise around a mean value. Plotting speed against acceleration (which physically relates to the product of relaxation function of the viscoelastic environment and the strain rate), the beautiful spiral patterns show that the speed fluctuations have a nonlinear dynamic feature with memory as long as a second (Fig. 7.2b), a time that coincides with the known typical mechanical relaxation time of cells [13]. Limit cycles are not observed, so this motion is not periodic, but the circuits are strikingly parallel and tilted. In other words, while fluctuations differ in both amplitude and time, their shapes are similar and they are regularly asymmetrical with time. We tracked a large number of cells, >50 cells for each experimental condition. Similar patterns were verified for >10,000 runs under each experimental condition. The mean values of speed, run time, and run length agree with reported values in the

literature [4]. The speed fluctuations do not appear to cluster into distinct values, nor do they have distinct peaks of multiple Gaussian distributions, features that would be expected if they reflect motor association-dissociation events [2, 14]. The observed nonlinearity cannot be explained by any existing molecular theories but is consistent with our hypothesis.

Fig. 7.3 plots the ensemble averaged speed-speed autocorrelation functions of active cargo transport, confirming the long memory with major negative correlation peaks at ~0.3 s. The negative peaks are expected as a cage effect, and are truly broad indicating a broad distribution of the time scales of the fluctuations, a ubiquitous feature of dynamic heterogeneity. Oppositely, sharp peaks corresponding to a well-defined time scale is anticipated if the observed nonlinearity is induced by a specific molecular cycling mechanism.

Proceeding with quantification, we analyzed the duration and traveled distance of each fluctuation cycle. Given a time series of speed $v(t)$ for a single run, we imposed a reference $\tilde{v}$ defined at 60% of the most likely speed in this run, and assigned periods of time when speed exceeded this reference level as bursts. This reference speed was chosen to match the average burst time (Fig. 7.4) with the major fluctuation frequency read from the ensemble speed-speed autocorrelation functions (Fig. 7.3). Each burst has a duration T measured as the time interval between two successive intersections of $v(t)$ with $\tilde{v}$ and a distance traveled within this run, the burst length L. Strikingly, the averaged burst length of certain duration scales with duration as a power law, $L \sim T^{\frac{3}{2}}$, over more than two decades (Fig. 7.5a). This power, independent of where the reference is assigned, matches that expected from crackling noise in critical inanimate systems [6,15]. The scaling length L_0 provides a typical length scale of the bursts under that condition (Fig. 7.5b), speculatively connecting to the specific details such as cargo size, number of motors bound, and molecular regulation. All bursts fall on the same master curve, after time t has been rescaled by burst-specific duration T and speed rescaled by $T^{\frac{1}{2}}$ (Fig. 7.5c). The

asymmetry in this time-averaged data is consistent with the picture that as cargo moves, dragged by molecular motors, at first stress builds up such that motion slows, then it releases and motion speeds up. Although the exact shape should depend on the detailed relaxation mechanism of the environment, the initial acceleration during which speed increases linearly with time (Fig. 7.5c right) appears to reflect release of elastic stress. The power of 3/2 is consistent with the simple heuristic argument that these data reflect the superposition of ballistic motion and random Brownian noise [16]. Thus, although at the molecular level this endogenous transport surely involves complex regulatory pathways and genes, this complexity displays coarse-grained scale-free simplicity.

This series of phenomena is universal to changing the molecular details (Fig. 7.3 and Fig. 7.5). The data all collapse when changing the cell line, from HeLa to Marc-145 or DU145, and varying the organelles from epidermal growth factor (EGF) containing endosomes to low-density lipoprotein (LDL) containing endsomes, and then to lysosomal-associated membrane protein 1 (LAMP1) tagged lysosomes, since they are carried by different motor and scaffolding proteins. We overexpressed microtubule-associated protein 4 (MAP4) as MAP4 is known to act as a road blocker on microtubules. We acetylated the microtubule by inhibiting the histone deacetylase with trichostatin A, since acetylation is expected to enhance the processivity of the motors. The scaling is insensitive to these changes. This striking invariance highlights the redundancy in regulation of cellular active transport, which in turn relates to universality in cell mechanics that has been proposed by others [12,13].

Modulating the cytoskeleton with latrunculin A (LatA) or cytochalasin D (CytoD), which both dissemble actin filaments, or Y-27632 to selectively inhibit Rho-associated protein kinase p160ROCK changes to 2 the scaling power of bursts less than $L = 100$ nm and $T = 0.3$ s (Fig. 7.5a, bottom panel) and also consistently shifts the typical burst lengths (Fig. 7.5b). Significantly, $L = 100$ nm coincides with the intracellular mesh size of actin networks, above which the contribution of cytoskeleton is expected to average out; it is reasonable to observe differences only for L

smaller than this. Consistently, after actin disruption, the first minimum in speed-speed autocorrelation curves becomes shallower, indicating a shift towards longer times (Fig. 7.3b).

7.3 Conclusions

In summary, temporally-resolved speed of active transport in living cells shows striking statistical regularities over scales that exceed the nanometers and milliseconds attributable to individual steps of discrete molecular motors. The universality of the scale-free power law scaling observed which is independent of the molecular details, and its quantitative agreement with those reported in inanimate systems (jammed colloids and granular media, and magnetic Barkhausen noise [6,15], suggest a common origin in pushing through a crowded environment in weak force regime.

7.4 Materials and Methods

To disrupt the actin networks, either 0.08 μg/mL LatA or 0.75 μg/mL CytoD was added 30 min before imaging. At these concentrations, blebs formed at cell peripheries but cells retained their shapes and no complete rounding was observed within 3 h. Other experimental details are described in chapter 6.

The ensemble autocorrelation function was defined as $R(\Delta t) = \left\langle \frac{v_i(t) \cdot v_i(t+\Delta t) - \bar{v}_i^2}{\sigma_i^2} \right\rangle_{i,t}$, where $\bar{v}$ and σ^2 are the mean and variance of this time series of speed, respectively, and the bracket denotes averaging over all trajectories and time. However, this definition is rigorous only for stationary processes, where the mean and variance do not change with time. This is not necessarily true for active transport, since the number of molecular motors at work could fluctuate with time and the cytoplasm is highly heterogeneous. To compute the autocorrelation consistently, we cropped runs longer than 50 frames into pieces

of length 50 frames or shorter, assuming the mean and variance would not change significantly during this time. An inevitable cost of this cropping is that correlations longer than 2 s are not reliable. As their mean and variance would not be statistically significant, runs shorter than 10 frames were excluded from this analysis.

7.5 References

1. Prost J, Joanny JF, Parrondo JMR (2009) Generalized fluctuation-dissipation theorem for steady-state systems. *Phys. Rev. Lett.* 103:090601.
2. Müller MJI, Klumpp S, Lipowsky R (2008) Tug-of-war as a cooperative mechanism for bidirectional cargo transport by molecular motors. *Proc. Natl. Acad. Sci. USA* 105:4609-4614.
3. Bormuth V, Varga V, Howard J, Schäffer E (2009) Protein friction limits diffusive and directed movements of kinesin motors on microtubules. *Science* 325: 870-873.
4. Shubeita G, *et al.* (2008) Consequences of motor copy number on the intracellular transport of kinesin-1-driven lipid droplets. *Cell* 135:1098-1107.
5. Hirokawa N, Noda Y, Tanaka Y, Niwa S (2009) Kinesin superfamily motor proteins and intracellular transport. *Nat. Rev. Mol. Cell Biol.* 10: 682-696.
6. Candelier R, Dauchot O (2009) Creep motion of an intruder within a granular glass close to jamming. *Phys. Rev. Lett.* 103:128001.
7. Hastings MB, Olson CJ, Reichhardt C (2003) Depinning by fracture in a glassy background. *Phys. Rev. Lett.* 90:098302.
8. Gazuz I, Puertas AM, Voigtmann Th, Fuchs M (2009) Active and nonlinear microrheology in dense colloidal suspensions. *Phys. Rev. Lett.* 102: 248302.
9. Jack RL, Kelsey D, Garrahan JP, Chandler D (2008) Negative differential mobility of weakly driven particles in models of glass formers. *Phys. Rev. E* 78: 011506.

10. Zia RN, Brady JF (2010) Single-particle motion in colloids: force-induced motion. *J. Fluid Mech.* 658: 188-210.
11. Habdas P, Schaar D, Levitt AC, Weeks ER (2004) Forced motion of probe particle near the colloidal glass transition. *Europhys. Lett.* 67: 477-483.
12. Zhou EH, *et al.* (2009) Universal behavior of the osmotically compressed cells and its analogy to the colloidal glass transition. *Proc. Natl. Acad. Sci. USA* 106:10632-10637.
13. Trepat X, Lenormand G, Fredberg JJ (2008) Universality in cell mechanics. *Soft Matter* 4:1750-1759.
14. Arcizet D, Meier B, Sackmann E, Rädler J, Heinrich D (2008) Temporal analysis of active and passive transport in living cells. *Phys. Rev. Lett.* 101:248103.
15. Sethna JP, Dahmen KA, Myers CR (2001) Crackling noise. *Nature* 410:242-250.
16. Baldassarri A, Colaiori F, Castellano C (2003) Average shape of a fluctuation: universality in excursion of stochastic processes. *Phys. Rev. Lett.* 90:060601.

7.6 Figures

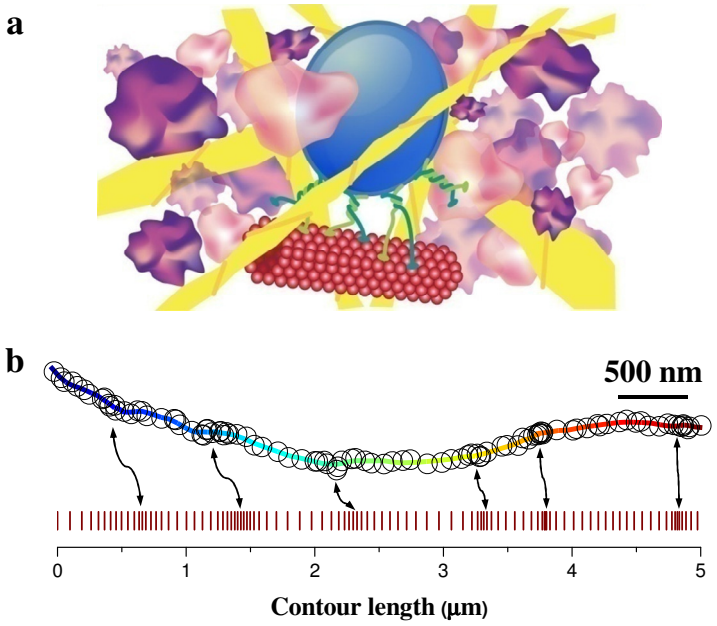

Figure 7.1

The main idea of this experiment. (a) The vesicle is dragged by molecular motors stepping on microtubules with the environment blocking motion transiently. Color representation: yellow, cytoskeleton; purple, cytoplasm. (b) A representative uninterrupted "run" lasting 5 s of EGF containing endosomes in HeLa cells, circles representing the raw position data obtained from tracking, the color denoting elapsed time. After accounting for transverse fluctuations of the microtubule and swinging of vesicles perpendicular to it, positions with constant time step (50 ms) along the contour of the track are shown on the bottom horizontal line. The arrows identify the demarcation between slow periods separated by fast bursts during this run of uninterrupted motion in one direction.

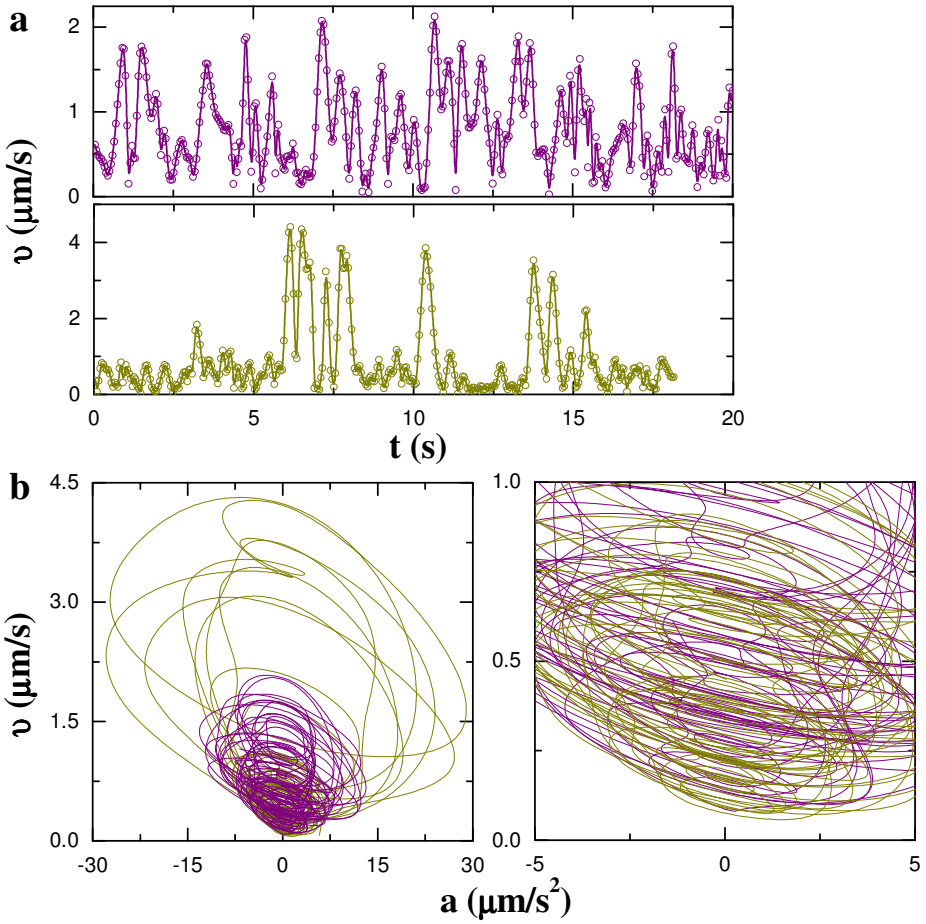

Figure 7.2

Speed fluctuations of endosomes transported along microtubules. (a) Two representative runs of EGF-containing endosomes in HeLa cells with temporally-resolved speed, evaluated over 50 ms intervals, plotted versus time. The fluctuation is one order of magnitude bigger than the measurement uncertainty, 0.2 μm/s. (b) The same two time series are plotted as instantaneous speed versus acceleration (left) with a magnified view near the origin (right).

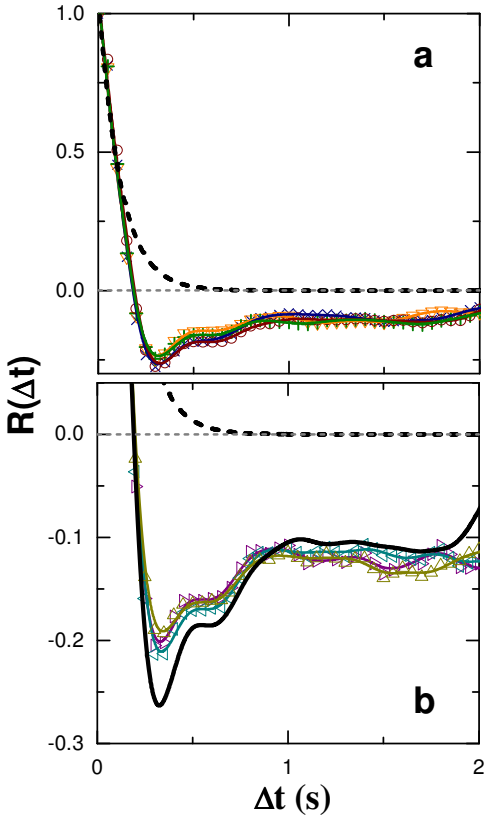

Figure 7.3

The ensemble-averaged speed-speed autocorrelation function $R(\Delta t)$ of active transport. In (a), the shape of $R(\Delta t)$ vs. Δt is invariant to experimental conditions. (b) illustrates the effect of cytoskeleton. The symbol representations are the same as in Fig. 7.5. The solid line depicts the average curve of cytoskeleton intact samples. The dashed lines represent fits as single exponential decay.

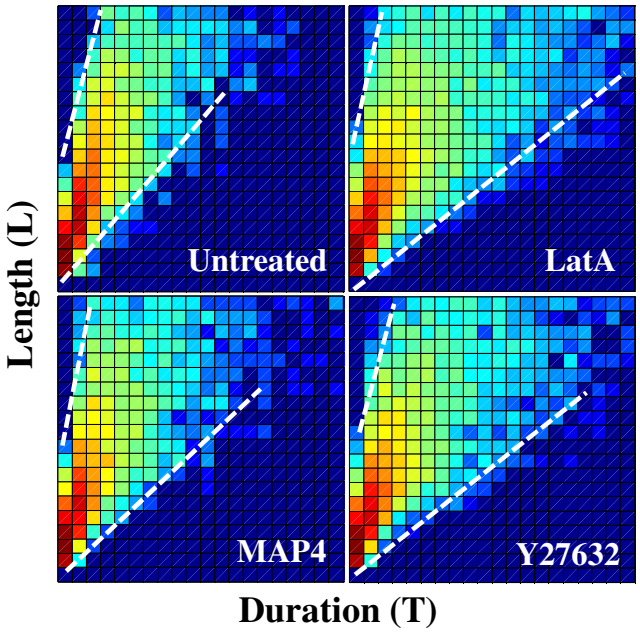

Figure 7.4

2D probability distributions of 'burst' duration and length of EGF-containing endosomes in untreated HeLa cells, as well as cells with MAP4 over-expression or treated with LatA (0.08 µg/mL) or Y-27632 (50 µM). The durations spanning 0-1 s and lengths 0-1 µm are shown. The binning width of the length is 50 nm. The color is coded as the logarithmic probability covering 2 orders of magnitude. The approximate ranges of dispersion are indicated by dashed lines.

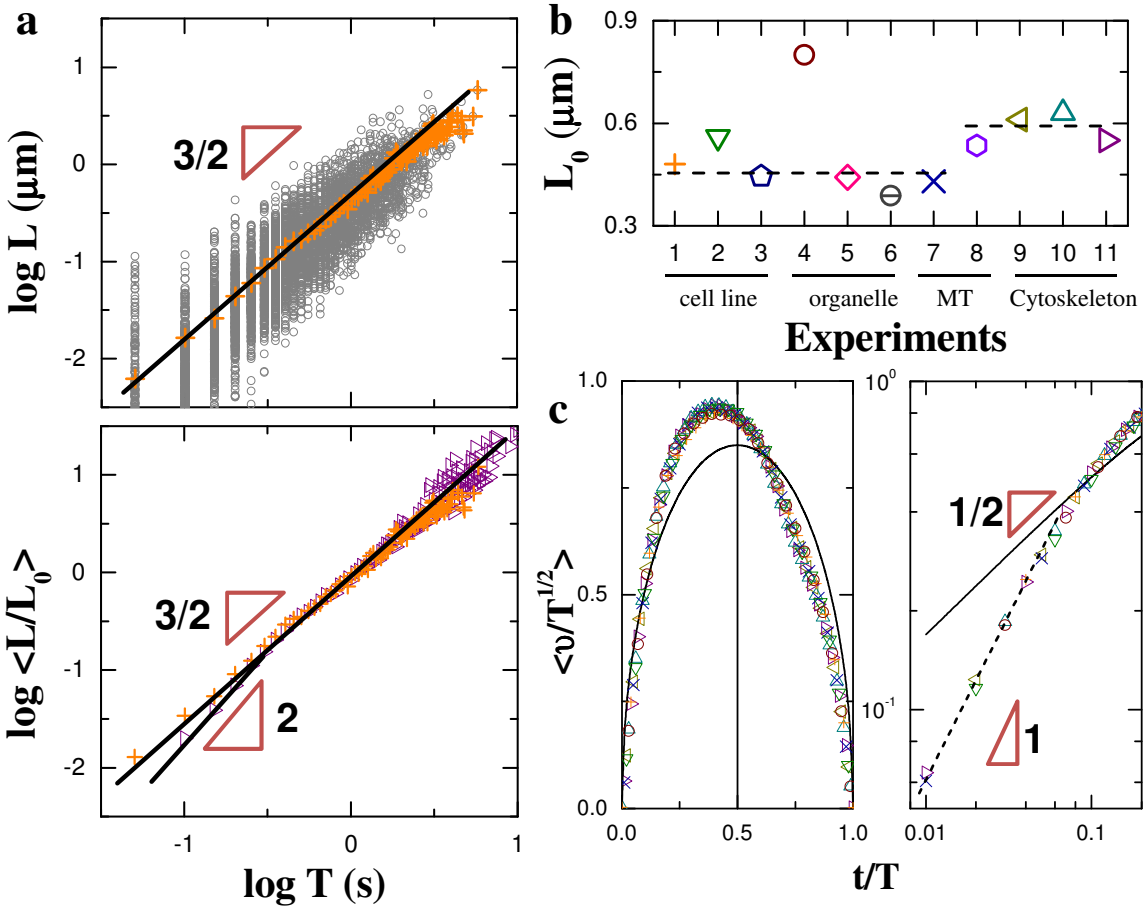

Figure 7.5

Scaling of speed fluctuations for the active transport of endosomes and lysosomes. (a) Top: Log-log plot of burst length (L) versus their duration (T); these data refer to EGF-containing endosomes in HeLa cells. The crosses, averaged from 26,496 bursts (raw data shown as grey circles), have the slope indicated in the figure. Bottom: Collapse of such data after modulating the cytoskeleton when comparing L/L_o, where L_o differs between systems. The solid lines have the slopes indicated in the figure, highlighting a change of the power law when $L < 100$ nm and $T < 0.3$ s. (b) The length L_o for collapsing data under different conditions in which the cell line and organelle are varied, microtubules are decorated and cytoskeleton is disturbed. The dashed lines indicate systematic shift of L_o to longer length upon actin disruption. The experiments are EGF containing endosomes in, 1, HeLa cells, 2, Marc145 cells, and, 3, DU145 cells; 4, LAMP1 labeled lysosomes in HeLa cells; LDL containing endosomes in, 5, HeLa cells, and, 6, DU145 cells; EGF containing endosomes in HeLa cells, 7, with MAP4 overexpression, 8, treated with TSA; 9, treated with Y27632; 10, with LatA; 11, with CytoD. Corresponding symbol representations are used through all figures. (c) The average burst shape, obtained by normalizing all bursts longer than 0.3 s to the same duration (T) and area (left). Compared to the solid line, a semicircle, the asymmetry of the data is evident. The tail for small fractional period, t/T, is plotted on log-log scales (right). The dashed line has slope of 1 indicating an accelerating stage. The tail of the semicircle (solid line) has slope close to 1/2. The data under all conditions collapse.

APPENDIX A

LIPOSOME DIFFUSION IN BIOPOLYMER NETWORKS

The contents are based on experiments done by Bo Wang, James Kuo, and Steve Granick.

Probe diffusion in polymer meshes, one of the classical issues in polymer physics [1], has been rejuvenated recently as a scientific problem due to its relevance in nanocomposites [2], supercooled liquids [3], and transport in biological environments [4]. In one over-simplified limit, when the probe size is comparable to the structural length scales of the polymer networks (often the mesh sizes), the probe diffusion can be extremely sensitive to even small changes in the size or interfacial interactions between the probe and polymers [3]. Careful studies of probe diffusion therefore demand thorough characterizations of these details. In this context, liposomes present an attractive platform, due to their controllable size and kaleidoscopic lipid types accessible to form vesicles.

As a modification of the traditional extrusion method, liposomes were prepared through a two-step ultrasonication procedure, bath sonication for 10 min followed by tip-sonication for 1 min (Branson sonifier at 65% amplitude, i.e. power of 13-14 W), after N_2 drying and hydration of the lipids. Then the suspensions were forced through polycarbonate filter membranes with defined pores sizes: this procedure presumably yields liposomes of diameter close to the pore size, while the exact number should be affected by the sonication power and extrusion pressure [5]. Noteworthy is that the liposome sizes also depend heavily on the lipid type used (Table A1), exhibiting an unexpected phenomenological positive correlation between the diameter and the bending modulus of the lipid bilayer [6,7]. Adding polyethylene glycol (PEG) conjugated lipids

into the lipid bilayer at a molar percentage of 10% consistently generated liposomes with size of 90±10 nm regardless of the pore size in filter membranes, which could be rationalized as a consequence of molecular packing from a thermodynamics standpoint [8]. These observations highlight the need for extra care when dealing with these samples in order to avoid ambiguity in further data interpretation.

An advantage of liposomes is that their surface chemistry can be easily tailored by using different type of lipids. Vesicles can be made negatively charged by doping the membrane with phosphatidylserine (PS) or phosphatidylglycerol (PG) molecules; positive charges can be introduced by cationic lipids such as lipids with headgroup of trimethylammonium-propane (TAP). Fluorescently labeled lipids and hydrophobic dyes can be mixed in with molar percentage as high as 2%, at this percentage the liposomes remain intact and the fluorescence signals are bright enough for single particle tracking experiments. Phosphocholine zwitterionic dipoles repel nonspecific adsorption due to a hydration layer bound through solvation of the charged terminal groups [9], which naturally eliminate the interaction between liposome probes and polymers. This effect can be enhanced by decorating bilayers with 5-10% of PEG-lipid conjugates [8,10]. It is worth mentioning that this high density of PEGylation is challenging to achieve through other chemical modifications of nanoprobes with sizes smaller than 200 nm. Illustrated in Fig. A1-A3, this non-stickiness has offered us an opportunity to measure the probe diffusion in biopolymer networks, Matrigel and nematic F-actin [11] in particular, at very high protein concentrations, where residual nonspecific interactions are expected to completely trap the probes [12]. An interesting extension along the line would be to probe the microscopic structure of nematic F-actin solutions with diffusion, when the macroscopic viscosity increases upon introducing divalent ions [11].

Instead of single point behavior, we also studied two-point cross correlation of the thermal motions, as this is anticipated to render the measurements insensitive to twisting concerns of detailed chemistry and local interactions. The measured longitudinal displacement correlations

of vesicles in F-actin network present unexpected long-ranged oscillations of diffusive nature (Fig. A4), a behavior that differs completely from expectations based on continuum approximations [13].

References

1. Langevin D, Rondelez F (1978) Sedimentation of large colloidal particles through semidilute polymer solutions. *Polymer* 19:875-882.
2. Tuteja A, Mackay ME (2007) Breakdown of continuum Stokes-Einstein relation for nanoparticle diffusion. *Nano Lett.* 7:1276-1281.
3. Wong IY, *et al.* (2004) Anomalous diffusion probes microstructure dynamics of entangled F-actin networks. *Phys. Rev. Lett.* 92: 178101.
4. Lai SK, Wang YY, Hida K, Cone R, Hanes J (2010) Nanoparticles reveal that human cervicovaginal mucus is riddled with pores larger than viruses. *Proc. Natl. Acad. Sci. USA* 107:598-603.
5. Hunter DG, Frisken BJ (1998) Effect of extrusion pressure and lipid properties on the size and polydispersity of lipid vesicles. *Biophys J.* 74: 2996–3002.
6. Rawicz W, Olbrich KC, McIntosh T, Needham D, Evans E (2000) Effect of chain length and unsaturation of elasticity of lipid bilayers. *Biophys J.* 79: 328–339.
7. Allende D, Simon SA, McIntosh TJ (2005) Mellittin-induced bilayer leakage depends lipid material properties: evidence for toroidal pores. *Biophys J.* 88: 1828-1837.
8. Rovira-Bru M, Thompson DH, Szleifer I (2002) Size and structure of spontaneously forming liposomes in lipid/PEG-lipid mixtures. *Biophys J.* 83: 2419-2439.
9. Chen S, Zheng J, Li L, Jiang S (2005) Strong resistance of phosphorylcholine self-assembled monolayers to protein adsorption: insights into nonfouling properties of zwitterionic materials. *J. Am. Chem. Soc.* 127: 14473-14478.

10. Noppl-Simson AD, Needham D (1996) Avidin-biotin interactions at vesicle surfaces: adsorption and binding, cross-bridge formation, and lateral interactions. *Biophys J.* 70: 1391-1401.
11. Viamontes J, Oakes PW, Tang JX (2006) Isotropic to nematic liquid crystalline phase transition of F-actin varies from continous to first order. *Phys. Rev. Lett.* 97: 118103.
12. Valentine MT, *et al.* (2004) Colloid surface chemistry critically affects multiple particle tracking measurements of biomaterials. *Biophys J.* 86: 4004-4014.
13. Crocker JC, *et al.* (2000) Two-point microrheology of inhomogeneous soft materials. *Phys. Rev. Lett.* 85:888-891.

Figures

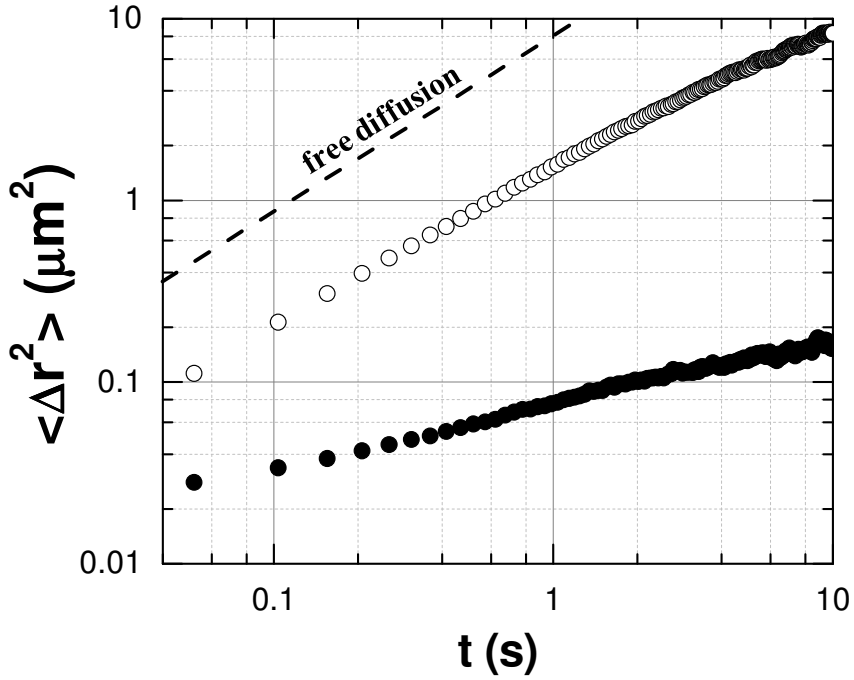

Figure A1

Mean squared displacements (MSDs) of 90 nm DOPC/DOPE-PEG liposomes diffusing in Matrigel with concentration of 9.7 mg/mL (filled symbols) and 4.85 mg/mL (open symbols) are plotted against logarithmic time. Free diffusion of the same sized probe is indicated by the dashed line. Matrigel (BD Biosciences) is a gelatinous protein mixture secreted by Engelbreth-Holm-Swarm (EHS) mouse sarcoma cells, with laminin (56%), collagen IV (31%) and enactin (7%) as major components. The PEG conjugated lipid, 1,2-dioleoyl-*sn*-glycero-3-phosphoethanolamine-N-[methoxy(polyethylene glycol)-750] (DOPE-PEG) with PEG molecular weight of 750, is supplemented in the lipid mixture at molar percentage of 10% before hydration. Importantly, the resistance to protein adsorption was confirmed by imaging the undyed liposomes incubated overnight with fluorescently labeled bovine serum albumin (BSA) and G-actin. To bypass the autofluorescence background of Matrigel, the liposomes were doped with 2% DiD (1,1'-dioctadecyl-3,3,3',3'-tetramethylindodicarbocyanine), and then mixed in liquidized Matrigel at 4ºC. The gelation was allowed to proceed on the microscope stage overnight at room temperature.

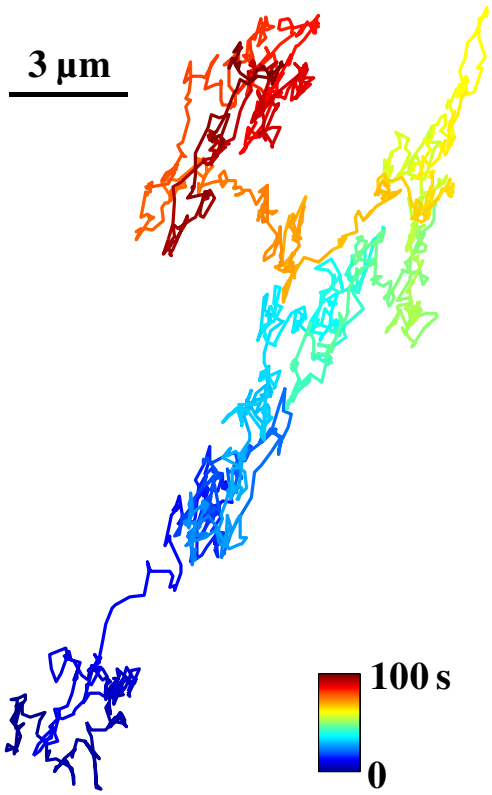

Figure A2

A typical anisotropic trajectory of 90 nm DOPC/DOPE-PEG liposome diffusing in nematic F-actin (c = 5 mg/mL) projected onto the x-y plane with 50 msec between frames, measured for 100 sec. Colors denote time lapse of the trajectory. The liposomes, dyed by N-(lissamine-rhodamine B)-dioleoylphosphatidylethanolamine (Rhb-DOPE), were added at concentration ~10^{-15} M into G-actin solutions reconstituted in fresh G-buffer (5 mM TRIS (tris(hydroxymethyl)aminomethane) at pH 8.0, supplemented with 0.2 mM $CaCl_2$, 1 mM ATP, and 0.2 mM dithiothreitol (DTT) and 0.01% NaN_3). The F-actin networks were formed by the addition of salt (100mM KCl, 2mM $MgCl_2$), and the polymerization was allowed to proceed on the microscope stage overnight.

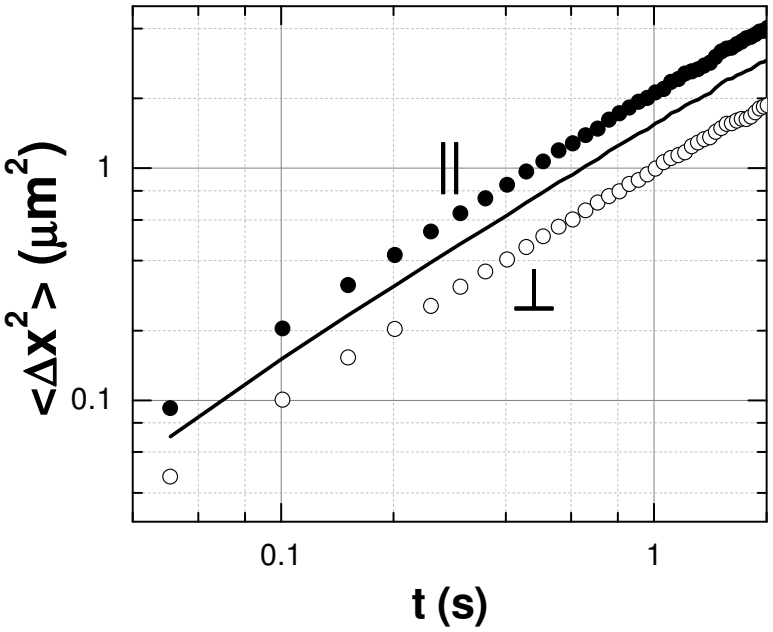

Figure A3

One-dimensional MSDs of 90 nm DOPC/DOPE-PEG liposome diffusing in nematic F-actin (c = 5 mg/mL) along (filled symbols) and perpendicular to (open symbols) the major axis, which is determined by 1st principal component of the displacement vectors. The solid line represents the average, i.e. $\frac{1}{2}\left\langle \Delta x_{\perp}^2 + \Delta x_{\parallel}^2 \right\rangle$.

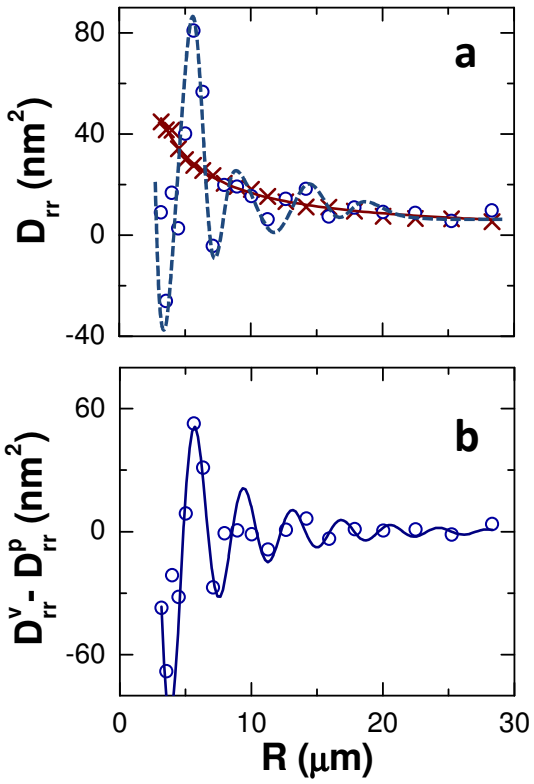

Figure A4

Two-point longitudinal displacement correlation is defined as $D_{rr}(R,\tau)=\left\langle \Delta r_i^{\parallel}(t,\tau)\Delta r_j^{\parallel}(t,\tau)\right\rangle_{i\neq j,t}$, where $\Delta r_{i,j}^{\parallel}$ is displacement over lag time τ of two distinct vesicles with separation R along the vector connecting their centers. (a) The D_{rr} are plotted as a function of separation R with lag time $\tau=0.25\,s$, for fluid vesicles (circles, 1,2-dierucoyl-*sn*-glycero-3-phosphocholine, DEPC, diameter 495 nm) and BSA coated polystyrene nanoparticles (crosses, diameter 500 nm), in entangled isotropic F-actin networks of concentration 2 mg/mL. D_{rr} of particles are fitted as $D_{rr}\propto r^{-1}$ (solid line). The dashed line is a guide to eye highlighting the oscillations. (B) The $D_{rr}^{v}-D_{rr}^{p}$, subtracting the correlation of rigid particles from that of vesicles, is plotted against separation R. The solid line is a fit to semi-empirical formula $D_{rr}^{v}-D_{rr}^{p}=A\cdot\cos\left(\frac{R}{\lambda}+\delta\right)\cdot\frac{1}{R}e^{-\frac{R}{\kappa}}$, which gives amplitude A growing linearly with lag time τ, and two length scales periodicity of the oscillation $2\pi/\lambda\approx 3.7\pm 0.3\,\mu m$ and the decay length $\kappa\approx 10\pm 4\,\mu m$.

Table

Table A1

Liposome sizes measured by dynamic light scattering[a,b].

Lipid type	Filter pore diameter (nm)[c]		
	100	200	400
DLinPC[d]	n.d.	180±10	220±45
DOPC[e]	130±15	200±30	320±85
DEPC[f]	140±15	270±60	495±150

[a] measured on a Brookhaven Instruments 90Plus particle size analyzer
[b] the sizes are reported as mean ± standard deviation in nanometers
[c] the diameters of the cylindrical pores of the track-etch membranes (Whatman) are reported by the manufacturer to have narrow distributions.
[d] 18:3 (Cis) PC, 1,2-dilinolenoyl-*sn*-glycero-3-phosphocholine
[e] 18:1 (Δ9-Cis) PC, 1,2-dioleoyl-*sn*-glycero-3-phosphocholine
[f] 22:1 (Δ9-Cis) PC, 1,2-dierucoyl-*sn*-glycero-3-phosphocholine